Advancing electrocatalysis in solid acid fuel cells

Thesis by

Áron Varga

In Partial Fulfillment of the Requirements

for the Degree of

Doctor of Philosophy

California Institute of Technology

Pasadena, California

2013

(Submitted June 5, 2013)

Dedicated to my loving parents and my sister Marta, who were always there for me.

"*The most exciting phrase*
to hear in science,
the one that heralds new discoveries,
is not 'eureka', but 'that's funny...'"

Isaac Asimov

Acknowledgments

This thesis would not have been possible without the help and support of the Caltech community. It has been a pleasure to come to work every day because of the people. Caltech provides the ideal environment for scientific discovery.

First and foremost, I would like to thank my advisor Prof. Sossina Haile, whose guidance and mentorship throughout my entire thesis was invaluable. It was an honor and pleasure to be part of her group.

I am extremely grateful to Profs. Konstantios Giapis and Richard Flagan for their continuous strong support and many insightful discussions. They were co-mentors to me. Many thanks to Prof. George Rossman and Nathan Dalleska for all the discussions and support with numerous projects and Prof. Yohannes Abate for continuing collaboration.

I would like to thank my thesis committee, Professors William Goddard, William Johnson, and Konstantinos Giapis for advice and support and the Caltech Materials Science Department for the opportunity to work and live at such a phenomenal place as Caltech.

I was also very fortunate to have patient senior students and scientists to work with right from the beginning: First and foremost Nicholas Brunelli, with whom collaborations still continue. Kenji Sasaki, Mary Louie, Dane Boysen and Calum Chisholm all helped me get up to speed quickly with solid acid fuel cells. It was

a great pleasure working with Andy Downard branching out to the field of aerosol science.

Caltech would not be half as fun without fantastic friends, BG, Steve, Christina, Pratyush, Cindy, Sawyer, Kuba, Rob and of course Hanqing. Thanks to Christina for introducing me to roadbiking and mountainbiking and to Pratyush for inspiring me to go to the mountains. And many more marathons with BG!

It was a fantastic experience to have worked with and mentored many SURF students through the years at Caltech: Stephanie Wuerth, Ryan George, Hyung Wan Do, Jeffrey Kowalski, Rachel Deghuee. Very fruitful collaborations and great teamwork with master students Marcel Schreier and Moritz Pfohl helped with a large part of carbon nanotube project. And thanks for the fun, collaborative work with Vanessa Evoen.

The Haile group is such a pleasant and intense group of people, always open and eager for discussion, and a helping hand: Special thanks to Yoshi, Rob, Chatr! And to my office mates: Evan, Taesik, Teruyuki, Carolyn.

It was such a pleasure working with highly skilled machinists for building new equipment: Michael Vondrus and Richard Gerhart.

And of course thanks to my family: I could not have done it without your love!

Abstract

Solid acid fuel cells are currently performance limited by the electrochemical reaction kinetics at the electrodes. For acceptable power output, precious metal catalysts such as platinum, are required, rendering the technology too expensive for commercialization in all but niche applications. This thesis explores new approaches to solid acid fuel cell electrodes with the aim of reducing the catalyst loading or even eliminating precious metals entirely, without sacrificing performance. Two broad approaches are pursued: nanostructuring for enhanced catalyst utilization and incorporation of carbon-based materials for enhanced electrical transport and even electrocatalysis.

Electrospray deposition is shown to be a viable technique to produce nanoparticles of the solid acid fuel cell electrolyte material CsH_2PO_4. *In situ* aerosol particle size measurements using a differential mobility analyzer and a condensation particle counter allowed the characterization of the electrospray parameter space, resulting in CsH_2PO_4 particle size control between 10 and 50 nm. Co-deposition of the CsH_2PO_4 nanoparticles together with a stabilizing surfactant polyvinylpyrrolidone (PVP) and platinum catalyst nanoparticles allows the creation of highly active, porous, interconnected electrode nanostructures. These nanostructures directly deposited onto fuel cell components, either the carbon paper current collector or the thin film electrolyte layer, serve as electrodes. A 30-fold reduction of platinum loading, without sacrificing electrode performance as compared to mixed powder-electrodes, is demonstrated.

The direct deposition of CsH_2PO_4 nanoparticles with the stabilizing surfactant PVP onto a prefabricated CsH_2PO_4 electrolyte layer and subsequent magnetron sput-

tering of a nanometer thin platinum film lead to surprising catalyst-mass normalized electrode activities for solid acid fuel cell anodes. Specifically, a 25-fold increase in the mass normalized activity is shown as compared to the predicted values from analysis of platinum thin films with a controlled geometry.

The second part of the thesis deals with the introduction of carbon nanotubes to the solid acid fuel cell electrodes. Three types of carbon nanotubes (CNTs) were grown directly onto the carbon paper current collector, in all cases using a chemical vapor deposition method and nickel catalyst nanoparticles.

(i) Conventional CNTs were shown to act as effective current collectors for electrosprayed composite electrode structures, containing platinum nanoparticles. Matching of scales between the current collector and the electrosprayed structure leads to improved interconnectivity of the platinum catalyst nanoparticles and a higher density of electrochemically active triple phase boundaries.

(ii) Nitrogen doped carbon nanotubes (NCNTs) were shown to actively catalyze oxygen electroreduction in solid acid fuel cells, with no platinum present.

(iii) Undoped but defective carbon nanotubes (dCNTs) were shown to be highly efficient catalysts of the oxygen electroreduction reaction, surpassing the activity of the state of the art, platinum containing electrodes. This is the first time undoped carbon nanotubes have been reported to be catalytically active for electroreduction of oxygen.

In addition, catalytically active carbon nanotubes show excellent catalysis of the water splitting reaction, creating the opportunity for new applications of these solid state electrochemical devices.

Contents

List of Figures

List of Tables

Chapter 1

Introduction

1.1 The energy problem

Human prosperity has always been directly correlated with energy consumption. With some fluctuation, both have risen slowly but steadily over millennia, from hunter-gatherers to agrarian societies. Incremental technological advances have resulted in a slow expansion of both the size of the population and per capita energy consumption. Non-sustainable levels of energy consumption have been reached during the industrial revolution, with extremely rapid increase after World War II, especially in the use of fossil fuels, Figure 1.1.

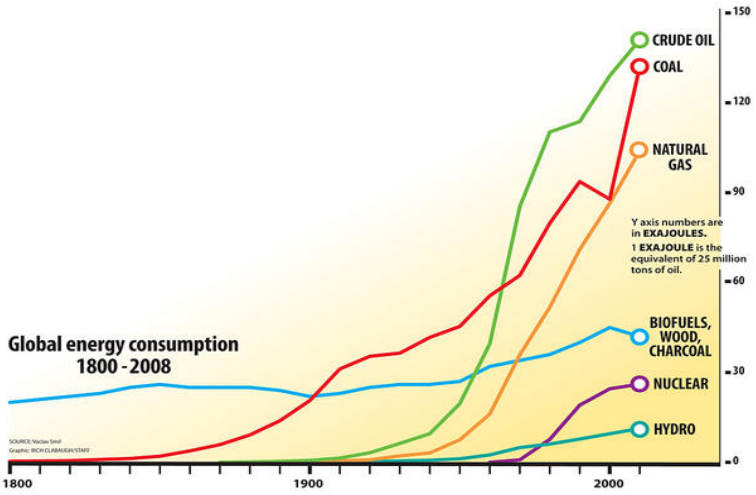

Figure 1.1: Global energy consumption vs. time (source: IEA)

Today, many populous countries, such as China, India, and Brazil are experiencing rapid economic development, entailing a staggering increase in per capita energy consumption. Multiplied by their large populations, this development provides the main driving force for increased energy demand.

Fossil fuels provide most of the primary energy today, often leading to geopolitical instability, global warming through the greenhouse effect caused by increased atmospheric CO_2 concentration, and local pollution from combustion particulates. Even though alternative energy sources, such as solar and wind power are becoming mainstream technologies, their significantly higher cost demands more efficient energy conversion. In addition, fluctuations in solar irradiation and wind conditions on the one hand and the need for reliable and constant energy supply on the other hand demand large scale energy storage. Nathan Lewis et al. have identified storing energy in the form of chemical bonds of molecules, such as hydrogen and oxygen the only viable method. [1]

Fuel cells are well situated to fulfill the role of energy conversion since they are the most efficient devices yet invented to convert chemical energy to electrical energy and can operate with a variety of chemical fuels including hydrogen. Direct combustion of fuels is often accompanied with significant amount of toxic gas emissions and low conversion efficiencies. Research on fuel cell technologies is therefore urgently needed to facilitate society's transition to a truly sustainable energy infrastructure.

1.2 Fuel cells

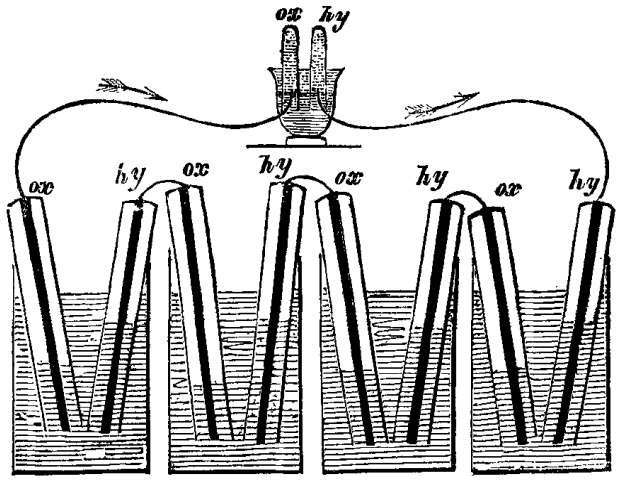

Figure 1.2: "Gaseous voltaic battery" consisting of platinum electrodes and sulfuric acid electrolyte, first demonstrated by Prof. William Grove in 1842 [2]

Fuel cells are defined as electrochemical energy conversion devices, directly converting chemical energy into electrical energy. The first description of a "gaseous voltaic battery" was given by Sir William Grove in 1842. [2] It consists of electrodes made of platinized platina in hydrogen and oxygen and dilute sulfuric acid electrolyte, Figure 1.2. In the past 160 years since Prof. William Grove's invention, a tremendous amount of work has been done to improve fuel cells, with five main technologies emerging, summarized in Table 1.1.

The electrolyte membrane is considered the property-determining component of a fuel cell, since it defines the operating temperature and the half-reactions at the electrodes. This in turn defines other materials and operational features, such as catalyst requirements, range of fuels that can be used, and start-up/shut-down times. Each technology has advantages and disadvantages as explained in the following sections. [3]

At high operating temperatures (Molten Carbonate (MCFC) and Solid Oxide Fuel Cells (SOFC)), efficient internal reforming of hydrocarbon fuels to CO and H_2 allow the use of hydrocarbons. Non-precious metal catalysts, such as nickel are sufficient to

Table 1.1: Fuel cell types

Type	PEMFC	AFC	PAFC	MCFC	SOFC
Temperature (°C)	70 - 110	100 - 250	150 - 220	500 - 700	700 - 1000
Electrolyte material	sulfonated polymers	(Na,K)$OH_{(aq)}$	H_3PO_4	$(Na,K)_2CO_3$	$(Zr,Y)O_{2-\delta}$
Mobile ion species	H_3O^+	OH^-	H^+	CO_3^{2-}	O^{2-}
Fuel	H_2, CH_3OH	H_2	H_2	hydrocarbons and CO	hydrocarbons and CO
Oxidant	O_2	O_2 and H_2O	O_2	O_2 and CO_2	O_2

effectively catalyze the electrochemical reactions at the electrodes. In addition, they are largely resistant to poisoning through sulfur and other contamination, and to carbon deposition. However, high operating temperatures also require expensive ceramic interconnect and support materials. Mismatch of thermal expansion coefficients of the different fuel cell components pose a significant challenge for sealing high temperature fuel cells. To avoid thermal shock, a long ramp-up and ramp-down time is required, making these fuel cell types not suitable for portable or mobile applications.

At the other end of the operating temperature spectrum (Polymer electrolyte fuel cells (PEMFC)), at low temperatures, only expensive precious metal catalysts such as platinum can effectively catalyze the electrochemical reactions at the electrodes. Catalyst poisoning from impurities in the fuel pose a significant challenge and require high purity feed gases. In addition, water molecules are involved in the proton transport in PEMFCs requiring smart water management to avoid dehydration at the anode and catalyst flooding at the cathode. Fast ramp-up and ramp-down times allow portable and mobile applications, such as battery replacements in laptops and cars.

The so-called temperature "sweetspot" for fuel cell operation, where inexpensive interconnect and support materials (e.g. stainless steel) can be used while not requiring precious metal catalysts or at least enabling a high resistance to catalyst poisoning is the intermediate temperature range between 200 and 400 °C. Both Alkaline (AFC) and Phosphoric Acid Fuel Cells (PAFC) fall into this category, but both operate with toxic and corrosive liquid electrolytes, posing significant engineering and safety challenges.

As a relative new technology in the field of fuel cells, Solid Acid Fuel Cells (SAFC) are well situated to alleviate most of the challenges other fuel cells types are facing. Its operating temperature of $\sim$ 240 °C, while employing a solid electrolyte permits simple cell design with inexpensive stainless steel interconnect and support materials. Catalyst poisoning is not observed even when hydrocarbons, such as methanol or ethanol are used as fuels [4,5]. Since water is not involved in the ion transport through the electrolyte, complicated water management beyond simple humidification of the feed gases is not required. [6]

1.3 Solid acid fuel cells

1.3.1 Fundamentals

Similar to other types of fuel cells, solid acid fuel cells (SAFCs) consist of three active components: anode, electrolyte, and cathode, Figure 1.3. In addition, passive components, such as current collectors, interconnects, and mechanical support materials, are needed to complete the cell. For a controlled release of the energy stored in the chemical bonds of the fuel (e.g. hydrogen) and the oxidant (e.g. oxygen), the ionically conducting electrolyte membrane needs to be gas impermeable and an electric insulator.

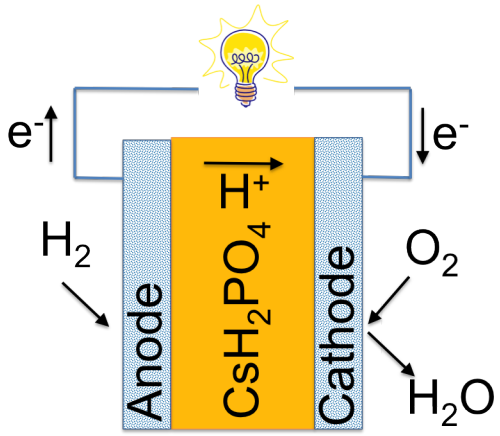

Figure 1.3: Schematic of a solid acid fuel cell

The two spatially separated half-reactions 1.1 and 1.2 at the anode and cathode respectively, are:

Anode:

$$H_{2(g)} \rightarrow 2\ H^+ + 2\ e^- \tag{1.1}$$

Cathode:

$$2\ H^+ + 2e^- + 1/2\ O_{2(g)} \rightarrow H_2O_{(g)} \tag{1.2}$$

Net reaction:

$$H_{2(g)} + 1/2\ O_{2(g)} \rightarrow H_2O_{(g)} \tag{1.3}$$

The thermodynamic driving force for the net fuel cell reaction (Equation 1.3) is given by the Gibbs free energy difference between the product (water) and reactants (hydrogen and oxygen):

$$\triangle G^{\circ}_{rxn} = -418\ \text{kJ/mol} \tag{1.4}$$

at standard conditions. The theoretical voltage across the fuel cell electrodes is

given by the Nernst equation 1.5:

$$E_{cell} = E^0 - \frac{RT}{nF} ln \frac{p(H_2O)^2}{p(O_2)p(H_2)^2} \tag{1.5}$$

where R is the universal gas constant, T is the absolute temperature, n is the number if moles of electrons involved in the reaction, F is Faraday's constant and E^0 is given by Equation 1.6

$$E^0_{cell} = \frac{-\triangle G^0_{rxn}}{nF} \tag{1.6}$$

The theoretical voltage is never reached in practice during fuel cell operation because of energy "losses" during several irreversible processes, indicated in the fuel cell polarization plot and often denoted as overpotentials, Figure 1.4.

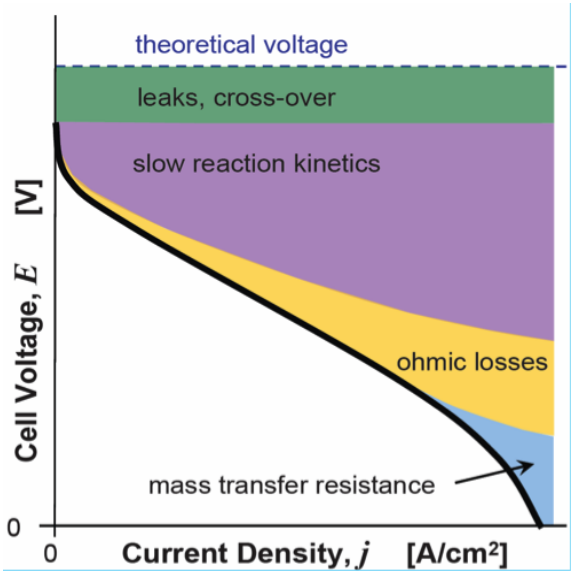

Figure 1.4: Typical fuel cell polarization plot showing various energy losses, known as overpotentials

Leaks of the fuel and oxidant feed gases across micropores in the electrolyte membrane and/or through sealing-imperfections as well as electronic cross-over lead to cell voltage reduction even when zero current is flowing.

The largest overpotential in low and intermediate temperature fuel cells is associated with the electrochemical reactions at the electrodes and is denoted activation overpotential. Especially the cathodic activation overpotential dominates as oxygen reduction reaction involves more elementary reaction steps, each associated with higher activation barriers than hydrogen oxidation.

Ohmic losses mainly due to ion transport through the electrolyte becomes more significant as the current density increases and cause resistance overpotential.

At very high current densities, the volume near the electrocatalytically active sites at the electrodes becomes depleted of the feed gases and a concentration overpotential arises that can be associated with mass transfer resistance.

Hence the cell voltage at any current density is described by Equation 1.7

$$E_{cell}(j) = E_{cell\ at\ j=0} - \eta_{crossover} - \eta_{activation} - \eta_{ohmic} - \eta_{diffusion} \tag{1.7}$$

1.3.2 Solid acid fuel cell performance

Solid acid fuel cells were first demonstrated in 2001 using $CsHSO_4$ at 150 - 160°C as the electrolyte [7] and in 2004 using CsH_2PO_4 at 250°C as the electrolyte [4]. For this intermediate operating temperature remarkable power density values of ∼416 mW cm^{-2} were reported in 2005 using 25 μm and 36 μm thin electrolyte membranes and pure hydrogen and oxygen as feed gases, Figure 1.5. [4] In 2006, alcohol fueled solid acid fuel cells were demonstrated using methanol, ethanol and even vodka. [5] More recently in 2009, 600 mW cm^{-2} power density values were achieved, again using hydrogen as the fuel and air as the oxidant with an optimized electrode catalyst material [8], Figure 1.6.

Significant efforts are underway to further improve the solid acid electrolyte in terms of conductivity and stability. Specifically the phase behavior of doped CsH_2PO_4 and the dehydration characteristics have been explored. [9–13]

Common to all the solid acid fuel cells is the fact that the I-R Ohmic losses at the

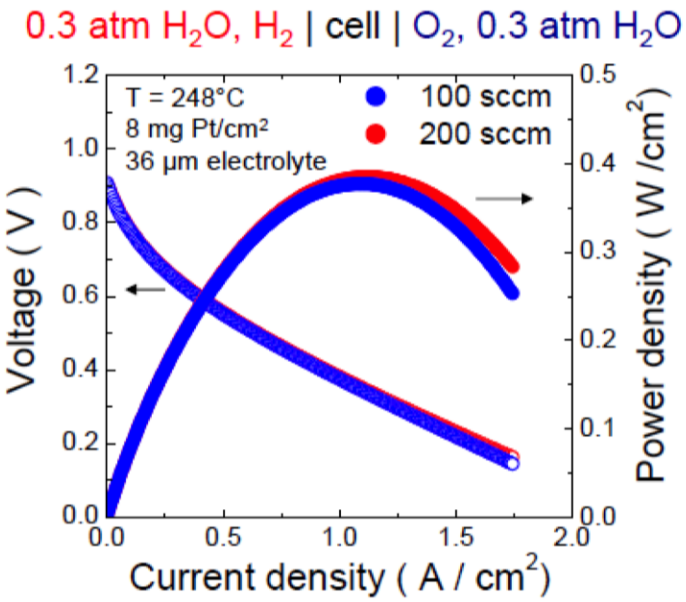

Figure 1.5: Polarization plot for a solid acid fuel cell with power density indicated [4]

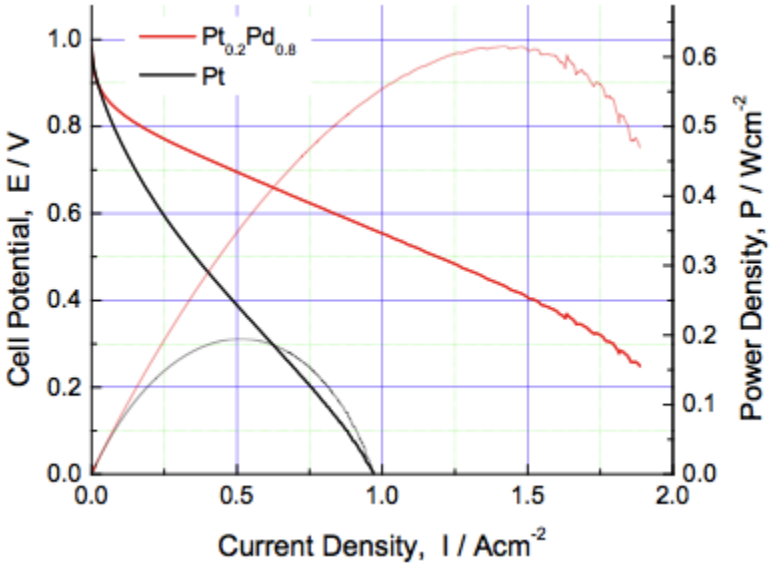

Figure 1.6: Solid acid fuel cell polarization plot with platinum and platinum-palladium alloy electrocatalyst at the cathode [8]

electrolyte membrane are significantly smaller than the activation losses of the electrochemical reactions, Figure 1.7. [6] This motivated intense efforts both in developing methods to understand the fundamentals of electrode reactions and in characterizing them. [14–17]

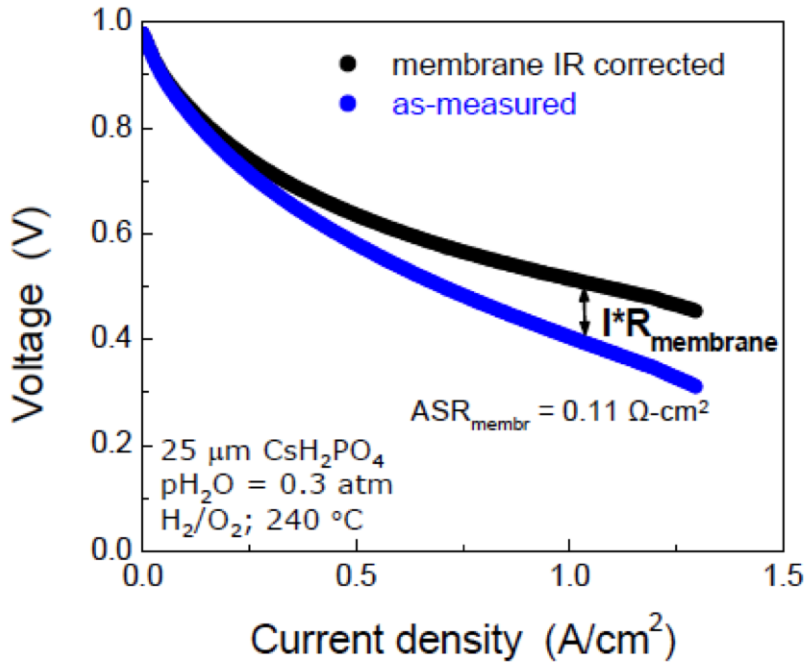

Figure 1.7: IR corrected solid acid fuel cell polarization plot showing small membrane area specific resistance compared to other sources of cell resistance [6]

1.3.3 Current status of SAFC electrodes

The electrode performance is characterized by the electrode resistance at a given current density, which in turn directly translates into a voltage, often denoted as the activation overpotential. High performance electrodes will have a low resistance to the flow of an electrochemical current, i.e. a low overpotential at a given current density. In other words, activation overpotential is the potential difference from the equilibrium Nernst potential necessary to drive a current. The relationship between the activation overpotential and the current density through the cell is given by the Butler-Volmer equation, Equation 1.8:

$$j = j_0(e^{\frac{nF\alpha_a\eta}{RT}} - e^{\frac{-nF(1-\alpha_c)\eta}{RT}}) \tag{1.8}$$

where j_0 is the exchange current density when η=0, α is the exchange coefficient describing the intrinsic activity of the electrode at conditions away from equilibrium, T is the temperature, R is the universal gas constant, and n is the number of electrons participating in the reaction.

At high overpotentials, where either the cathodic or the anodic current dominates, the Butler-Volmer (Equation 1.8) equation can be simplified into the Tafel equation (Equation 1.9), giving a simple relationship between the net electrochemical current and the activation overpotential necessary to attain it:

$$\eta_{activation} = \frac{RT}{\alpha_{aorc}nF} ln(\frac{j}{j_0}) \tag{1.9}$$

For a given material system with intrinsic parameters, such as the exchange coefficient, the operating temperature and type of reaction, the only possibility of reducing the activation overpotential is by reducing the microscopic current density through an electrochemically active site. To maintain the total current through the electrode, the number of electrochemically active sites needs to be increased accordingly. Macroscopically, the current density does not change because it is calculated as the ratio of the total current to the projected area of the electrode, which typically extends into the third dimension, Figure 1.8.

In order to maximize the number density of electrochemically active sites, a porous three-dimensional composite structure is typically utilized, consisting of three phases: electrolyte particles, catalyst particles (sometimes together with a current collector) and open pores for free gas flow. With large (>100 nm) catalyst particles, the electrochemically active site is the so-called three-phase boundary at the conjunction between the electrolyte, the catalyst and the gas phase. Here, the simultaneous transport of ionic species, electrons and gas molecules can occur. Catalyst or electrolyte particles that are isolated, do not participate in the electrochemical reaction.

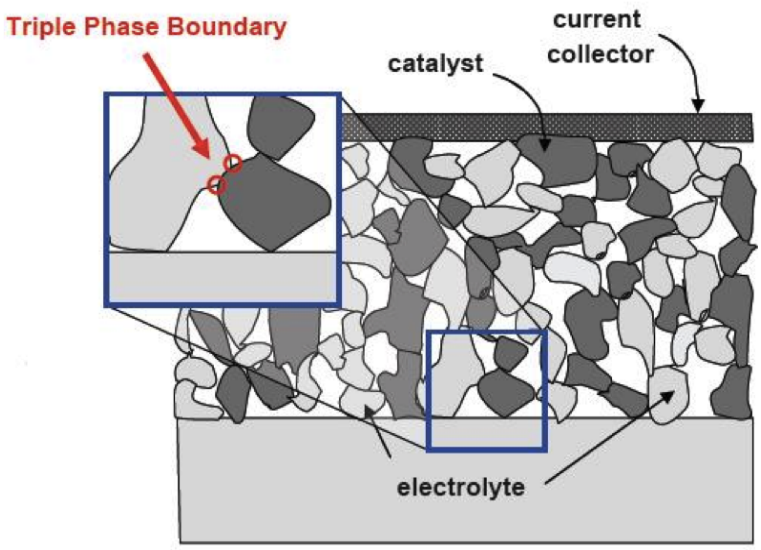

Figure 1.8: Schematic of a composite fuel cell electrode

Recent studies of hydrogen electroreduction at the anode of solid acid fuel cells, using thin platinum films with well controlled geometries have revealed that not only the three-phase boundary mechanism is active. [14] The diffusion rate of hydrogen through platinum thin films smaller than 50 nm is sufficiently fast that the entire two-phase boundary between the platinum thin film and the CsH_2PO_4 electrolyte is contributing to the overall electrochemical current, Figure 1.9. The elementary steps of the simple hydrogen electrooxidation reaction have not been described for solid acid fuel cells.

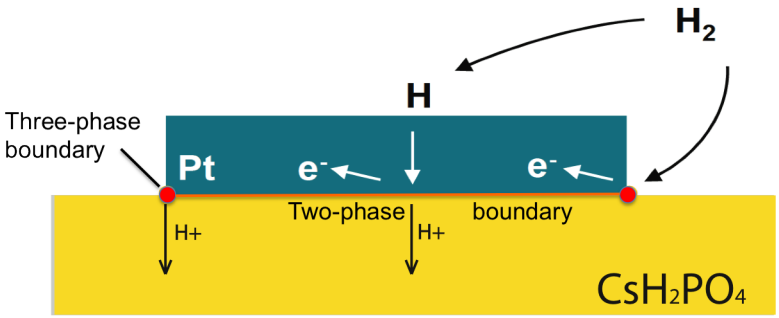

Figure 1.9: Schematic of three-phase boundary and two-phase boundary pathway for hydrogen electrooxidation at the anode

The oxygen electroreduction reaction elementary steps remain even more elusive, since it is a multistep, four electron reaction. It has been studied extensively for polymer electrolyte and solid oxide fuel cells, however the difference in operating temperatures and environments make a direct transfer of the findings to solid acid fuel cells impossible. Nevertheless, we can speculate either a three-phase boundary mechanism and/or a two-phase boundary mechanism as shown in Figure 1.10.

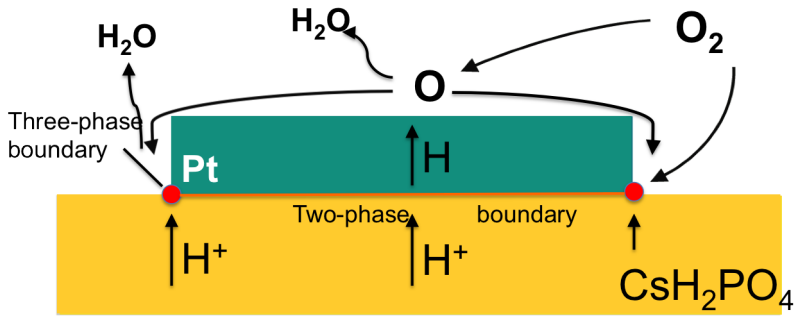

Figure 1.10: Schematic of three-phase boundary and two-phase boundary pathway for oxygen electroreduction at the cathode

Optimal electrodes therefore will either maximize the density of three-phase boundaries or maximize the two-phase boundary area, depending on which electrochemical reaction mechanism is dominant as shown in Figure 1.11.

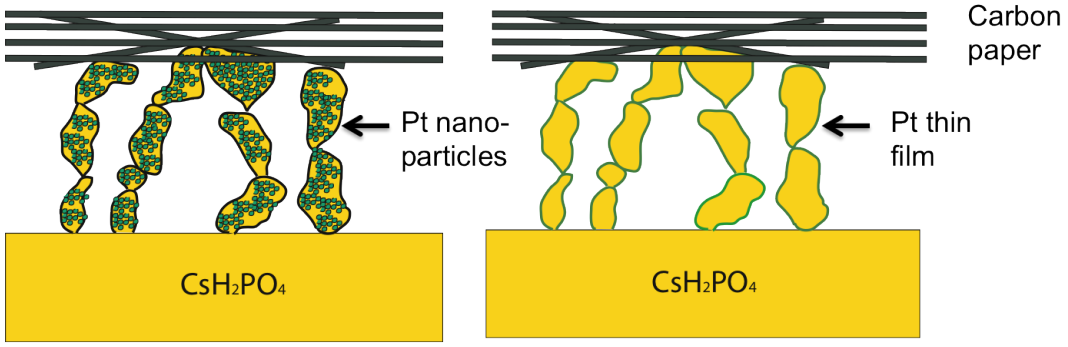

Figure 1.11: Schematic of ideal solid acid fuel cell electrodes (a) maximizing triple phase boundary area and (b) maximizing two phase boundary area

Solid acid fuel cell electrodes consist of mechanically mixed powders of CsH_2PO_4 and catalyst(s). The CsH_2PO_4 powder is typically fabricated using the co-precipitation method where Cs_2CO_3 and H_3PO_4 are allowed to react in an aqueous solution.

CsH_2PO_4 is precipitated out in an ultrasonicated methanol bath to give $\sim 5\mu$m diameter particles. This powder is mixed with commercially available platinum powder (ca. 10 nm diameter) and platinum on carbon black powder ($\sim$ 40 nm in diameter) at an empirically optimized weight ratio of Pt:Pt/C:CsH_2PO_4 (3:1:3 wt ratio), Figure 1.12. It is immediately apparent that a large number of platinum particles are not in contact with the electrolyte particle, rendering them inactive towards the electrochemical reactions. Their sole purpose is current collection away from those platinum particles that are in direct contact with the electrolyte material.

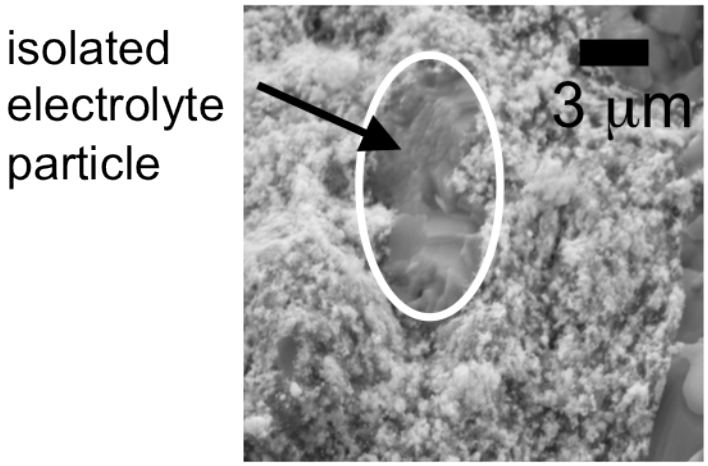

Figure 1.12: SEM micrograph of mechanically milled composite SAFC electrode consisting of micrometer sized CsH_2PO_4 powder and nanometer sized Pt-catalyst powder

Significant improvements in catalyst utilization can be achieved by two methods: 1. Creating a more well-mixed powder by matching the scales of the electrolyte and catalyst particles. To this end, conventional aerosol methods have been used to fabricate small CsH_2PO_4, with particle sizes ranging from 1.1 μm to 160 nm. Already significant improvements have been achieved with the activation overpotential reduced from 0.25 V to 0.16 V, Figure 1.13. Simple extrapolation of the CsH_2PO_4 particle diameter to smaller values is expected to give even smaller electrode overpotentials, Figure 1.14.

2. The highest mass normalized activity for platinum containing solid acid fuel cell anodes is 19 S cm^{-1}. The anode consisted of a sputtered 7.5 nm thin platinum

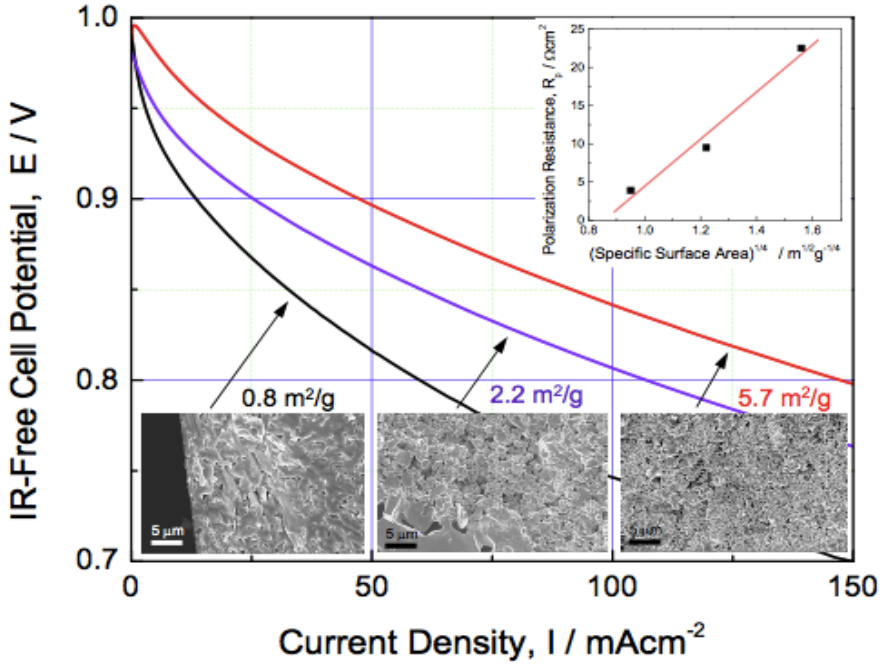

Figure 1.13: "Comparison of IR-free polarization curves of SAFCs incorporating different sized CsH_2PO_4 particles in the cathode. Scanning electron micrographs of the electrodes are shown and the inset presents the correlation between effective charge transfer resistance and average particle size, L (of the electrolyte component of the cathode). IR correction was performed by subtracting out the Ohmic resistance of the electrolyte." [8]

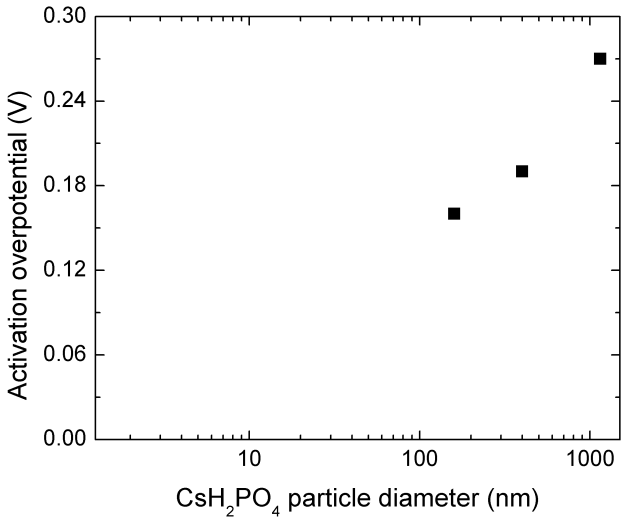

Figure 1.14: Activation overpotential vs. CsH_2PO_4 particle diameter in a composite powder electrode as calculated with data from Figure 1.13 [8]

Table 1.2: Solid acid fuel cell electrodes

Electrode	Resistivity ($\Omega\ cm^2$)	Pt loading ($mg\ cm^2$)	mass normalized activity ($S\ mg^{-1}$)
7.5 nm sputtered Pt film	3.1 ± 0.5	0.017	19
Pt:CsH_2PO_4 (1:2 wt ratio)	1.7	10	0.059
Pt:Pt/C:CsH_2PO_4 (3:1:3 wt ratio)	0.06	7.7	2.2

film on polished CsH_2PO_4 pellet (19 mm diameter). The absolute performance of the anode can be enhanced by increasing the surface area of the underlying CsH_2PO_4 by depositing them in a nanoparticulate form, Figure 1.11.

At present, solid acid fuel cell cathodes are fabricated in the same manner as the anodes, as described above. The activation overpotential for the oxygen reduction reaction at the cathode is dominating, see Figure 1.15: Therefore, an improved electrode will have the largest impact at the cathode side.

1.4 Objectives of this dissertation

1.4.1 Enhanced platinum utilization at electrodes

Commercial application of low and intermediate temperature fuel cells have been hindered by the need for high loading of expensive precious metal catalysts at the electrodes. High performance powder electrodes of solid acid fuel cells employ 7.7 mg cm^{-2} platinum. This dissertation aims to reduce the platinum loading while maintaining the electrode performance through new fabrication methods.

1.4.2 Precious metal free electrode catalysts

Replacing precious metals as the electrocatalyst in fuel cells is a daunting task and has been the subject of intense research. The second part of the dissertation explores

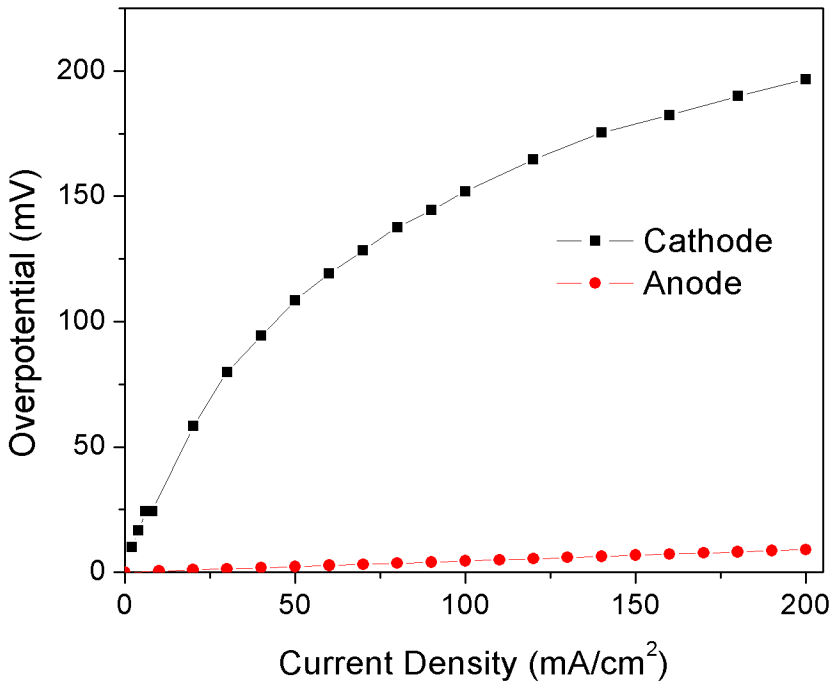

Figure 1.15: Activation overpotential of cathodic and anodic reaction [18]

the possibility of reaching the goal of completely precious metal free solid acid fuel cell with commercially viable performance.

Chapter 2

Methods

2.1 Electrospray deposition

2.1.1 Introduction

The concept of electrospray was first demonstrated in 1914 by John Zeleny. [19] Over the past century, electrospray technology has found various applications including electrostatic painting, crop spraying, and fuel dispersion. Seminal papers describing the physical processes governing electrospraying include the work of Sir Geoffrey Taylor [20], Lord Rayleigh [21], Malcolm Dole [22], and Julio V. Iribarne [23]. Widespread application of the electrospray as a tool for scientific research started in the 1990s with John B. Fenn using an electrospray to ionize large molecules, permitting for the first time their analysis with a mass spectrometer. [24] Mass spectrometry of large molecules in turn enabled rapid developments in medical and biological sciences, earning John Fenn the Nobel Prize in 2002.

In the field of fuel cells, electrospray deposition has also been used to create thin films of oxide materials with varying porosity [25–28] as well as nanoparticles [29,30]. Functional but not "high performance" PEMFC electrodes have also been deposited via electrospray with the aim of simplifying the fabrication process. [31,32]

2.1.2 Electrospray apparatus

2.1.2.1 Operating principle

Electrospray deposition is a technique to generate a highly charged aerosol. In general, a liquid is pumped through a capillary that is held at a high voltage relative to a grounded substrate. As the liquid emerges at the tip of the capillary, the surface tension and electrostatic forces induce the formation of a highly charged aerosol, with typical droplet diameter of the order of a micron. The droplets are accelerated along the electric field lines towards the substrate, while the liquid is evaporating. With the droplet radius decreasing but the overall charge remaining constant, the charge density can increase until the surface tension is not sufficient to hold the droplet together, thus causing the droplet to disintegrate into secondary droplets. This process may occur multiple times until all the liquid is evaporated. If a solvent is present in the liquid, nanoparticles may be formed and deposited onto the grounded substrate.

In my thesis work, three generations of electrospray systems were fabricated.

In general, the electrospray apparatus consists of a machined aluminum chamber (5 cm ID, 5 or 7 cm L and 1 cm wall thickness) with electrically insulating polymer (Delrin (175°C melting point), or Teflon (327°C melting point)) endcaps. A stainless steel capillary (ID 127μm, OD 1.6 mm, L 50 mm) through the center of the bottom endcap, sealed with a rubber O-ring served as the aerosol ejection nozzle. Three $\sim$3 mm deep, concentric groves around the capillary spaced 5 mm apart, machined into the polymer endcap served to trap any excess precursor liquid from the capillary and to increase the surface area to avoid electric breakdown between the capillary and the grounded chamber walls. In addition, two windows (1 cm diameter) were machined and adhered with epoxy into the electrospray chamber on opposite sides in order facilitate visual observation of the tip of the capillary during electrospraying. Two additional holes at the bottom of the chamber served as the sheath gas inlets, Figure 2.1. The substrate holder, which was protruding through the center of the endcap had a gas outlet channel machined through. A pressure gauge and a valve

were attached to the sheath gas outlet in order to monitor the pressure inside the electrospray chamber. The tip of the metal capillary was machined to have an angle smaller than 49.3° (Taylor cone angle [20]). Heatrope with three independent PID feedback controllers was used to control the sheath gas temperature, the electrospray chamber temperature, and the substrate holder temperature independently. A digital mass flow controller or a mechanical flow meter served to control the nitrogen sheath gas flow rate through the electrospray chamber.

In most cases, an inverted spray geometry was used, with the capillary pointing upwards against gravity. Here, the aerosol was accelerated toward the substrate at the top of the electrospray chamber, 1 - 5 cm away from the capillary. The more conventional geometry of spraying down onto a substrate was also explored for thin film fabrication.

The precursor liquid flow was controlled by a mechanical syringe pump or an air-pressurized Erlenmeyer flask. The pressure in the Erlenmeyer flask was regulated with a needle valve and monitored with a pressure gauge. The latter liquid delivery system is free of mechanical ratcheting effects, which may cause instabilities during the electrospray process. In addition, the Erlenmeyer flask can be ultrasonicated during electrospraying, in order to prevent agglomeration of nanoparticles, when colloidal suspensions are electrosprayed. To electrically bias the electrospray capillary, a high voltage, regulated DC power supply (Acopian Goldbox Infinity) was connected directly to the capillary. A picoammeter (Keithley 480 Digital 3.5 Digit Bench Picoammeter) was used to monitor the current carried by the charged aerosol droplets and/or particles, by connecting it in series between electric ground and the substrate holder. Any aerosol droplets and/or particles not deposited onto the substrate, exiting with the sheath gas were trapped in a HEPA filter or a water trap.

To explore higher deposition rates and hence shorten electrode fabrication times, an electrospray system with three active capillaries, arranged in with an equilateral triangle footprint was constructed. For improved uniformity of the deposited structure, twelve dummy capillaries also arranged with an equilateral triangle footprint

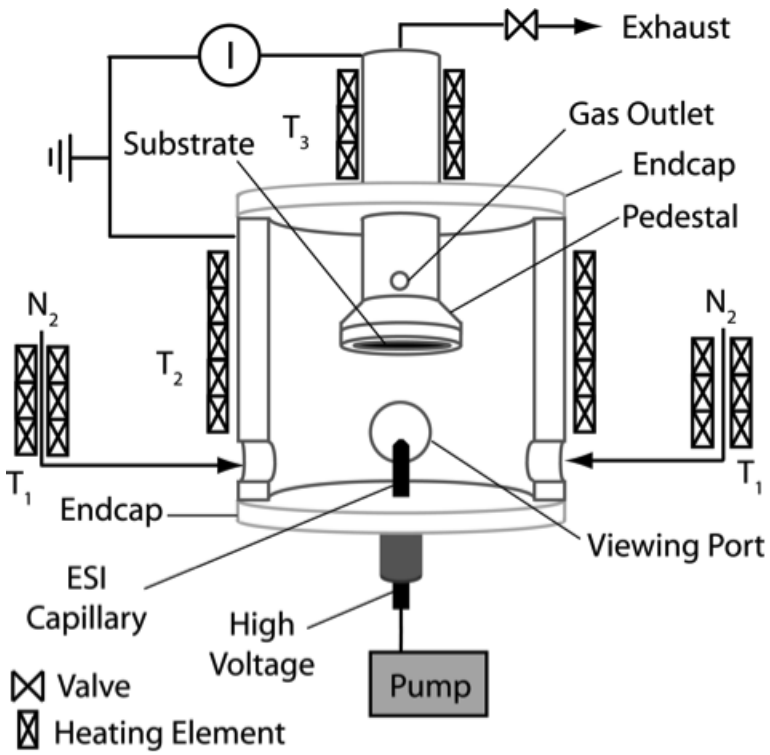

Figure 2.1: Schematic of electrospray apparatus [33]

around the active capillaries was added. The effects of longer flight paths on the deposited particle size were explored by adding a 30 cm long drying tube and electrophoretic deposition system to the electrospray, Figure 2.2.

In some instances, a microcapillary (OD 0.36 mm, ID 0.1 mm) was used for the nanoparticle deposition.

2.1.3 Electrospray mechanisms

The literature on the physical processes occurring during electrospraying is extensive, and includes discussions about the spraying modes, the formation of aerosol droplets, the transport and drying of the droplets, and deposition onto a substrate. Yet a comprehensive model has not been achieved.

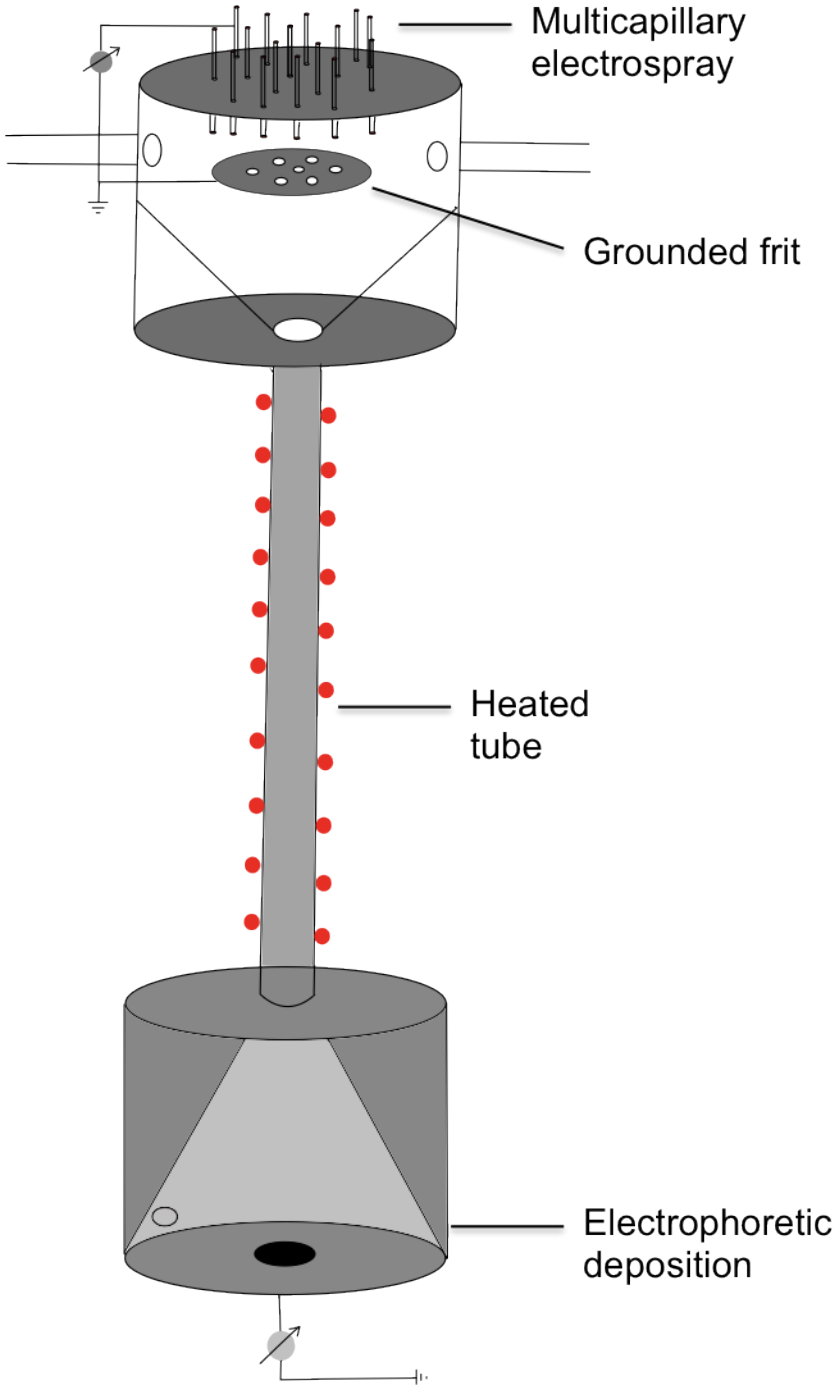

Figure 2.2: Schematic of electrospray apparatus with multiple capillaries and drying tube

2.1.3.1 Droplet formation

When a conductive liquid is pumped through the electrospray capillary, biased to a high voltage, a droplet emerges at the tip. It experiences both repulsive electrostatic forces and stabilizing forces due to the surface tension. In addition, inertial and viscous forces determine the behavior of the droplet and its shape, from which the highly charged aerosol emerges. Multiple spraying modes have been identified, that are generally dependent on the physical parameters controlling the aforementioned forces. These parameters include the electric and mechanical properties of the liquid (dielectric constant, conductivity, viscosity, density, surface tension) and electrospray parameters (flow rate, capillary voltage). A comprehensive description of spraying modes in the electrospray is given by Jaworek and Krupta [34], see Figure 2.3.

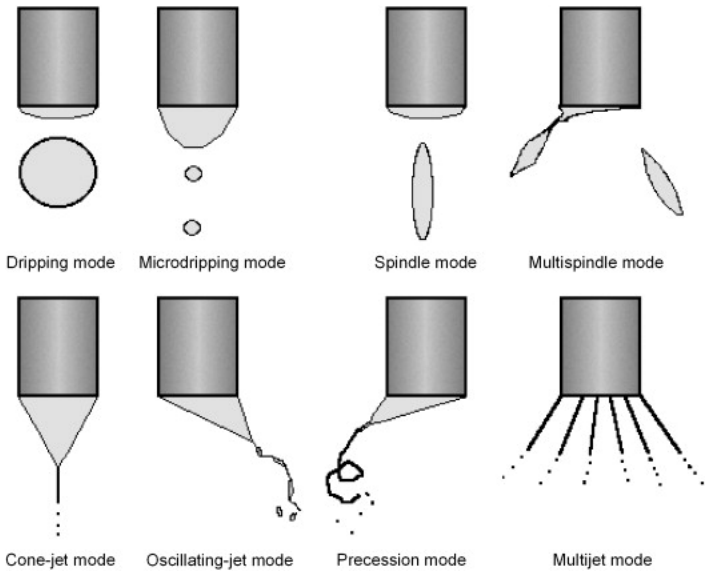

Figure 2.3: Various modes of electrospraying [35]

The most stable spraying mode, giving a fine aerosol spray, is the Taylor cone-jet mode, which was first described analytically by Taylor [20] and further studied among others by Lim et al. [36], Hartman et al. [37], Ganan-Calvo [38], and Hayati et al. [39].

The break-up of the Taylor cone-jet into aerosol droplets can occur in various modes as well, depending again on the physical characteristics of the precursor solu-

tion [40]. Quantitative analysis of the initially formed droplets has produced various scaling laws for the droplet size and charge per droplet [41–44] with the most recent comprehensive summary provided by Ganan-Calvo [45].

2.1.3.2 Droplet evaporation and disintegration

In typical electrospray operation, highly charged droplets on the order of microns are produced and are accelerated toward the grounded counterelectrode, which can be a substrate for deposition. During flight, the droplets evaporate while the total charge remains constant. With the increasing charge concentration, the repulsive electrostatic force can overcome the stabilizing surface tension forces , which is termed the Rayleigh limit. At the Rayleigh limit, instabilities form on the droplet, similar to a Taylor cone, emitting highly charged secondary droplets, Figure 2.4. This process can occur multiple times until the droplet is fully evaporated. The droplet evaporation and fission process has been described in detail by many authors [46–55].

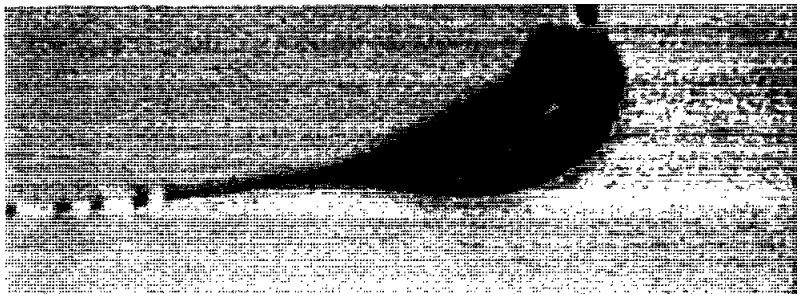

Figure 2.4: Stereozoom optical microscope image of a droplet of heptane during Coulomb fission, producing progeny droplets. [47]

2.1.3.3 Particle deposition and characterization

When a solution is sprayed and the solubility limit of the solute is reached, nucleation and growth of a solid particle is possible. When the solvent is completely evaporated, and pure solid particles deposit on a given substrate, dry thin films with varying porosity and even highly porous nanostructures may be result. [25, 27, 28, 56] The morphology of the deposited structure mainly depends on the electrical properties of

the substrate, the electrical properties of the deposited material and the particle size distribution. For instance, protrusions on a conducting substrate tend to concentrate the electric field lines, leading to preferential deposition of particles. Non-conducting or semi-conducting substrates can experience significant charge buildup, leading to a deflection of aerosol particles away from the similarly charged areas. The particle size distribution determines the final feature size and the porosity of the deposited structure. Therefore, the characterization of the aerosol (droplets and/or particles or mixtures of both) is important and has been conducted with optical microscopy [47], so-called doppler experiments [49, 50, 52], and differential mobility particle sizers [48, 57–62].

2.2 AC impedance analysis

AC impedance spectroscopy is a powerful tool to characterize the behavior of electrochemical cells. It was first established by Walter H. Nernst in 1894 to measure the dielectric constants of electrolytes. Since then, AC impedance spectroscopy has been used in a variety of fields, including the study of double layers, corrosion, electrocrystallization, mixed conductors, redox materials, and heterogeneous surfaces.

Typically, electrochemical processes have differing response times to a perturbation. AC impedance spectroscopy exploits this phenomenon by varying the frequency of a sinusoidal voltage perturbation over a wide range and measuring the current response, Figure 2.5.

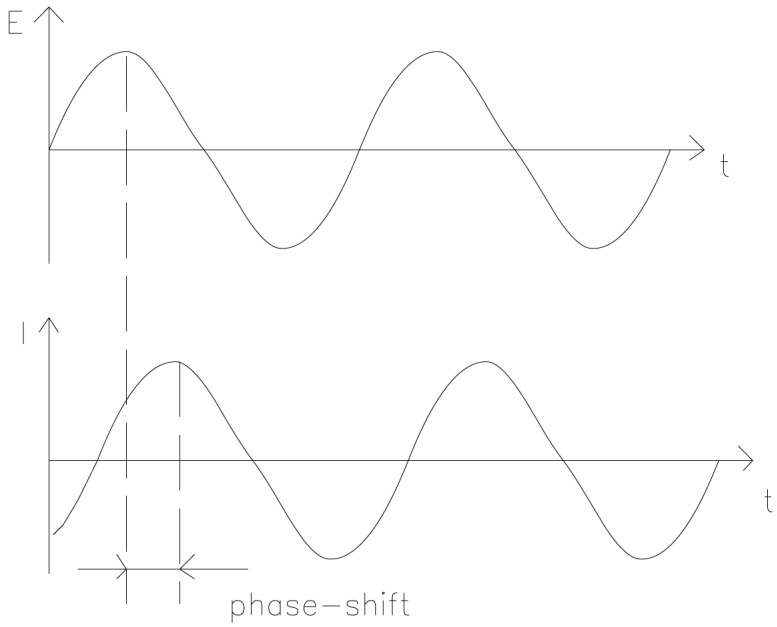

Figure 2.5: Sinusoidal voltage perturbation and current response in a linear system [63]

The complex impedance corresponding to the applied voltage and measured current can be obtained using Ohm's law, Equations 2.1, 2.2, and 2.3.

$$E(t) = E_0 sin(\omega t) \tag{2.1}$$

$$I(t) = I_0 sin(\omega t + \phi) \tag{2.2}$$

Using Euler's relationship:

$$Z(t) = \frac{E(t)}{I(t)} = \frac{E_0\ sin(\omega t)}{I_0\ sin(\omega t + \phi)} = Z_0\ (cos(\phi) + i\ sin(\phi)) \tag{2.3}$$

During fuel cell operation, multiple physical and chemical process occur simultaneously in series, where each process is associated with a complex resistance. These processes include migration of ionic species through the bulk electrolyte, the electrolyte grain boundaries, electrode-electrolyte interface, charge transfer reactions, diffusion of gaseous species at the electrode, etc. These processes are typically of capacitive and resistive nature, and hence, a so-called equivalent circuit consisting of capacitors and resistors is often used to model an electrochemical cell. If the characteristic frequencies of each process are sufficiently different, a deconvolution of the total impedance into contributions from these processes is possible using AC impedance spectroscopy.

A convenient way to visualize the complex impedance of an electrochemical cell is in the form of a Nyquist plot (-Im(Z) vs. Re(Z)). Capacitive and inductive processes are frequency dependent and can be represented as imaginary components, while purely Ohmic resistors are frequency independent and can be represented as real components of the complex resistance. The parametric plot as a function of frequency, of the complex impedance for a parallel RC circuit is shown in Figure 2.6.

2.3 Symmetric cell measurements

Measuring the polarization curve of a fuel cell gives information about the overall performance but no information about the characteristics of individual components, Figure 2.9. AC impedance spectroscopy on the other hand allows the characterization of each fuel cell component separately. The most convenient method is to use a symmetric cell geometry, single chamber configuration with only the oxidant or the fuel gas present and thus allowing the characterization of the cathode or the anode

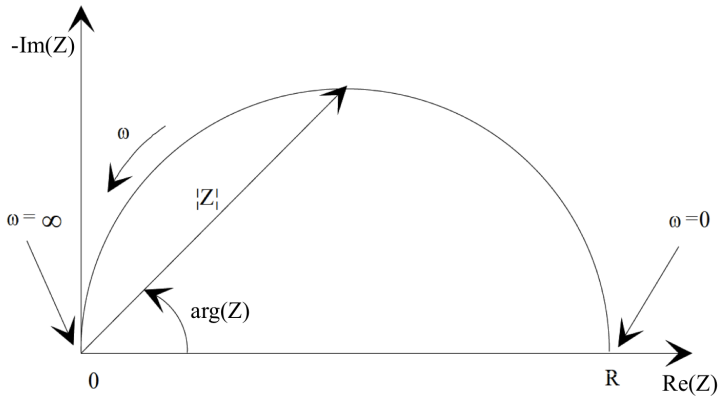

Figure 2.6: Nyquist plot of the impedance of a parallel RC circuit [63]

respectively.

When a small alternating voltage perturbation about equilibrium is applied to such as cell, no net current flows. In this configuration, both the forward and reverse half-reactions are probed at both electrodes. For small perturbations, the reaction kinetics is assumed to be equal in both directions, Figure 2.7, and 2.8.

Platinum containing solid acid fuel cell electrodes are not stable during a symmetric cell measurement in humidified oxygen at ∼240°C, oxidizing to PtO_x. A voltage equal to the redox potential for Pt + O → PtO at pO_2 = 0.53 atm and 240°C of 0.13 V, determined with Equation 2.4 and 2.5 needs to be applied to ensure platinum is in its reduced form.

$$E = \frac{-\triangle G}{nF} \tag{2.4}$$

$$\triangle G = \triangle G^{\circ} - RTln(pO_2) \tag{2.5}$$

Because we cannot measure platinum containing symmetric cells in an oxygen environment and hope that the microstructural insights can be transferred to the cathode, we use symmetric cell measurements in humidified hydrogen to characterize

novel electrodes in chapter 4 and 5.

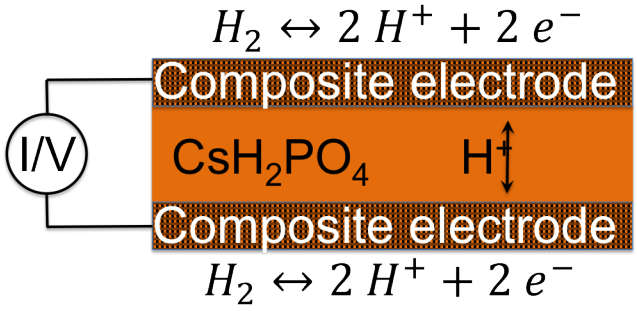

Figure 2.7: Schematic of a symmetric cell measurement in humidified hydrogen

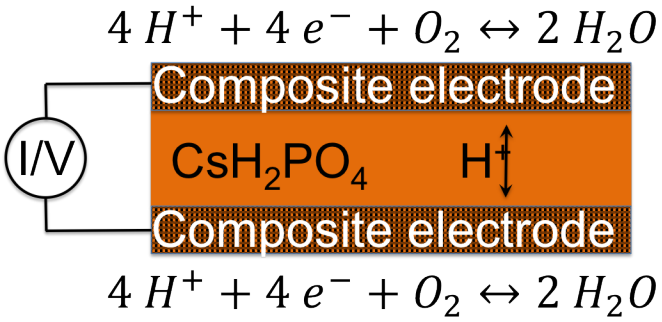

Figure 2.8: Schematic of a symmetric cell measurement in humidified oxygen

2.4 AC impedance spectroscopy with a DC bias

To characterize fuel cell electrodes with conditions closer to real fuel cell operating conditions than with the method described above, a DC voltage bias is applied to the cell during AC impedance spectroscopy. Figures 2.9, 2.10 and 2.11 show the correlation between the slope of the current-voltage curves and the complex resistance, as measured with AC impedance spectroscopy. In a symmetric cell configuration, the cell resistance at open circuit is measured (the steepest slope R_0). When a bias voltage is applied, a net current is forced through the cell and the electrode resistance decreases as expected for electrode processes controlled by Butler-Volmer kinetics.

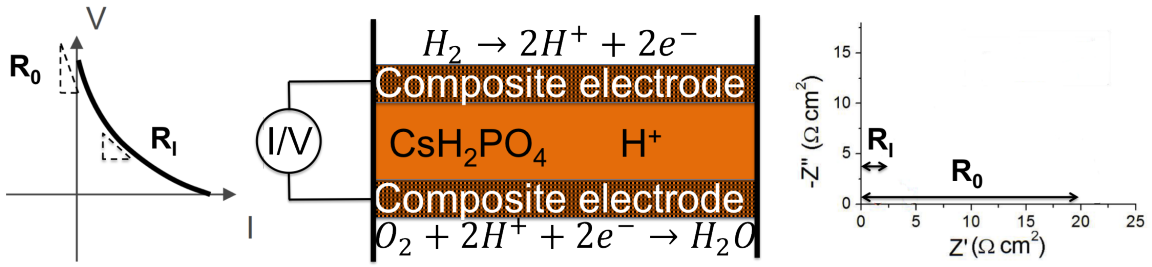

Figure 2.9: (a) IV curve of fuel cell with resistances indicated at zero current (R_0) and an arbitrary current (R_I), (b) Schematic of fuel cell with half reactions indicated (no proton migration at zero current), (c) Impedance information obtained from the polarization plot in (a)

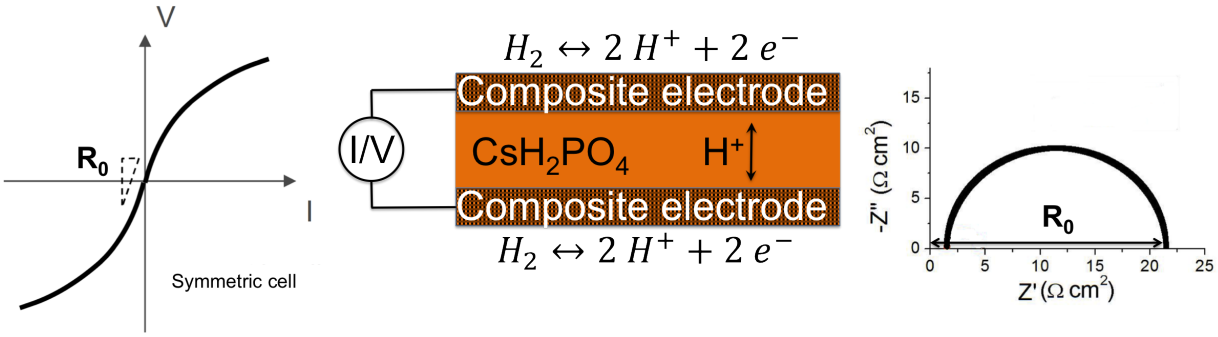

Figure 2.10: (a) IV curve of symmetric cell with no bias and resistance (R_0) indicated (zero net current), (b) Schematic of symmetric cell half reactions indicated (humidified hydrogen here), (c) Typical Nyquist plot of symmetric cell impedance obtained by AC impedance spectroscopy

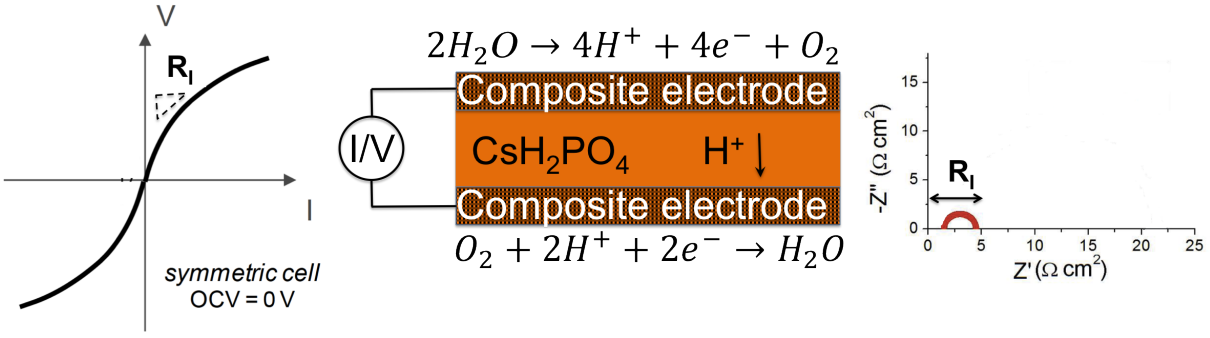

Figure 2.11: (a) IV curve of symmetric cell with bias and resistance (R_I) indicated (net current), (b) Schematic of symmetric cell half reactions indicated (humidified oxygen here), (c) Typical Nyquist plot of symmetric cell impedance obtained by AC impedance spectroscopy

Chapter 3

Electrospray synthesis of sub-100 nm CsH_2PO_4 particles

A. Varga, A. Downard, H.W. Do, V. Evoen, K. P. Giapis, R. C. Flagan, S. M.Haile, Electrospray synthesis of sub-100 nm CsH_2PO_4 particles, *in preparation*

3.1 Abstract

Nanometer-sized particles of the solid acid fuel cell electrolyte material CsH_2PO_4 have been prepared by electrospray synthesis. Using a differential mobility analyzer to provide real-time particle-size information, the role of electrospray parameters, such as precursor solution composition, surface tension, conductivity, sheath gas temperature and flow rate, and solution flow rate, were evaluated. The observed trends revealed a set of parameters that enable the controlled generation of CsH_2PO_4 particles with sizes between 12 and 50 nm in diameter. The smallest of these particles are particularly promising for solid acid fuel cell electrodes because they are comparable in size to commercially employed platinum catalyst nanoparticles.

3.2 Introduction

State-of-the-art SAFCs deliver lower power densities than their SOFC and PEMFC counterparts, largely due to performance limitations at the cathode. [6] This component is generally constructed as a composite of the electrolyte material, which serves as the proton transport medium, and of nanoparticulate platinum electrocatalyst that is supported on carbon, which creates additional pathways for electron transport from the sites of electrocatalysis to the current collector. To date, a peak power density of 416 mW cm^{-2} has been achieved with a platinum loading of 7.7 mg cm^{-2}. [4] Significantly, it has been shown that the electrode performance scales inversely with the size of the electrolyte particles in the electrode structure, a phenomenon that has been attributed to the increase in the density of electrocatalytically active triple phase boundaries between the catalyst, the electrolyte and a gas phase with decreasing electrolyte particle size. [8] To minimize the voltage loss at the electrode (electrode overpotential) and, thereby, increase fuel-cell power density, we seek to substantially decrease the particle size while maintaining an interconnected, porous structure. Initial studies using electrospray deposition to fabricate SAFC electrodes produced electrolyte particles of about 100 nm in size, and dramatically reduced Pt loading below that of conventional SAFC electrodes, while maintaining comparable electrode activity. [33] Despite this advance, Pt loadings in SAFCs remain too high to be commercially viable in many applications. Thus, electrode feature sizes need to be reduced further, which should both reduce Pt loadings and increase activity. Efforts to produce electrolyte particles smaller than 100 nm have been delayed by the inability to explore the electrospray parameter space quickly due to the deposit-image-modify cycle that was employed in our earlier studies. Even when the electrospray was operated under conditions that should, according to well-established scaling rules for electrospray performance, produce particles in the low nanometer size regime, feature sizes remained large. It remains unclear whether the electrospray only produces particles above this size, or whether incomplete drying of the solution droplets emanating from the electrospray may be responsible for the large feature sizes. The hygroscopic,

low-melting-point materials used here pose particular challenges. Deposition of liquid droplets instead of nanoparticles may allow deposits to coalesce into structures that are much coarser than the particles from which they are formed. In the present work, we take an alternate approach to facilitate control the deposited structures. Instead of relying entirely on characterization of the final product, we introduce a process analytical technology to monitor the electrosprayed particles before they are deposited on the substrate. The instrument we utilize is the differential mobility analyzer (DMA), which provides real-time measurements of the particle size distribution of the aerosol produced by the electrospray. The DMA thus enables optimization of the electrospray prior producing an electrode, and monitoring of the electrospray aerosol while deposition is taking place [64, 65]. Using this technology, we demonstrate production of electrolyte particles with mean sizes as small as 12 nm, with the potential to, thereby, dramatically improve electrode performance.

Empirical scaling laws, describing initial electrospray jet and aerosol droplet diameter, generalized and validated experimentally by others [29, 45, 66–68], will be used as a guide to choose parameters for the generation of small CsH_2PO_4 particles.

3.3 Experimental procedure

3.3.1 Background and electrospray scaling

3.3.1.1 Electrospray

Generally in electrospray atomization, a liquid is supplied via a pump to a capillary that is held at a high voltage relative to a counter electrode, which may be the substrate. As the charged liquid emerges at the tip of the capillary, repulsive Coulombic forces are balanced by the surface tension. For low viscosity liquids, the fluid deforms into a so-called Taylor cone, a conical cusp that, at equilibrium, has a half-angle of 49.3°. [29, 55, 69] The electric field concentrates at the tip of the Taylor cone, stimulating the emission of a thin liquid jet of diameter $d_j \ll d_{capillary}$. Under appropriate operating conditions, the electric field induces instabilities in the capillary jet that result in emission of uniformly-sized droplets from an axially symmetric jet. [40] This mode of operation is called varicose break-up. The resulting aerosol droplets are driven toward the counterelectrode by the electric field. As they travel, the solvent evaporates, drastically increasing the areal charge density. When the charge per unit area on the droplets reaches the so-called Rayleigh limit, where repulsive Coulombic forces overcome the stabilizing surface tension, the droplets become unstable and form cusps much like the original Taylor cone. Progeny droplets are emitted from these cusps, carrying a small fraction of the mass, and much of the charge. [70] This process can occur multiple times until solute precipitation occurs and/or the droplet deposits onto a substrate.

3.3.1.2 Initial droplet size

Numerous theoretical and experimental studies have explored the relationship between electrospray parameters and the size of the emitted droplets under the varicose break-up regime. [29, 45, 66–68] Ganan-Calvo [45] presents an integrated analysis that unifies previous observations of different scaling laws under different experimental conditions. The author suggests that two dimensionless terms, representing a char-

acteristic liquid flow rate driven by inertial and viscous forces respectively times the actual flow rate:

$$\alpha_\rho = \frac{\rho K Q}{\gamma \varepsilon_0} \tag{3.1}$$

and

$$\alpha_\mu = \frac{K^2 \eta^2 Q}{\gamma^3 \varepsilon_0^2} \tag{3.2}$$

establishing bounds on the regimes of the electrospray.15 Here, ρ is the liquid density, K is the liquid electrical conductivity, Q is the liquid flow rate, γ is the liquid surface tension, ε_0 is the permittivity of vacuum, and η is the viscosity of the liquid. When $\alpha_\rho \gg \alpha_\mu^{1/4}$ and $\alpha_\rho/(\varepsilon_r - 1) \gg 1$, where ε_r is the relative dielectric constant of the liquid, inertial forces dominate over surface tension and viscous forces, and electrostatic forces dominate over polarization forces in cone-jet necking. As verified below, this regime applies here. Under these conditions the jet diameter d and electric current I are, respectively [Ganan-Calvo, J. Fluid Mechanics, 2004]

$$d_j = (\frac{\rho \varepsilon_0}{\gamma K)^{1/6}} Q^{1/2} \tag{3.3}$$

$$I = (\gamma K Q)^{1/2} \tag{3.4}$$

In this mode of operation, neither the viscosity of the liquid nor its dielectric constant affect the electrospray characteristic. For ease of analysis, expression 3.3 can alternatively be described in terms of dimensionless quantities

$$\frac{d_j}{d_0} = (\frac{Q}{Q_0})^{1/2} \tag{3.5}$$

where [Barrero, Ganan-Calvo, J. Aerosol Sci. 1997]

$$d_0 = (\frac{\gamma\varepsilon_0^2}{\rho K^2})^{1/3} \tag{3.6}$$

is the characteristic diameter of the electrospray, and

$$Q_0 = \frac{\varepsilon_0\gamma}{\rho K} \tag{3.7}$$

is the characteristic liquid flow rate. The diameter emitted, d_d, is comparable to that of the jet d_j. [67] Furthermore, the droplet charge, q, at emission approaches ($>$ 80%) the Rayleigh limit,

$$q^2 = 8\pi^2\varepsilon_0\gamma d_d^3 \tag{3.8}$$

at which the electrostatic repulsion by the charge on the droplet surface is balanced by the surface forces that resist that repulsion and hold the droplet together. [42] The current and fluid flow rate cannot be varied independently if one is to obtain a stable cone-jet emission (Eq. 3.4). Similarly, the voltage and current are largely interdependent, hence the appearance of only one of these three terms in establishing d_j. Moreover, Eq. 3.3 suggests that the initial droplet size should decrease with increasing surface tension.

3.3.1.3 Initial droplet velocity and relaxation

After the droplets are emitted, the electric field gradient (normally parallel to the direction of gas flow) drives them toward the substrate. The electric field at the tip of the Taylor cone, where radius r $\rightarrow$ 0, [71] is

$$E(r) = \sqrt[2]{\frac{2\gamma cos(\theta)}{\varepsilon_0 r}} \tag{3.9}$$

which introduces a singularity. Hence the Coulombic force dominates over all others at that point. The emitted droplets experience both the electrostatic force and aerodynamic drag, and rapidly approach a quasi-steady-state migration velocity. The characteristic time required to establish this steady-state velocity is called the

aerodynamic relaxation time, Seinfeld and Pandis [72]:

$$\tau = \frac{\rho d_d^2 C_c}{18\eta} \tag{3.10}$$

The droplets of interest here range from those initially emitted, which may be of order one micron diameter, much larger than the mean free path of the gas molecules. However, as they evaporate and undergo Coulombic explosions, the droplet size decreases into the free molecular regime. The Cunningham correction factor C_c accounts for the "slip" between the particle and the surrounding gas that develops in the transition from continuum to free molecular flow. Even at the initial droplet size, the relaxation time is short, milliseconds, so the droplet velocity quickly drops below the initial high value at the point of emission, rapidly approaching the gas flow velocity.

3.3.1.4 Droplet evaporation

During travel to the counterelectrode, the solvent in the droplets evaporates. Evaporation of multicomponent droplets has been studied experimentally and described with quasi-steady state evaporation models [50,73,74]. A good approximation for the evaporation rate of droplets can be obtained using the simple expression derived in Seinfeld and Pandis [72]:

$$d_d \frac{d_d}{dt} = \frac{S_{v,\infty} - S_{eq}}{D_v + \zeta} \tag{3.11}$$

where the numerator represents the driving force for evaporation, given by the difference between the ambient saturation $S_{v,\infty}$ and the equilibrium saturation S_{eq} of the droplet, Equation 3.12.

$$S_{eq} = exp(\frac{4M_W\gamma}{RT_\infty\rho d_d} - \frac{6n_s M_W}{\pi\rho d_d^3}) \tag{3.12}$$

D_v corresponds to the diffusivity of vapor, Equation 3.13 and ζ are based on an energy balance and predicts the effect of any temperature difference between the droplet its environment into account, Equation 3.14.

$$D_v = \frac{\rho R T_\infty}{4 p^0 T_\infty D'_v M_W} \tag{3.13}$$

$$\zeta = \frac{\Delta H_v \rho}{4 k'_a T_\infty} \left(\frac{\Delta H_v M_W}{T_\infty R} - 1 \right) \tag{3.14}$$

Here, M_w is the molecular weight of the solvent, γ the surface tension, n_s the number of moles of solute, R the ideal gas constant, T_∞ the temperature of the environment, ρ the solution density, p^0 the saturation vapor pressure, D'_v the modified vapor diffusivity, ΔH_v the latent heat of evaporation, and k'_a the effective thermal conductivity of air. Using pure water as the solvent for the calculations gives the upper bound for the time till full evaporation of the electrosprayed droplets, since the presence of a significantly more volatile methanol component is expected to result in a faster evaporation rate. Concomitant to the decrease of the droplet radius is the increase in the surface charge density. As the charge density approaches the Rayleigh limit, the droplet undergoes a fission event in which multiple small secondary droplets, with sizes less than 5% that of the parent, are emitted, whereas the loss of charge is much greater, on the order of 15 - 40%. This process is described by the charge residue model (CRM) [22, 46, 52, 55, 72, 75] and has been observed experimentally by Hartman et al. [40], Smith et al. [70] and others. Thus, the fission event has little influence on the parent droplet size, but increases the particle size distribution through the generation of progeny in a distribution which itself is less monodisperse than the original distribution. [47] In the absence of Coulomb fission events, the aerosol size distribution broadens during drying as a result of the faster drying of smaller droplets, but at the stage when all of the solvent has been evaporated and only the solute residue remains, the original size distribution is recovered.

3.3.1.5 Solute precipitation

Because nucleation of the crystal phase is a kinetically constrained process, highly supersaturated droplets may persist long after the solubility limit is reached. When nucleation does occur, the particle morphology can vary widely. Slow evaporation

and fast diffusion of the solute, nucleation and growth of a particle typically leads to solid particles (volume precipitation). Fast evaporation on the other hand can lead to significant solute concentration gradient in the droplet so that hollow particles may form (surface precipitation). [55, 69, 75]

3.3.2 Parameter variation

To summarize, the initial droplet size, evaporation rate, and droplet disintegration process, and hence ultimate particle size are influenced by both the solution properties and the process parameters. [40, 76] As a specific example, the electrospray temperature and nitrogen carrier gas flow rate will impact the solvent evaporation rate. Similarly, the surface tension, which depends on the solution composition, can be expected to influence the droplet size at which Coulombic repulsion due to charge concentration overcomes surface tension forces (Rayleigh limit) and induces droplet disintegration. Thus, the final particle size distribution may depend on the surface tension. Key parameters were varied to determine their impact on particle size distribution. Given the breadth of the parameter space, the problem was parsed by retaining a "default set of parameters" and varying only one at a time. The parameters to be varied were determined from our earlier attempt at optimizing deposition of porous solid acid fuel cell electrode structures in which we relied on scanning electron microscopy to determine these effects. [33] In terms of solution properties, the CsH_2PO_4 concentration, the methanol-to-water ratio, and the Polyvinylpyrrolidone (PVP) surfactant concentration were varied. Among process parameters, voltage, temperature, nitrogen flow rate, and precursor solution flow rate were varied. The ranges explored for these parameters as well as the default values are summarized in Table 3.1. The range of parameter space accessible (in particular the voltage and precursor liquid flow rate) was limited to those conditions that yielded a stable Taylor cone jet-spraying mode. The stability of the spray was monitored both by visual observation through the viewing port of the electrospray apparatus. Erratic fluctuations of the Taylor cone were interpreted as warnings that other spraying modes,

Table 3.1: Parameters varied in electrospray deposition process. The sprayed solution consists of CsH_2PO_4 dissolved in a water-methanol mixture, in some cases with PVP added as a surfactant

	Methanol (wt%)	CsH_2PO_4 (g/L)	PVP (g/L)	Temp (°C)	N_2 flow rate (cm^3/min)	Liq flow rate* (ml/h)	Voltage* (kV)
Range	22-53	0.5-10	1-30	22-120	200-1200	0.5-2.5	4.9-5.75
Default	53	5 or 10	1	100	1000	0.5	5

such as the multijet, pulsating, or dripping mode had emerged. [34] Such conditions were avoided.

*The voltage and liquid flow rate settings cannot be varied entirely independently as they are restricted to values that yield a stable Taylor cone and constant particle concentration.

3.3.3 Materials preparation and solution characterization

CsH_2PO_4 was synthesized from aqueous solution as described elsewhere. [15] In brief, stoichiometric quantities of $CsCO_3$ and H_2PO_3 were dissolved in deionized water. Methanol was added to the solution to induce precipitation. The identity of the precipitate was determined by X-ray powder diffraction. Values of the solution properties that influence the electrospray process were measured experimentally. The solubility of CsH_2PO_4 was measured by light scattering methods. CsH_2PO_4 powder was added incrementally to the room temperature solution under continuous stirring, while observing the light scattering that resulted from shining a conventional laser light on the solution by the naked eye. If scattering was observed beyond one hour of stirring, the solution was considered to be beyond the saturation limit. The conductivity of prepared solutions was measured using a digital conductivity meter (Omega CDH-7X, applied DC voltage: 10 mV), with fixed stainless steel electrodes that were cleaned prior to the measurements. The surface tension of selected solutions was measured via the DuNuoy ring method, using a Cenco Interfacial Tensiometer (Precision direct

reading model, Ser. No. 909) and a CSC Scientific Inc. platinum ring (Cat. No. 70542, mean circumference 5.992 cm). In our previous work, PVP was used for stabilizing colloidal suspensions of platinum catalyst nanoparticles in the electrospray solution and, thus, as a means of incorporating such catalysts into the deposited electrodes. Accordingly, the influence of PVP (Alfa Aesar, Stk# 41626 MW 8000) on all of the above solution properties was also evaluated here.

3.3.4 Electrospray apparatus

The electrospray apparatus constructed for the fabrication of nanoparticulate CsH_2PO_4 has been described previously. [33] Briefly, the system consists of a heated chamber into which the CsH_2PO_4 solution is supplied by mechanical pumping through an electrically-biased stainless steel capillary that was positioned to electrospray upwards, as shown in Fig. 3.1.

The large voltage difference (4.9 to 5.8 kV) between the capillary tip and the grounded collection tube (ID 4.8 mm, OD 20 mm) exiting from the top of the chamber extracts droplets from the capillary and drives them towards the exit. The highly charged aerosol particles are convected rapidly by both the electrospray electric field and the carrier gas flow (default value of 8.5 mm/sec linear flow velocity; 3 sec residence time in the electrospray chamber). Evaporation of the solvent during flight, as described above, induces charge concentration on the droplet surface, which in turn leads to droplet disintegration. Based on the very short relaxation time of ~ 5 μs, we can neglect the initial high velocity of the droplets due to the singularity of the electric field at the tip of the Taylor cone. Thus, a flight path length of 2.5 cm (the default capillary to substrate distance) provides sufficient time, on the order of a second, for complete solvent evaporation so that already deposited particles do not re-dissolve on the substrate. Based on equations 3.5 and 3.11, a minimum of 1-3 ms is required for full solvent evaporation for 1-3 μm diameter initial droplet size.

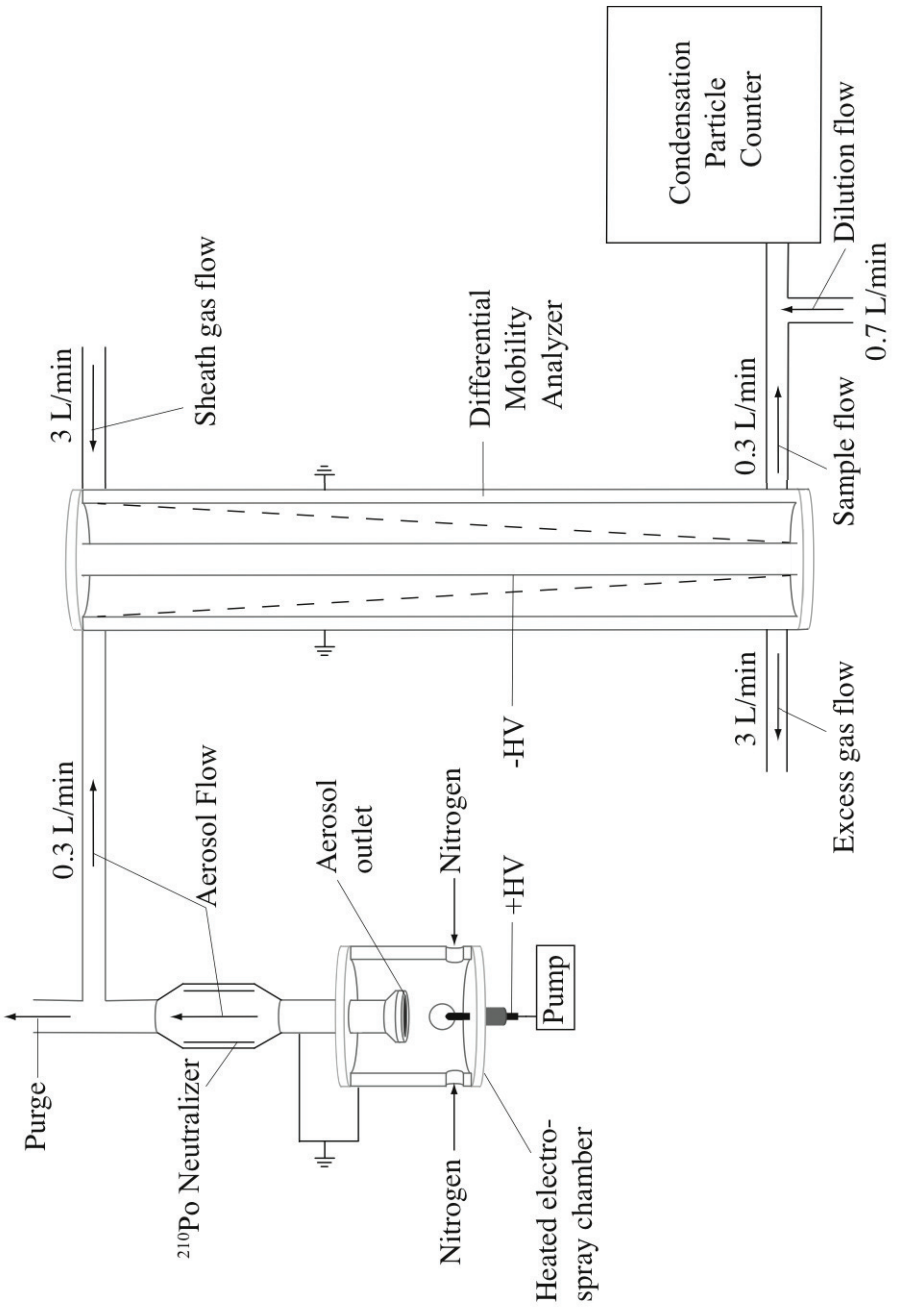

Figure 3.1: Schematic of the electrospray apparatus with integrated differential mobility particle sizer, including ^{210}Po neutralizer, differential mobility analyzer, and condensation particle counter

3.3.5 Product aerosol characterization

We seek to characterize the particles that are produced by the electrospray in the form that they exist at the point of deposition on the substrate. To accomplish this task, a sampling orifice is installed at the center of and electrically grounded temperature controlled disk that has the same dimensions as the substrate and its holder that we use in fabricating the fuel cell electrodes. A small flow of aerosol is extracted rom the chamber through this orifice for subsequent analysis using an on-line aerosol particle size distribution measurement system. The core of this instrument is the differential mobility particle analyzer (DMA), which classifies charged aerosol particles according to the velocities with which they migrate across the particle-free sheath gas flow that is confined between coaxial cylindrical electrodes that are held at different voltages. Those particles that cross the gap in the time it takes to flow from an inlet port in one electrode to a downstream outlet port in the counter electrode are extracted and counted. Thus, only particles within a narrow range of electrophoretic mobilities contribute to the signal at any voltage setting. The ratio of the range of mobilities transmitted to that of the optimally transmitted particles scales as the ratio of the volumetric flow rate of the aerosol to that of the larger, particle-free sheath gas. The distribution of particles with respect to mobility is determined by stepping the voltage applied between the DMA electrodes over a range that is bounded by the electrostatic breakdown at the high end and the onset of diffusional degradation at the low end. [77]

To translate the mobility distribution into a size distribution, we note that the electrophoretic mobility of a spherical particle of diameter D_p and charge q is

$$Z_p = \frac{qC_c\frac{2\lambda}{D_p}}{3\pi\mu_p} \tag{3.15}$$

where C_c is a slip correction factor and Î» is the mean-free-path of the gas molecules. For small nanoparticles, in the free molecular limit, $Z_p \ \alpha \ qD_p^{-2}$. The charge on a particle must, therefore, be known to determine its size. Ideally, measurements are made on singly charged particles, but the electrospray produces much

more highly charged particles. A known charge distribution is produced by exposing the particles to an electrically neutral cloud of positive and negative gas ions, in a so-called aerosol neutralizer that is placed upstream of the DMA. In this environment, the aerosol attains a steady-state charge distribution in which a small but known fraction of particles carries a single elementary unit of charge, i.e. $q = \pm e$. [78] The classified nanoparticles are carried by the gas flow from the DMA to a condensation particle counter (CPC), in which they are grown to a sufficiently large size that they can be counted optically. Measurements of the classified particle concentration are made as a function of applied voltage. The DMA voltage was varied between 84 V to 500 V, with step sizes linearly varying from 8.2 V to 17 V. At the operating flow rates, this corresponds to a particle size range from 10 to 100 nm. Periodically, a wider particle size range was scanned with voltages ranging from 84 V to 5.2 kV and step sizes varying linearly from 8.2 V to 40 V, corresponding to a particle size range of 10 to 500 nm. The measurement time was 10 sec at each step, with the concentration recorded every second, i.e. 10 measurements per step. The transients between the size steps were deleted and the concentration data for each size step averaged and adjusted for aerosol particle-size-dependent charging statistics described by Hoppel Frick (1986) [78] and manufacturer specified counting efficiency of the CPC. The raw data (counts vs. applied voltage) was inverted to obtain the size distribution for each electrospray condition using the method of by Stolzenburg and McMurry (2008) [79]. The resulting distribution was subsequently fitted to a log-normal function - the standard distribution function for dilute nanometer sized aerosol particles - from which the geometric mean diameter, D_g, and geometric standard deviation was obtained, see Figure 3.3. The full particle size distribution was determined multiple times for a given set of parameters to ensure reproducibility and to enable measurement of experimental uncertainty. Observations of increasing uncertainty in the measured mean diameter provided a direct indication of fluctuations induced by electrospraying instability as the boundary of the stable Taylorcone spray mode was reached. [80] The DMA was calibrated with standard polymer spheres (21, 59, 82, 92, 105 nm diameter, Nanosphere Size Standards, Duke Scientific Corp.) dispersed in de-ionized water and

aerosolized via a standard particle nebulizer, Figure 3.2 [81].

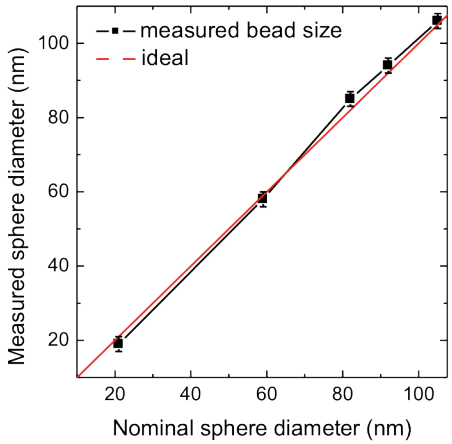

Figure 3.2: Calibration of differential mobility particle sizer with polystyrene beads

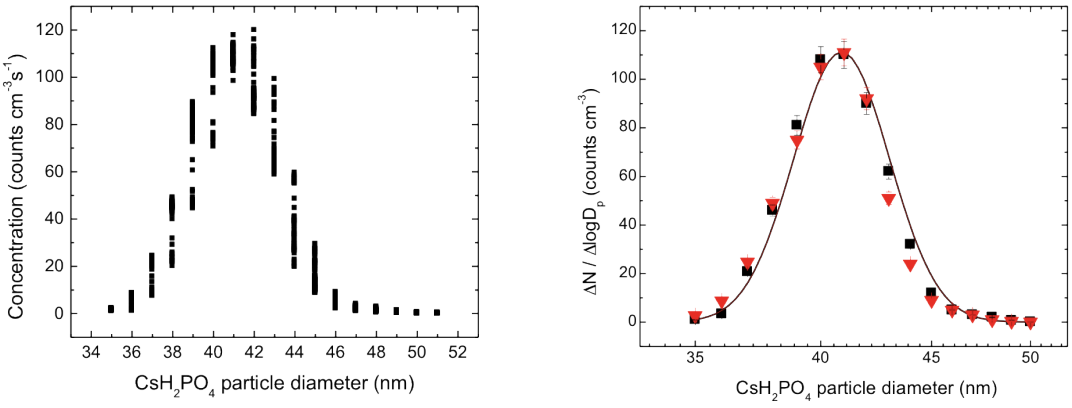

Figure 3.3: Example of particle size measurements and data analysis. (a) Counts (cm^{-3} s^{-1}) as a function of particle diameter, multiple measurements, as detected at discrete particle sizes; and (b) averaged values and fit to a log-normal distribution

3.4 Results

3.4.1 Solution properties

The solubility limit for CsH_2PO_4 in water methanol mixtures determined here is presented in Figure 3.4. The solubility decreases exponentially with increasing methanol content, from 137.9 g/L in 100% H_2O to 0.5 g/L in 90 wt% methanol, and undetectable solubility in 100% methanol. These values set the limit of the maximum CsH_2PO_4 concentration that can be used in the electrospray solutions. Use of solutions with CsH_2PO_4 concentrations no higher than ∼50 wt% of the solubility limit ensured that the electrospray nozzle would not clog during operation over longer time periods (>1 hour). The default methanol concentration of 53 wt% corresponds to a CsH_2PO_4 concentration of ∼5 g/L.

Varying the CsH_2PO_4 concentration has a dramatic impact on the solution conductivity, but limited impact on the surface tension of the solution, as inferred from Figure 3.5

Both the conductivity and surface tension results are in line with expectations for

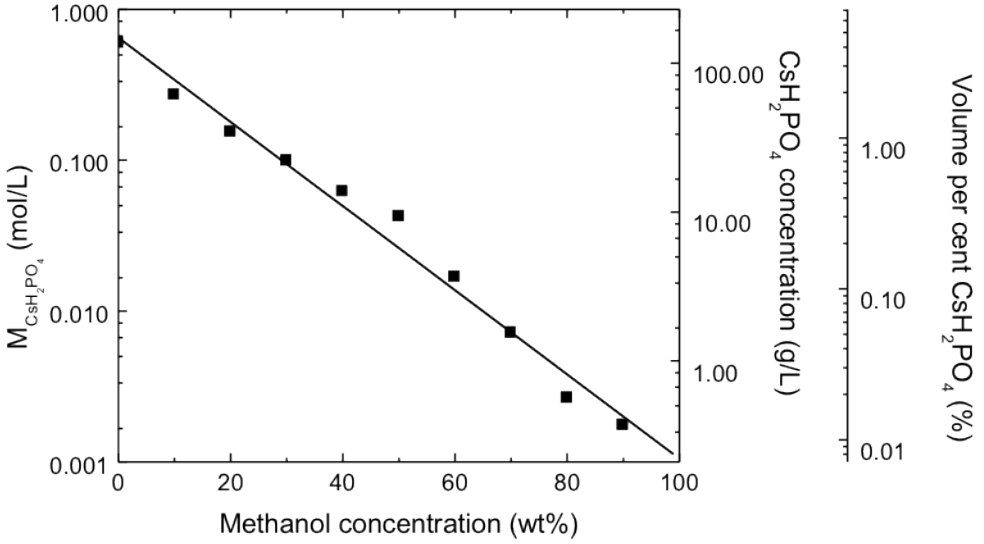

Figure 3.4: Solubility limit of CsH_2PO_4 in water-methanol mixtures

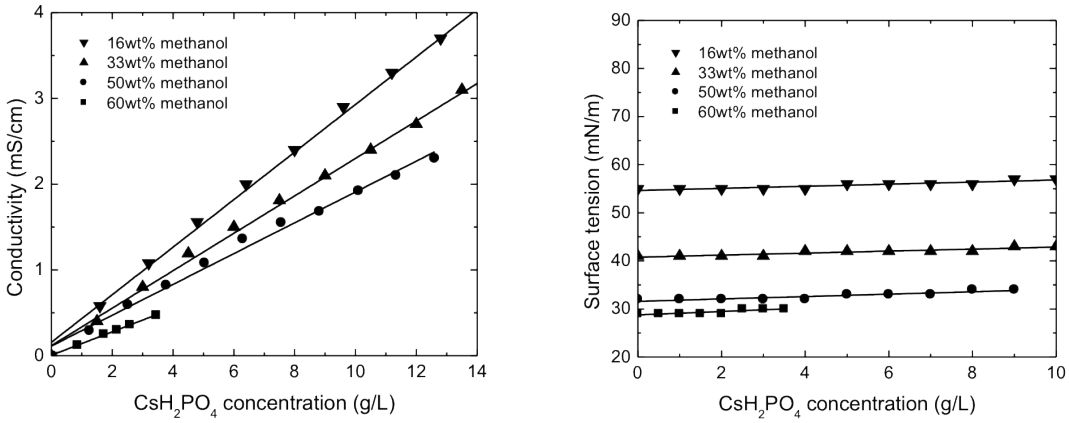

Figure 3.5: Conductivity and surface tension of precursor solutions with 16 wt%, 33 wt%, 50 wt%, and 60 wt% methanol in water vs. CsH_2PO_4 concentration

introducing ions into an aqueous solution. The measured values for the surface tension of pure distilled water and pure methanol at room temperature, with values of 73.4 mN/m and 22.5 mN/m respectively, are in excellent agreement with the literature.

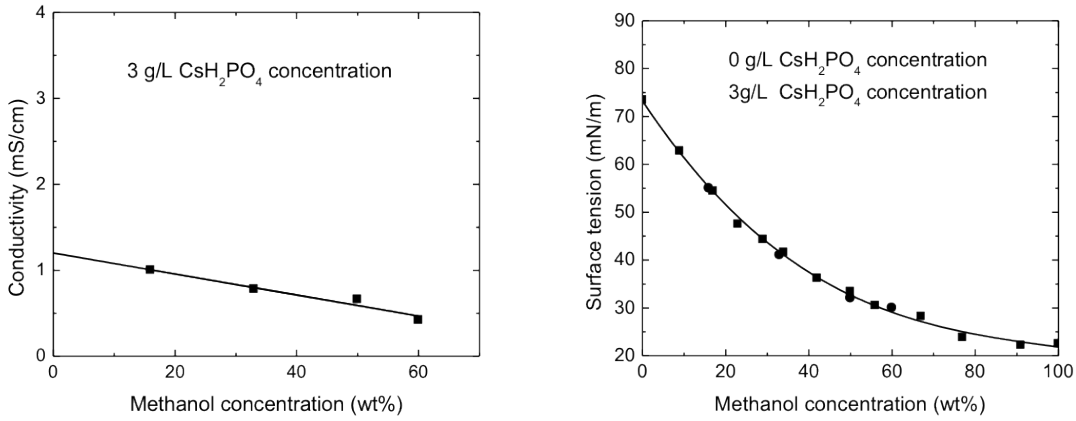

Figure 3.6: Conductivity and surface tension of precursor solutions vs. methanol concentration(3 g/L CsH_2PO_4 concentration and no CsH_2PO_4, respectively)

PVP has a negligible effect on both the solution conductivity and surface tension, see Figure 3.7.

Figure 3.8 shows a linear increase of the current carried by the aerosol particles with applied capillary voltage. When a ^{210}Po neutralizer is added before the aerosol particles reach the grounded probe, a nearly zero current is observed, indicating good neutralizing efficiency.

3.4.2 Particle size trends

Figure 3.9a shows representative particle size distributions for multiple CsH_2PO_4 concentrations, and the corresponding log-normal. Figure 3.9b. summarizes the impact of CsH_2PO_4 concentration on the mean particle size, obtained from the log-normal fitting of curves in Figure 3.9a, with the standard deviation of the distribution indicated. With increasing CsH_2PO_4 concentration, we observe a significant decrease of the particle diameter, leveling off at $\sim$ 25 nm, and a narrower size distribution. A

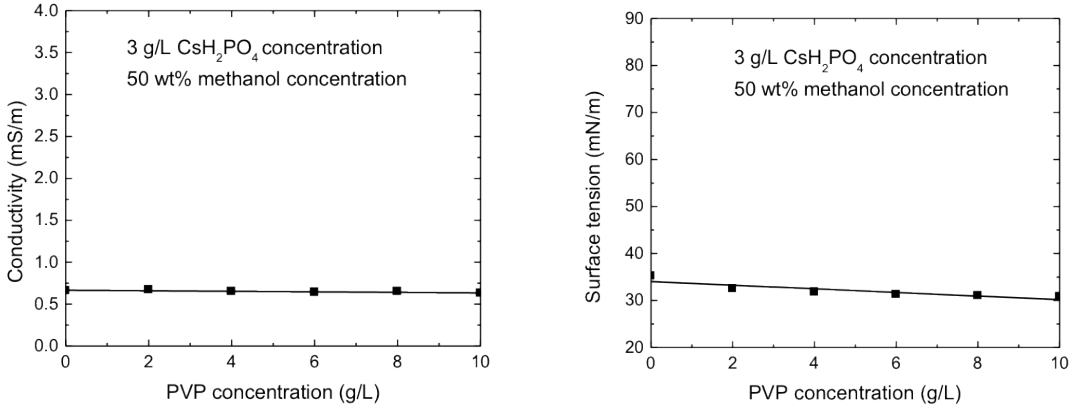

Figure 3.7: Conductivity and surface tension of precursor solutions vs. PVP concentration

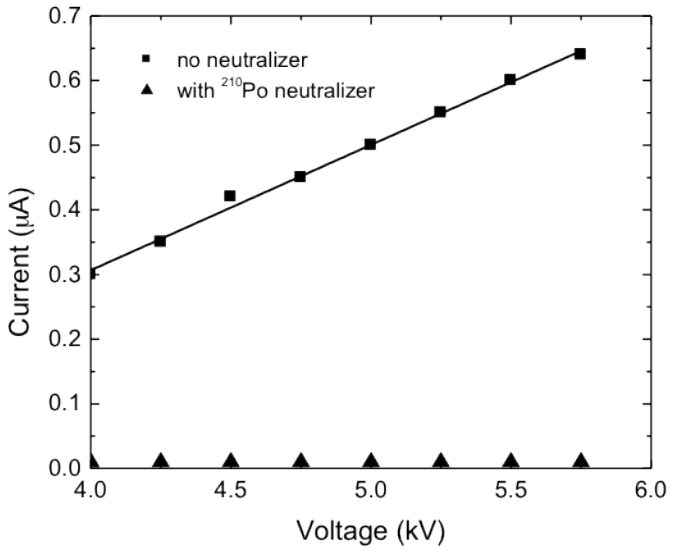

Figure 3.8: Current carried by the charged aerosol flux vs. electrospray capillary voltage measured with a picoammeter

decrease in the initial droplet size vs. CsH_2PO_4 concentration was calculated (open circles), using equation 3.5 and the measured precursor solution properties.

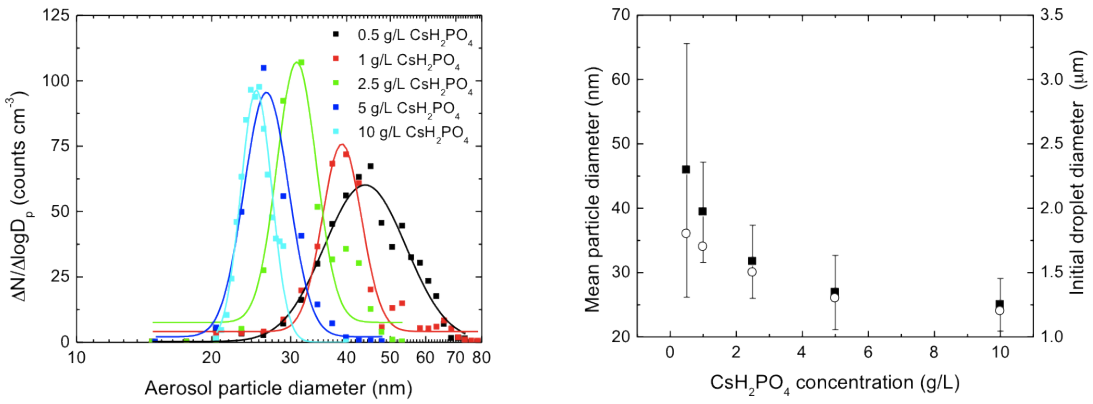

Figure 3.9: Aerosol particle size distributions with log-normal fitting for varying CsH_2PO_4 concentrations b) Mean particle size of aerosol vs. CsH_2PO_4 concentration with standard deviation of the distributions indicated (solid squares) and calculated initial droplet size (open circles)

Figure 3.10a shows representative particle size distributions for varying methanol concentrations of the precursor solution, including log-normal. Figure 3.10b summarizes the impact of methanol concentration on the mean particle size. Here the CsH_2PO_4 concentration is fixed at 5 g/L and no other components are added to the solution. With increasing methanol concentration in the precursor solution, the mean particle diameter varies only slightly. At 22 wt% and 53 wt% methanol concentration, a less stable spraying mode (pulsating mode) was observed, corresponding to low particle concentrations and a broad particle size distribution. At 25 and 36 wt% methanol, we observe the narrowest particle size distribution and the highest measured concentration, respectively. The calculated initial droplet size does not vary significantly with varying methanol concentration (open circles).

Similarly, the precursor solution flow rate can be varied within a range, controlled by the stability of the Taylor cone spraying mode. [20] We observed both a reduction in CsH_2PO_4 particle size and a narrower particle size distribution with a decrease in precursor solution flow rate, Figure 3.11. At flow rates higher than 2.5 ml/h, the

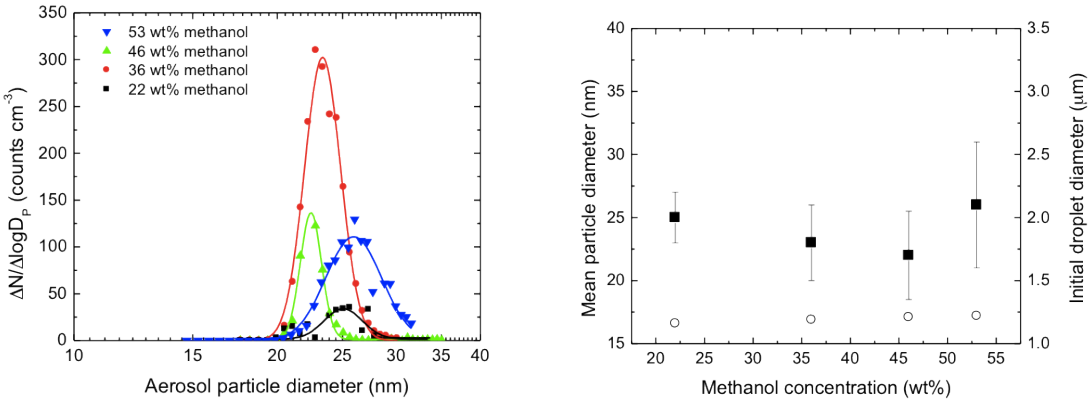

Figure 3.10: Aerosol particle size distributions with log-normal fitting for different methanol concentrations b) Mean particle size of aerosol vs. methanol concentration with standard deviation of the distributions indicated

dripping mode was observed. At flow rates lower than 0.5 ml/h, the Taylor cone disappeared periodically and clogging of the capillary tip occurred frequently. The particle size distribution is narrowest at 0.5 ml/h. The calculated initial droplet size increases linearly with increasing solution flow rate.

When the surfactant PVP is added to the electrospray precursor solution, the mean particle diameter increases monotonically, Figure 3.12. We observe the narrowest particle size distribution with the highest peak concentration at 10 g/L, indicating a stable spraying mode.

Figure 3.13a shows minimal variation in the mean particle size as the electrospray voltage is varied over the narrow range of 4.9 to 5.75 kV, limited by the stability of the Taylor cone spraying mode. More significant is the narrowing of the particle size distribution as voltage is increased. Figure 3.13b, shows a significantly broader particle size distribution at the lower bound of the applied voltage. At voltages higher than 5.75 kV, corona discharge and/or occasional dielectric breakdown is observed and is to be avoided.

The particle size exhibits a broad minimum with electrospray temperature (heated gas lines, chamber, and substrate). Smaller electrolyte particles are seen at 60 and 100°C, with a significantly larger particle size and higher concentration at 120°C as

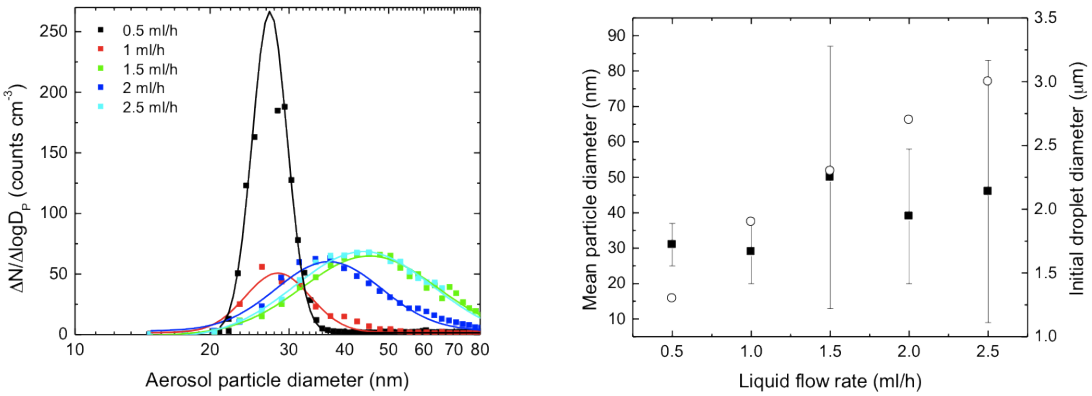

Figure 3.11: a.) Aerosol particle size distributions with log-normal fitting for different precursor liquid flow rates b) Mean particle size of aerosol vs. precursor liquid flow rate with standard deviation of the distributions indicated (solid squares) and calculated initial droplet size (open circles)

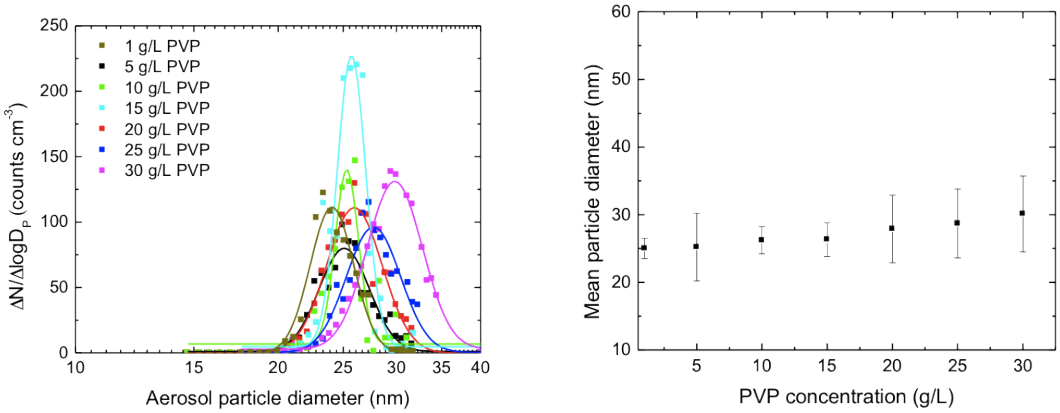

Figure 3.12: a.) Aerosol particle size distributions with log-normal fitting for different PVP concentrations b) Mean particle size of aerosol vs. PVP concentration with standard deviation of the distributions indicated.

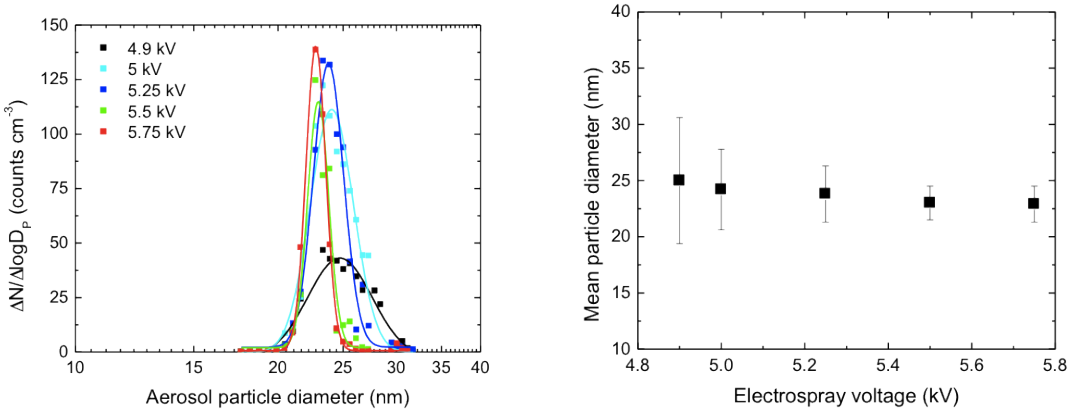

Figure 3.13: a) Aerosol particle size distributions with log-normal fitting for different voltages at the electrospray capillary b) Mean particle size of aerosol capillary voltage with standard deviation of the distributions indicated

shown in Figure 3.14. The particle size distributions were significantly narrower at the intermediate temperature range. The final parameter giving a reduction of the electrolyte particle size is the nitrogen sheath gas flow rate. The increased nitrogen sheath gas flow rate results in a significant initial decrease in particle size and a narrower particle size distribution.

A combination of the parameters giving the smallest mean particle size for each parameter variation separately, and a stable electrospray mode, see Table 3.1, resulted in the generation of $\sim$ 12 nm diameter CsH_2PO_4 particles, shown in Figure 3.15, a result confirmed with atomic force microscopy and scanning electron microscopy images (not included here). 10 nm represents the detection limit of the employed DMA.

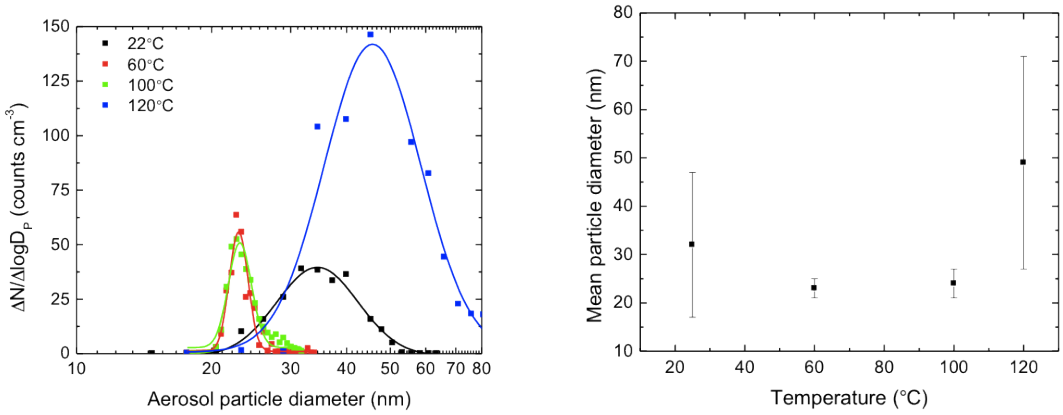

Figure 3.14: a.) Aerosol particle size distruibutions with log-normal fitting for different electrospray temperatures b) Mean particle size of aerosol vs. electrospray temperature with standard deviation of the distributions indicated

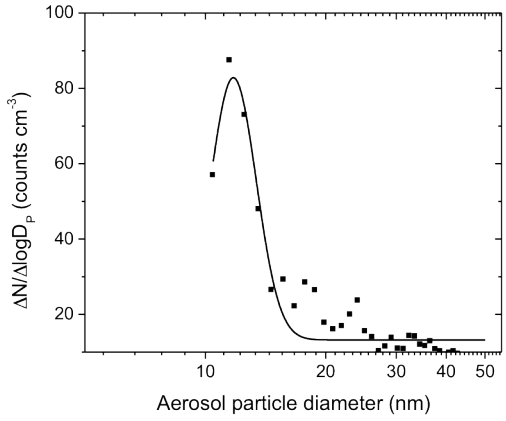

Figure 3.15: Electrosprayed CsH_2PO_4 particle size distribution with optimized electrospray parameters showing 12 nm diameter particles

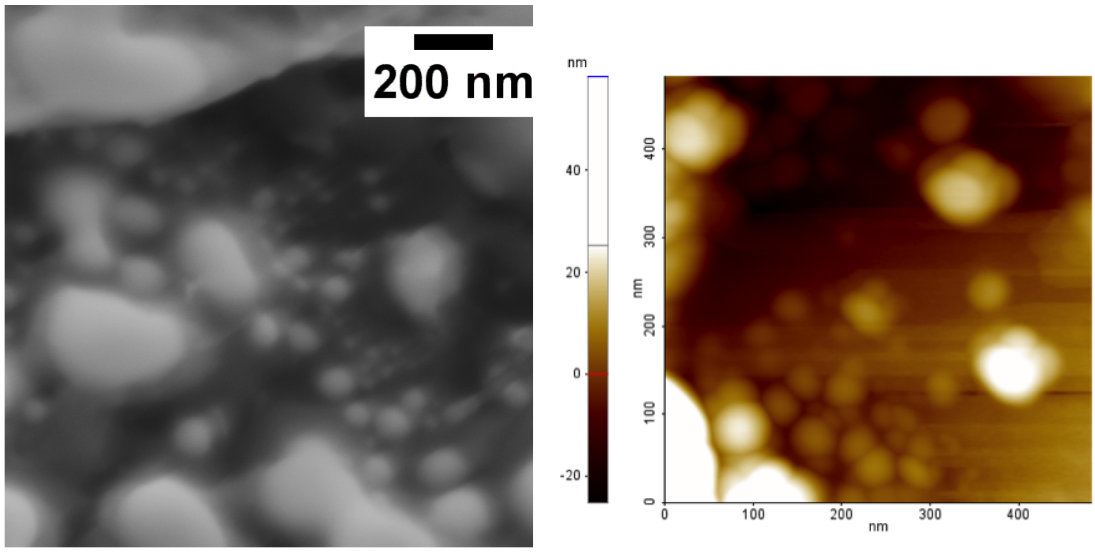

Figure 3.16: a)SEM and b) AFM image of 12 nm CsH_2PO_4 particles

3.5 Discussion

Generally, the trends in the aerosol particle size distribution may be explained by the models for the initial droplet formation from the Taylor cone, the evaporation-fission sequence, and solute precipitation, as summarized above.

An increase in CsH_2PO_4 concentration results in a considerable increase in conductivity of the precursor liquid for the electrospray. A higher solution conductivity may be expected to result in smaller initial aerosol droplets, according to Equation 3.3. The calculated initial droplet size follows the general trend of the final particle size but it is not marked enough to explain the decrease in the final particle size. In addition, the increase in solute concentration has the opposing effect of particle size reduction in case the initial droplet size were to remain constant. We speculate that more frequent Coulomb fission events due to a higher charge concentration on the droplets, as a result of faster charge transfer to the droplet at higher liquid conductivities, may lead to smaller final particle sizes. We also observe a decrease in the standard deviation, i.e., a more monodisperse particle size distribution with increasing CsH_2PO_4 concentration, consistent with a more stable Taylor cone. A CsH_2PO_4 concentration larger than 5 g/L leads to frequent clogging of the capillary and hence is not suitable

for long-term operation (>1 hour). The slight increase of the mean particle diameter with increasing methanol concentration is consistent with the decreasing surface tension and conductivity of the solution, according to Equation 3.3; Multiple researchers have observed that a decreasing the water-methanol ratio allows faster evaporation of the solution. [82, 83] and, with that, more frequent droplet disintegration.

The third parameter that influences the initial droplet size is the precursor liquid flow rate. The increase in the final particle size can be explained by the calculated increase in the initial droplet diameter, based on Equation 3.3. The most stable spraying mode giving the narrowest particle size distribution was observed at 0.5 ml/h precursor flow rate. The particle concentration and the width of the distribution deteriorate significantly at higher flow rates.

The slightly lower surface tension with increasing PVP content does not impact particle size. The added volume of the surfactant as a skin on the electrolyte particles likely influences the evaporation rate by lowering it.

When the applied capillary voltage is increased, the droplets were observed to be charged to a higher fraction of the Rayleigh limit. [84] thus more frequent droplet disintegration is expected. [52] Since the range of the voltage variation is very limited, the particle size reduction at the high end of the applied voltage range is also barely detectable. The width of the particle size distribution on the other hand becomes much narrower as voltage is increased, most likely due to a more stable Taylor cone spraying mode.

When the electrospray temperature is varied, the reduction of the mean particle diameter can be explained by the higher evaporation rate of the solvent. A higher solvent evaporation rate allows more frequent fission events leading to smaller electrolyte particles. At very high evaporation rates, hollow particles with larger diameters are generated as in other salt containing liquid systems [55], explaining the marked increase in the mean particle diameter and the width of the particle size distribution, without the increase of the solute supply rate.

Finally, an increase in the nitrogen flow rate effectively reduces the partial pressure of the solvents and hence increases the evaporation rate, according to equation 3.11

in addition to possible convective effects, leading to more frequent fission events and smaller electrolyte particles.

The surprisingly marked decrease in the measured final particle size when the optimized set of parameters was used indicates that the determined particle size trends for each parameter is valid when other parameters are changed, but the magnitude may vary significantly. For example, the influence of the electrospray temperature on the final droplet size may be much more significant when the methanol concentration of the precursor solution is higher.

3.6 Conclusion

In situ aerosol size monitoring using differential mobility analysis enabled efficient characterization of the electrospray parameter space, including the precursor solution composition, surface tension, conductivity, and flow rate, the electrospray sheath gas temperature, flow rate, and electrospray voltage. The process established here yielded insights into the influence of certain parameters on the final particle size. This process can be applied to other aerosol nanoparticle deposition or production systems to facilitate rapid, in situ exploration of the large parameter space that must be explored to optimize nanoparticle synthesis methods.

The most significant parameters influencing the final particle size in the present electrospray system were found to be solute concentration, electrospray temperature, and nitrogen flow rate, each of which results in a decreased mean particle diameter as its value is increased.

It is interesting to note the size difference between the deposited CsH_2PO_4 nanoparticles with a $\sim$100 nm feature size as observed with a scanning electron microscope6 and the consistently smaller particle size of $<$50 nm as measured with the differential mobility particle sizer. The results presented here provide two possible explanations for the size discrepancy. If fully dry nanoparticles are measured by the differential mobility particle sizer, then, all else being equal, the process parameter nitrogen carrier gas flow rate should not have a significant impact on the particle size, as it only influences the speed at which the droplets go through the evaporation-Coulomb fission-evaporation sequence. But if the droplets entering the neutralizer still contain solvent, a further reduction in particle size due Coulomb fission events is prevented, hence at low nitrogen carrier gas flow rates we observe larger particles than at high flow rates. The significantly larger feature size of $\sim$100 nm of deposited CsH_2PO_4 can be explained by the presence of solvent in the droplet when deposited, which is not sufficient to re-dissolve the already deposited porous, fractal structure, but enough to prevent the crystallization of sub-100 nm particles. Increasing the capillary to substrate distance may lead to smaller, dry particles depositing. Furthermore, the low

melting temperature of 345°C, and the high hygrocopicity of CsH_2PO_4 explain fast agglomeration of the nanoparticles even at ambient conditions without a stabilizing agent.

Depending on the possibility of stabilizing the nanometer phases and allowing fully dry CsH_2PO_4 nanoparicles to deposit on a substrate, this result opens the opportunity for fabricating composite solid acid fuel electrodes that have the ideal structure consisting of percolating, porous networks of 12 nm CsH_2PO_4 particles. These structures hold the promise of much improved catalyst utilization allowing for significantly enhanced fuel cell power density values with equal platinum loading to traditional, mechanically milled electrodes.

Chapter 4

Nanocomposite solid acid fuel cell electrodes via electrospray deposition

Adapted with permission from: A. Varga, N. A. Brunelli, M. W. Louie, K. P. Giapis, S. M.Haile, Composite Nanostructured Soli-Acid Fuel-Cell Electrodes via Electrospray Deposition. *Journal of Materials Chemistry* **2010**, 20, 6309 - 6315

4.1 Abstract

Stable, porous, nanostructured composite electrodes were successfully fabricated via the inexpensive and scalable method of electrospray deposition, in which a dissolved solute is deposited onto a substrate using an electric field to drive droplet migration. The desirable characteristics of high porosity and high surface area were obtained under conditions that favored complete solvent evaporation from the electrospray droplets prior to contact with the substrate. Solid acid (CsH_2PO_4) feature sizes of 100 nm were obtained from electrosprayed water-methanol solutions with 10 g L_{-1} CsH_2PO_4 and 5 g L^{-1} Pt catalyst particles suspended using polyvinylpyrrolidone (PVP). Alternative additives such as Pt on carbon and carbon-nanotubes (CNTs) were also successfully incorporated by this route, and in all cases the PVP could be removed from the electrode by oxygen plasma treatment without damage to the structure. In the absence of additives (Pt, Pt/C and CNTs), the feature sizes were larger, $\sim$ 300 nm, and the structure morphologically unstable, with significant coars-

ening evident after exposure to ambient conditions for just two days. Electrochemical impedance spectroscopy under humidified hydrogen at 240° C indicated an interfacial impedance of $\sim 1.5\ \Omega\ \mathrm{cm}^2$ for the $\mathrm{Pt}/\mathrm{CsH_2PO_4}$ composite electrodes with a total Pt loading of 0.3 ± 0.2 mg cm^{-2}. This result corresponds to a 30-fold decrease in Pt loading relative to mechanically milled electrodes with comparable activity, but further increases in activity and Pt utilization are required if solid acid fuel cells are to attain widespread commercial adoption.

4.2 Introduction

The power output of even the most advanced SAFCs have not yet reached levels typical of conventional polymer electrolyte or solid oxide fuel cells, largely due to poor activity of the electrodes. That is, while it has been possible to limit electrolyte voltage losses in SAFCs through fabrication of thin-membrane fuel cells (with electrolyte thicknesses of 25-50 μm), it has not been possible to attain high activity electrodes or lower Pt loadings to competitive levels. [6, 8] Because the components in SAFC electrodes (Pt, CsH_2PO_4, and pores) can each transport only one species (electrons, protons, and gas-phase molecules, respectively), one can surmise that the electrocatalysis reaction is limited to the triple-phase boundaries at which the electrolyte, catalyst and the gas phase are in contact and where the simultaneous and coordinated transport of electrons, ions, and gas molecules can occur. Maximization of the triple-phase boundary per unit projected area is thus a recurring theme in composite electrode systems. [85] In the case of SAFC electrodes, the possibility of attaining a high density of TPBs as implied through the use of nanoparticle Pt has not been realized because of the typically large size of the electrolyte particles. At the submicron scale, recent studies have demonstrated a monotonic increase in fuel cell power output with decreasing electrolyte particle size, [8] suggesting that further reductions into the nanoscale regime would indeed create extensive triple-phase contacts and dramatically enhance electrocatalytic activity. Beyond maximizing TPBs, a composite electrode must also ensure continuous pathways for ion, electron and gas phase transport. Accordingly, the aim of the presented work is to fabricate an interconnected, porous, three-dimensional nanostructured composite. Ultimately, such a structure may provide the dual benefits of enhanced electrochemical activity and reduced Pt loading. The fabrication methodology utilized here is the electrospray technique. Electrospray has been widely used for aerosolizing liquids. [86] It relies on electrostatic forces to expel micrometer sized droplets from a charged liquid. The liquid is pumped through a capillary, and, under ideal conditions, the applied electric field causes the liquid to emerge in the shape of a cone, called the Taylor cone. [20]

The high electric field concentrated at the tip of the cone induces the emission of a fine spray of charged droplets. If the liquid is a solution of solvent and solute and sufficient evaporation occurs as the droplets are accelerated towards the grounded substrate, the resulting charge concentration induces break-up of the droplet and the ultimate deposition of sub-micron to nanoscale particles on the substrate. A wide range of chemical and physical parameters can be varied to tune the characteristics of the resultant structure, which can span from dense thin films to porous electrodes [32,87,88]. These parameters include solvent concentration, solution composition (affecting solution conductivity, surface tension, viscosity), spraying temperature, gas flow rate, and spray geometry (e.g. tip-to-substrate path length, spraying direction). Here we demonstrate that, under the appropriate set of conditions, the electrospray method can be employed to obtain porous electrode structures for solid acid fuel cells.

4.3 Experimental procedure

4.3.1 Materials

The electrolyte material CsH_2PO_4 was prepared by precipitation from an aqueous solution of Cs_2CO_3 and H_3PO_4, and the synthesis confirmed by X-ray powder diffraction. The material was redissolved into water or a methanol-water mixture at a concentration of 10 - 20 g L^{-1} to serve as the electrospray solution. The methanol-to-water molar ratio was varied from 0:1 to 1:1 as a means of manipulating the solution conductivity and surface tension, parameters which can both influence the outcome of the electrospray process. [86] In selected experiments various forms of Pt and carbon were added to the solution as a means of attaining their incorporation into the final electrode structure. These were platinum black (Alfa Aesar, Stk # 43838, nom. $\sim$30 m^2/g); 40 % platinum on carbon black (Alfa Aesar, Stk # 42204); and multi-walled carbon nanotubes (MWCNTs). (The MWCNTs were synthesized by the arc discharge method and were provided courtesy of Prof. C.P. Collier) The solids loadings in the solutions were 5 g L^{-1} for the platinum black and platinum on carbon, and $<$ 1 mg L^{-1} for the MWCNTs. To promote the suspension of these insoluble additives, the common stabilizing polymer polyvinylpyrrolidone (PVP; Alfa Aesar, MW 8000) [89], was added at a concentration of 20 g L^{-1}. Deposition was performed, in most cases, on carbon paper (Toray TGP-H-120), a substrate that is suitable for subsequent fuel cell fabrication because of its high porosity, good chemical stability, and high electronic conductivity. In selected experiments, dense CsH_2PO_4 served as the substrate, however, unless stated otherwise, all results refer to deposition on carbon paper.

4.3.2 Electrospray deposition

The electrospray apparatus used for these experiments is shown in Figure 4.1 .

The solution enters the deposition chamber (at a controlled flow rate between 5 and 15 μL min^{-1}) via a stainless steel capillary (ID 127 μm, OD 1.6 mm, L 50

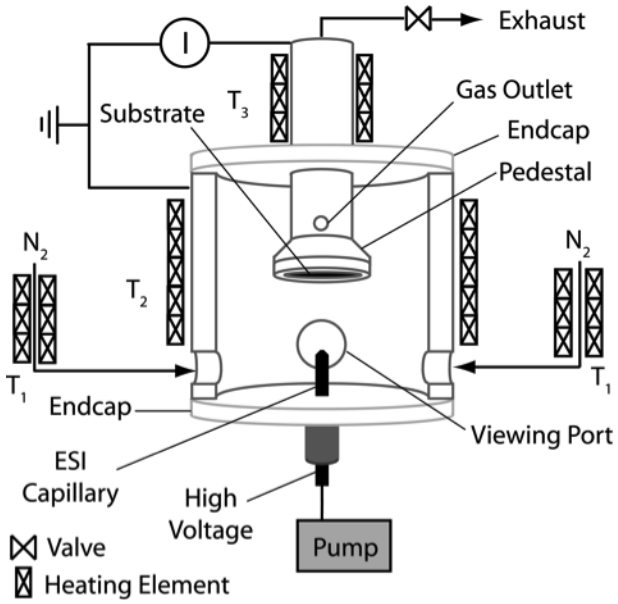

Figure 4.1: Schematic of electrospray apparatus

mm). The capillary tip is machined to a point with a half-angle of $\sim 45°$, less than the Taylor cone half-angle of 49.3°. The sharpened end of the capillary opposes a heated aluminum pedestal (OD 25.4 mm), placed typically at a distance of 3 cm, onto which the substrate is mounted. An upwards spray geometry is employed so as to prevent dripping of excess solution that can result from instabilities in the spraying process onto the substrate. Between the capillary and the pedestal a positive bias in the 4.5 to 7.5 kV range is applied, the precise value of which is selected in order to maintain a stable Taylor cone. These parts are enclosed in an aluminum housing with two plastic endcaps made of Delrin® (polyoxymethylene) that electrically isolate the capillary and the pedestal (the endcaps limit the upper operating temperature of the system to the plastic melting point of 175°C). The housing is heated independently of the pedestal. Visualization of the Taylor cone was achieved with two glass windows (dia. $\sim$ 12 mm) placed on opposite sides of the housing. The light from one window provided sufficient contrast to observe the Taylor cone directly through the second window. Two inlet and one outlet ports in the housing accommodate flowing nitrogen, used as the drying gas. The gas is preheated to enhance the rate of solvent evaporation and was supplied at a flow rate of typically 1000 sccm (gas space velocity of 1.8 cm

s^{-1}), as controlled with a mass flow controller. The current carried by the flux of charged particles to the substrate was measured using a picoammeter (Keithley 480 Digital 3.5 Digit Bench Picoammeter) connected in series between the ground wire and the pedestal, providing a convenient way to monitor the spraying process and the stability of the Taylor cone. For the structures that included co-sprayed Pt-black, the Pt loading was estimated from the weight change of the sample. Because of geometric variability between different capillary tips, which have a nominal inner diameter of only 127 μm, fine control of the Pt deposition quantity by fixing the deposition time was not possible.

4.3.3 Physical and electrochemical characterization

Phase identification of the deposited material was performed by X-ray powder diffraction, using a Philips PW3040-Pro diffractometer (CuKα radiation, 2θ range of 20° to 60°). The as-prepared electrode morphology was studied by scanning electron microscopy using a ZEISS 1550VP Field Emission SEM. For those experiments in which electrocatalysts were co-sprayed with the electrolyte for ultimate electrochemical characterization, the resulting structure was treated with an oxygen plasma with the objective of removing the PVP and ensuring that the sites for electrocatalysis would not be blocked by the polymer. An in-house constructed tubular plasma reactor was employed for this purpose [90]. The plasma was generated by inductively coupling radio frequency (13.56 MHz) power to an argon-oxygen gas mixture (Ar flow: 7.5 sccm, O_2 flow: 2.5 sccm) with a copper coil wound around a horizontal glass chamber. The electrosprayed carbon paper substrate was placed on a pedestal 10 cm downstream of the excitation region and treated for 4 min using a plasma power of 150 W with a chamber pressure of 136 mTorr. The structures were examined by infrared spectroscopy (Nicolet 860 Magna series FTIR) before and after exposure to establish the efficacy of the oxygen plasma treatment. Symmetric electrochemical cells were fabricated using dense CsH_2PO_4 electrolyte and two identical, electrosprayed carbon paper substrates as the electrodes. The electrolyte was obtained by cold-pressing

CsH_2PO_4 powder for 20 min under a uniaxial pressure of 34 MPa. Two electrosprayed electrodes were then applied to either side of the dense electrolyte and held in place using a compression holder. The screws of the holder were tightened a fixed torque of 0.1 Nm using a torque wrench so as to apply, a value found to be sufficient for attaining good electrical contact across the electrolyte-electrode interface without inducing damage to the electrode microstructure. Two stainless steel porous plates were placed on either side of the symmetric cell in order to give uniform gas diffusion to the surface of the electrode as depicted in Figure 4.2.

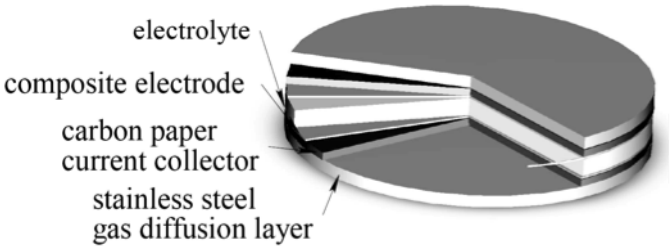

Figure 4.2: Schematic of symmetric cell assembly employed for electrochemical characterization of the electrodes; composite electrodes were electrosprayed onto carbon paper substrates

Impedance data were collected under humidified hydrogen at 240°C with an impedance analyzer (Eco Chemie Autolab PGSTAT302 equipped with a frequency response analysis module) operating at a voltage amplitude of 10 mV over frequencies ranging from 10 mHz to 1 MHz. Hydrogen was supplied at a rate of 30 sccm (0.6 cm min^{-1}) and humidified flowing through a water bubbler held at 80°C.

4.4 Results and Discussion

After an extensive exploration of the wide parameter space available for manipulating the outcome of the electrospray process, a highly fractal and porous structure with submicron features was ultimately obtained, an example of which is shown in Figure 4.3 (a) and (b)

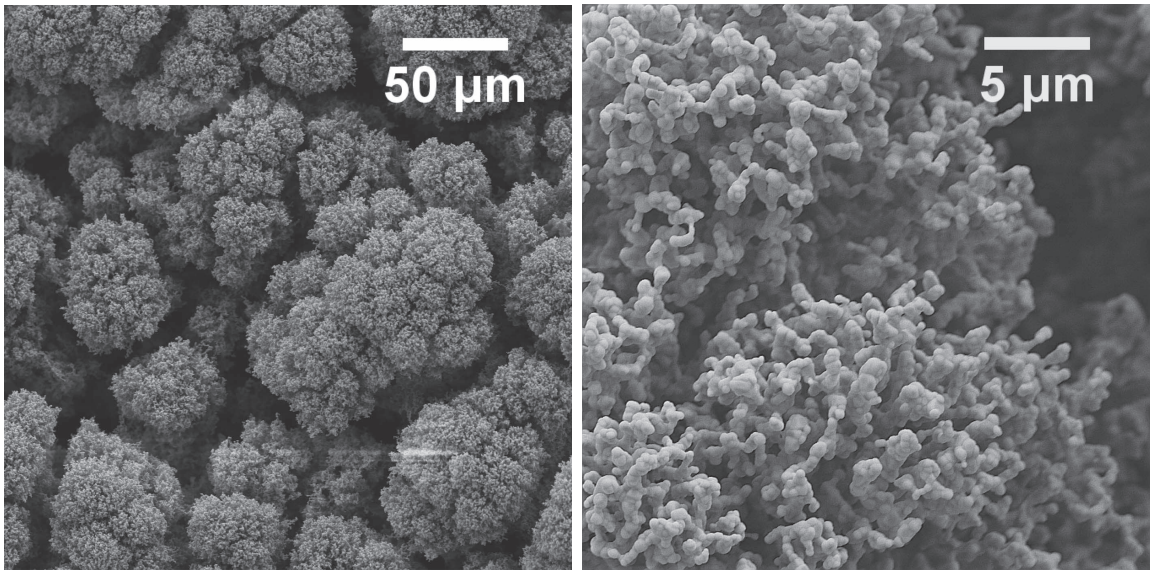

Figure 4.3: (a) low magnification and (b) high magnification SEM micrograph of porous, interconnected, three-dimensional CsH_2PO_4 structure obtained by electrospray deposition (parameters given in Table 5.1) showing fractal conformation

The parameters leading to this structure are summarized in Table 4.1. The average feature size, as directly determined from the SEM micrograph, was found to be ca. 300 nm. The X-ray diffraction pattern of the nanostructure (4.4) confirmed that the deposited material was CsH_2PO_4.

A deposition rate of 5 mg h^{-1} and deposition efficiency (defined as the ratio of mass gain of the substrate to solute mass loss) of 50-70 % were measured by weighing the sample and solution before and after deposition with a precision balance. The sample surface coverage was complete but non-uniform. The thickness of the porous film ranged from 20 μm at the center of the substrate to 10 μm at the edge. It is

Table 4.1: Electrospray parameters employed for the preparation of porous, nanostructured CsH_2PO_4 electrodes (e.g., Figure 4.3) and solid films (e.g., Figure 4.5)

Parameter	Porous nanostructure	Thin film
Temperature (°C)	140	90
Voltage (kV)	4.5	7.5
Sheath gas flow rate (sccm)	1000	300
Mol% methanol in solution	50	0
CsH_2PO_4 concentration (g/L)	10	20
Solution flow rate (ml/h)	1	1

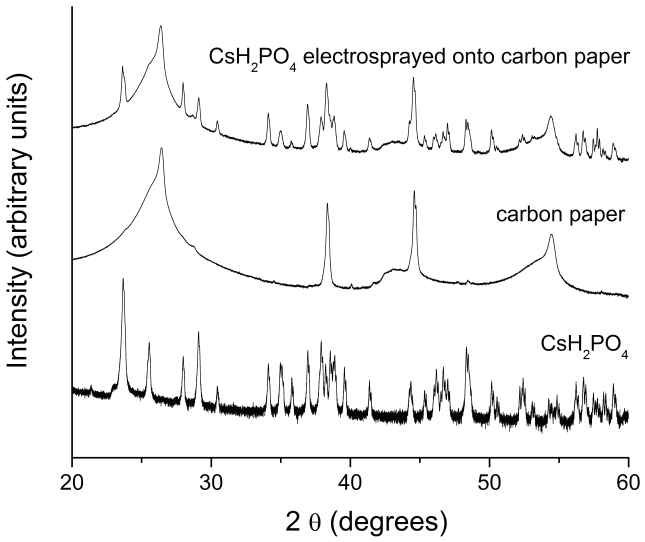

Figure 4.4: X-ray diffraction pattern of electrosprayed CsH_2PO_4 compared to those of the carbon paper substrate and neat CsH_2PO_4

thought that the non-uniform deposition ensues from the radial decrease of the electric field strength in combination with statistical variations of the charge carried by each droplet. As the dominant force acting on the charged droplets and particles is electrostatic in nature, it can be expected that their flight path follows the electric field lines and the number density of deposited particles correlates with the strength of the electric field.

Varying the substrate temperature over the range from 65 to 140°C, while holding all other parameters constant (with the exception of voltage), produced no significant change in the morphology of the nanostructure. This result provides strong evidence that the solvent completely evaporates before CsH_2PO_4 particles are deposited. Otherwise, differing amounts of residual solvent would generate differing morphologies. The absence of solvent at the final point of particle-substrate impact, in turn, suggests that the fractal nanostructure is created as a result of preferential deposition of particles onto protrusions created by growth instabilities and magnified by electric field effects in combination with limited surface diffusion. The alternative possibil-

ity, of void generation due to vigorous evaporation of the solvent upon contact of droplets with the substrate, is inconsistent with the temperature independent morphology. Overall, the preliminary evidence suggests that ensuring complete solvent evaporation is essential for obtaining fractal structures. Conditions with low solvent evaporation rates (i.e. reducing the nitrogen flow rate, eliminating methanol from the electrospray solution, and/or lowering the chamber temperature) led to the growth of a dense film, as shown in Figure 4.5.

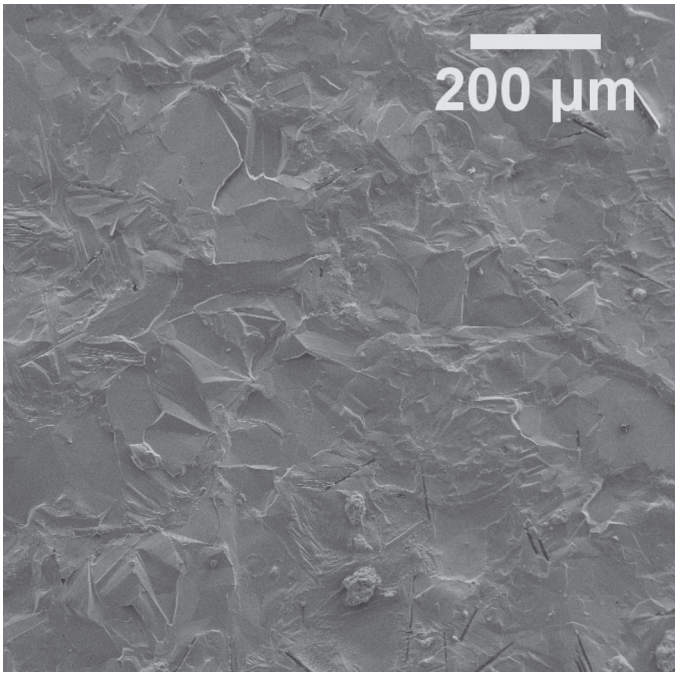

Figure 4.5: SEM image of dense thin film of CsH_2PO_4 obtained by electrospray deposition (parameters given in Table 4.1)

While not pursued in this work, the high density of this film suggests that the electrospray method can be used for both electrolyte and electrode fabrication in fuel cell construction, as has begun to be explored for solid oxide fuel cells. [91] Furthermore, exploratory depositions on CsH_2PO_4 were quite successful, opening up alternative avenues for fuel cell fabrication (not shown). Typically, electrospray deposition is not possible on electronically insulating substrates because charge accumulation eventually deflects incoming, like-charged particles. Successful deposition in this case

suggests that the high protonic conductivity of CsH_2PO_4 (even at temperatures below the phase transition) is sufficient to permit charge dissipation.

Returning to the morphological features of the material deposited on carbon, Figure 4.3, it is apparent that the fractal structure displays a highly attractive morphology for electrode application with high porosity and high surface area. However, the configuration was found to be unstable over time. Coalescence of the particles was evident after just two days of exposure to ambient conditions and, after seven days, the loss of surface area and porosity was severe, Figure 4.6

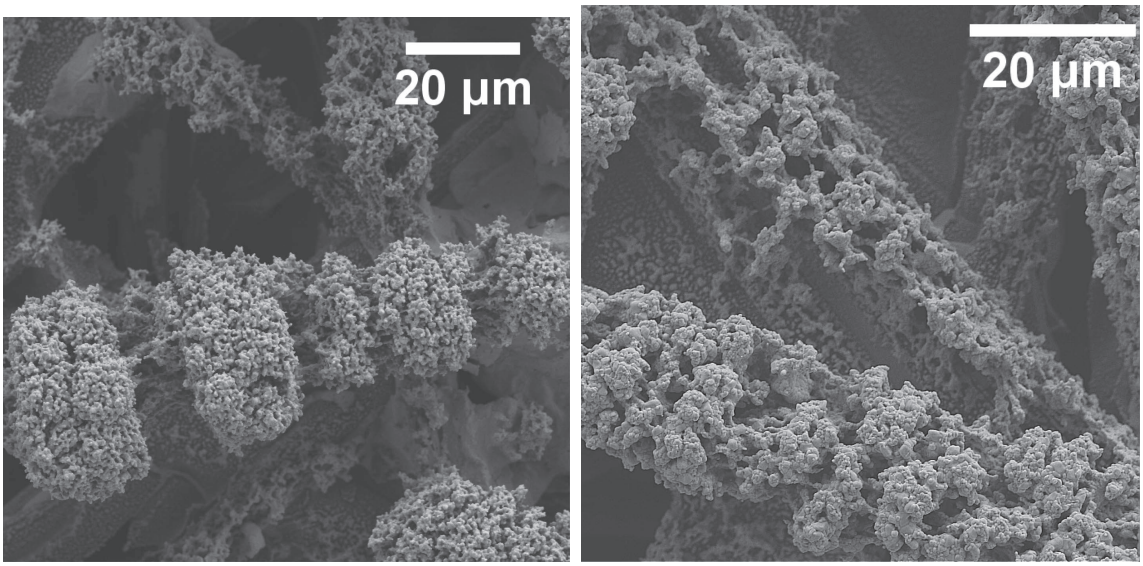

Figure 4.6: SEM micrograph showing agglomeration of CsH_2PO_4 nanostructureafter (a) two days and (b) seven days of exposure to ambient conditions

This behavior is believed to be connected to the hydrophilic nature of CsH_2PO_4 and its capacity (though the material is not seriously deliquescent) to absorb water from the atmosphere. Similar coarsening behavior has impeded progress in the incorporation of nanoparticle CsH_2PO_4 obtained by aerosol methods into advanced SAFC electrodes. [8] Furthermore, even if morphologically stabilized, the structure of Figure 4.3 requires introduction of an electronically conducting phase and electrocatalysts in order to function electrochemically. Incorporation of the electron-conducting and catalytic additives, Pt black, Pt on carbon, and MWCNTs, into the electrospray solution

(while maintaining all other parameters as in Table 4.1) led, respectively, to the structures shown in Figures 4.7 - 4.8. Two characteristics in these composite structures are distinctly different from those of the neat CsH_2PO_4 structures. First, the feature size is substantially reduced, from $\sim$ 300 nm to $\sim$ 100 nm, whether the added component is Pt black, Pt on carbon, or MWCNTs. Second, the structure is markedly smoother on a 10 μm scale, suggesting rapid discharge of the electrical current through the high conductivity additives. It is also noteworthy that the additive phase is not visible in the image, suggesting that the Pt and C are well dispersed. That the conducting phases can indeed be incorporated into the structures was confirmed by simply visual inspection: on black carbon paper neat CsH_2PO_4 forms a visibly white layer, whereas on a white substrate (dense CsH_2PO_4) the electrosprayed composite forms a visibly black, non-reflective layer.

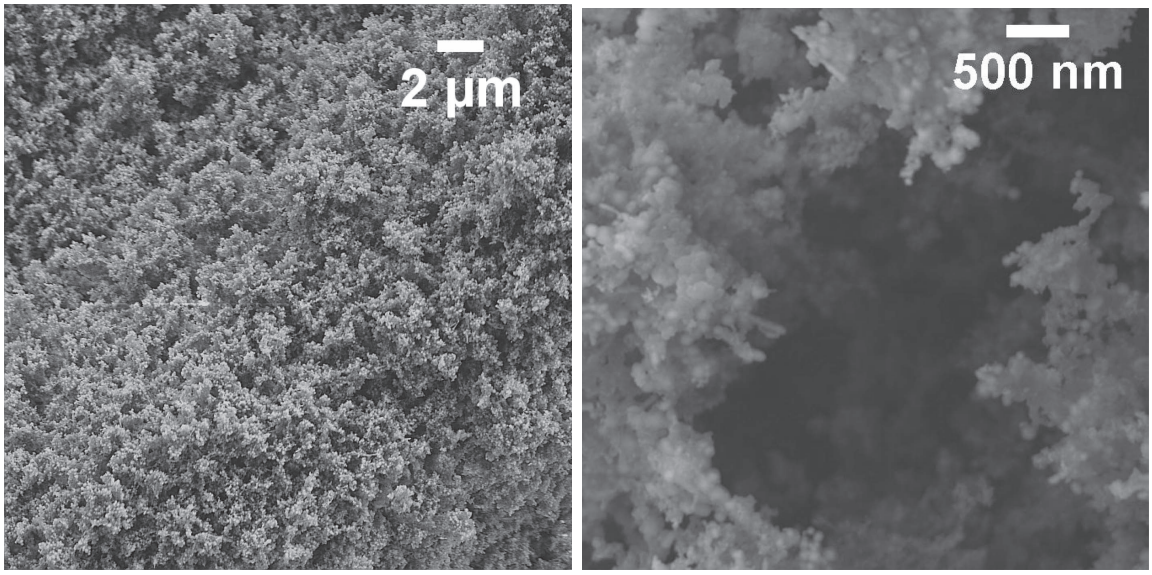

Figure 4.7: SEM micrograph of composite electrode nanostructures comprised of CsH_2PO_4, Pt-black and PVP at (a) low magnification and (b) high magnification

The FTIR spectra of composite electrodes, Figure 4.10, reveal a sharp difference between the as-deposited structures and those exposed to an oxygen plasma treatment. The as-deposited material, prepared using Pt black as the additive, displays

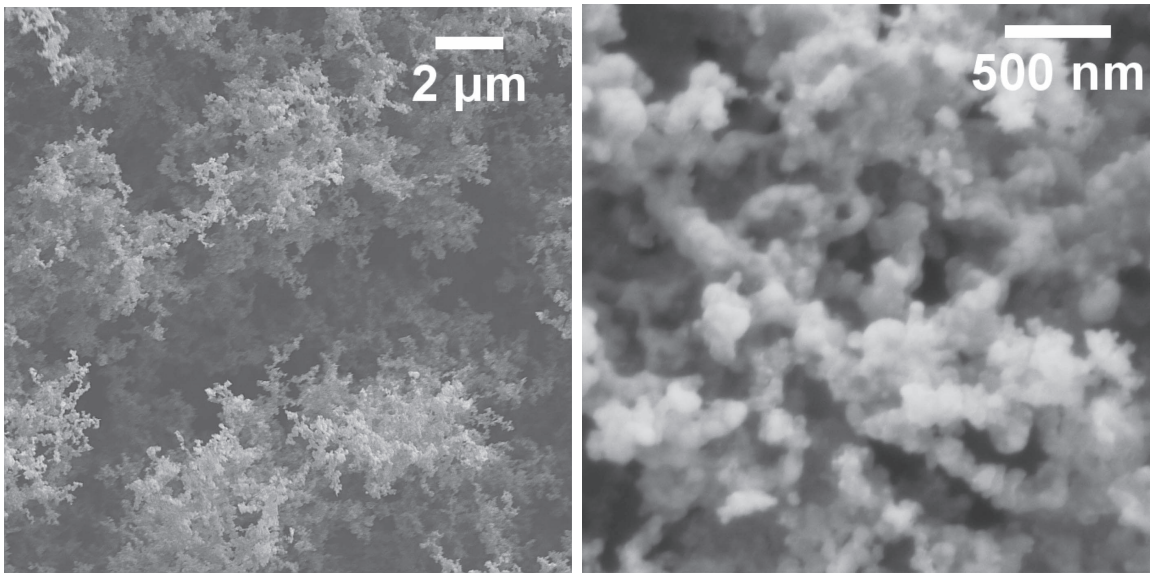

Figure 4.8: SEM micrograph of composite electrode nanostructures comprised of CsH_2PO_4, Pt on carbon, and PVP at (a) low magnification and (b) high magnification

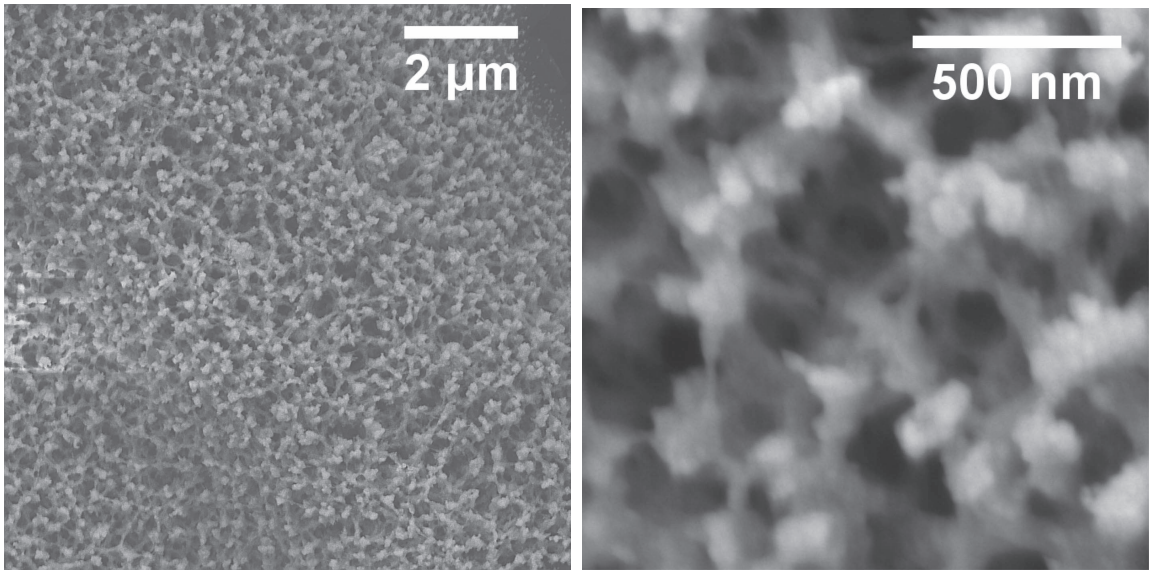

Figure 4.9: SEM micrograph of composite electrode nanostructures comprised of CsH_2PO_4, multi-walled carbon nanotubes, and PVP at (a) low magnification and (b) high magnification

several IR absorption bands in the region 1000 to 4000 cm^{-1} which correspond to either the blank carbon paper or the reference spectrum for PVP [92]. After 4 min of exposure to plasma treatment, the bands at $\sim$ 1650 and 1285 cm^{-1} due to PVP are completely removed and the spectrum is essentially identical to that of the substrate. Rather remarkably, the structure is not only morphologically unchanged by the plasma treatment, but also morphologically stable over long periods of time subsequent to the treatment. Even after several days of exposure to ambient conditions, the plasma-treated composite structure retains its 100 nm feature size, Figure 4.11. Thus, insoluble catalyst components can be readily incorporated into electrosprayed CsH_2PO_4 electrodes, with the fortuitous consequence of providing morphological stability.

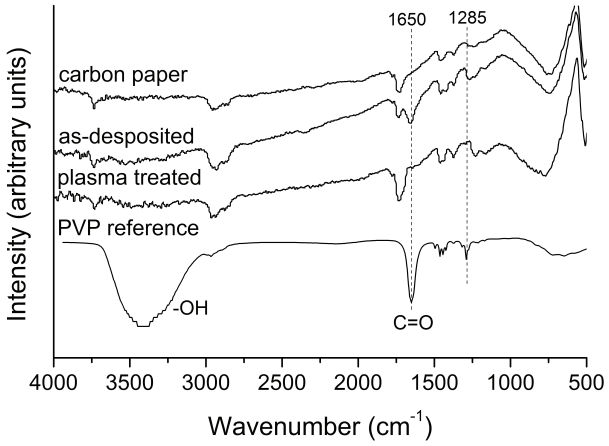

Figure 4.10: FTIR spectra of (i) blank carbon substrate, (ii) as-deposited composite electrode comprised of CsH_2PO_4, Pt, and PVP, (iii) composite electrode after oxygen plasma treatment, and (iv) reference PVP (in KBr). Large, broad spectrum band at $\sim$ 3400 cm^{-1} apparently due to residual water

Electrochemical measurements were performed using the electrosprayed electrodes incorporating Pt black and subsequently subjected to oxygen plasma treatment for PVP removal (the effectiveness of which was always confirmed by FTIR spectroscopy prior to electrical characterization). Based on the change in substrate mass upon

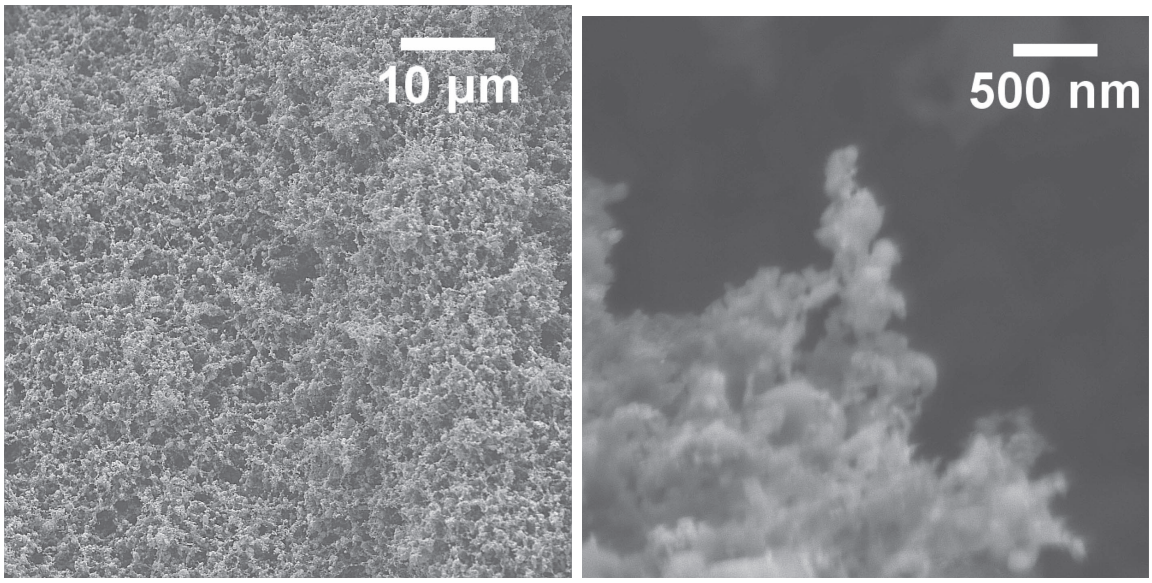

Figure 4.11: SEM micrograph of composite electrode nanostructures comprised of CsH_2PO_4, Pt-black and PVP after exposure to ambient conditions for five days subsequent to oxygen plasma treatment (a) low magnification and (b) high magnification

electrode deposition, the Pt loading (mass of Pt per unit projected area) is estimated at 0.3 ± 0.2 mg cm^{-2}. In general, the impedance spectra, as presented in Nyquist form, Figures 4.12 and 4.13, were found to display two overlapping arcs in the frequency regime of 1 MHz to 10 Hz, both attributed to the electrode behavior, as well as an offset along the real axis, corresponding to the resistance of the electrolyte. The characteristic frequencies of the observed arcs are ∼3 kHz, consistent with electrode behavior. Impedance spectra collected from three different samples, Figure 4.12, demonstrate the high reproducibility of the method. Furthermore, the electrosprayed electrodes display excellent stability, Figure 4.13. Over the course of a 24 hr measurement under humidified hydrogen at 240 °C, the electrochemical activity increased slightly in the first 12 hrs and then reached an apparently stable value. This observation suggests that coarsening of the electrode structure is minimal on the timescale of hours, whereas interfacial contacts may improve under the slight pressure of the cell holder.

Rather significantly, the total electrode impedance measured here, of ∼ 1.5 Ωcm^{-2} (determined simply from the total span of the electrode arcs along the real axis),

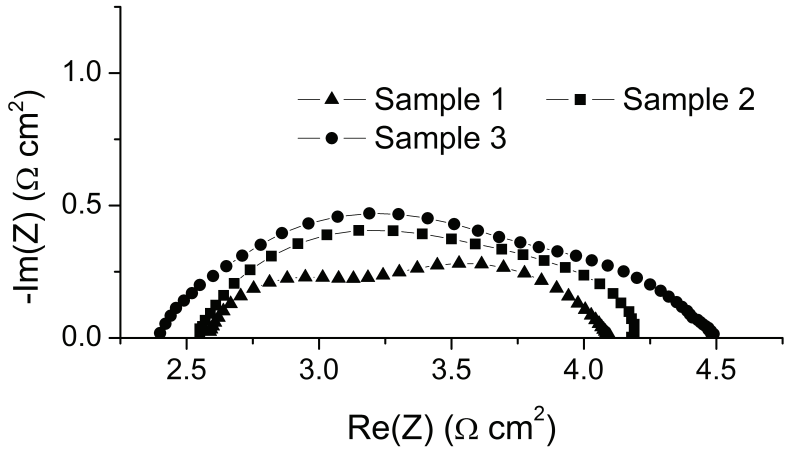

Figure 4.12: Impedance spectra of representative CsH_2PO_4 + Pt | CsH_2PO_4 | CsH_2PO_4 + Pt symmetric, electrochemical cells with electrosprayed electrodes on carbon and a Pt loading of 0.3 ± 0.2 mg cm^{-2}; data collected under humidified hydrogen with pH_2O = 0.4 atm at 240°C

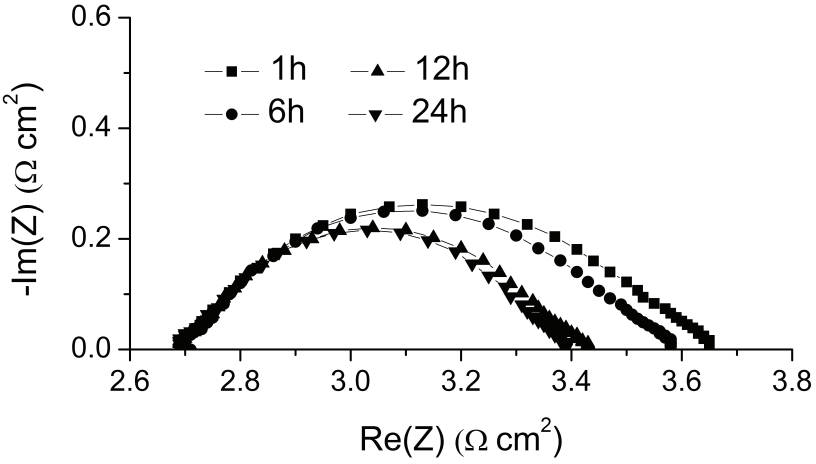

Figure 4.13: Impedance spectra of representative CsH_2PO_4 + Pt | CsH_2PO_4 | CsH_2PO_4 + Pt symmetric, electrochemical cells with electrosprayed electrodes on carbon and a Pt loading of 0.3 ± 0.2 mg cm^{-2}; data collected under humidified hydrogen with pH_2O = 0.4 atm at 240°C collected over a 24 hour period

is comparable to that obtained previously (1.67 Ωcm^{-2}) using mechanically milled electrodes of almost identical overall composition (approximately 2:1 by mass of CsH_2PO_4:Pt), but with much higher total mass and hence much higher Pt loading ($\sim$ 10 mg cm^{-2}) [17]. The 30-fold reduction in Pt loading without loss in activity is a highly attractive outcome of the electrospray process. Unlike the electrodes fabricated here, however, state-of-the-art SAFC electrodes incorporate Pt on carbon (Pt/C) and graphite in addition to Pt black and display interfacial impedance values of only $\sim$ 0.06 Ωcm^{-2} under humidified hydrogen (with a Pt loading of 7.7 mg/cm^2). [6] Efforts are presently under way to produce comparable multi-component SAFC electrodes by the electrospray process and achieve an analogous 30-fold reduction in Pt loading without loss in activity. Such an outcome would render the anode performance of SAFCs comparable to state-of-the-art polymer electrolyte membrane fuel cells and set the stage for addressing the even more challenging problems of cathode electrochemical activity, stability and Pt loading. [8] Finally, it is noteworthy that composite electrodes from which PVP had not been removed by an oxygen plasma treatment displayed electrochemical impedances that were only slightly higher (by about a factor of two) than those for which PVP removal had been confirmed by IR spectroscopy. This result suggests that the spraying process leaves regions of the Pt particles uncoated by the stabilizing polymer, or that PVP is sufficiently permeable that the catalyst particles remain accessible for electrochemical reactions. The alternative possibility, that the polymer removal under the oxygen plasma treatment is incomplete, is considered less likely; FTIR spectra of the redissolved electrodes did not show any sign of the presence of organic components.

4.5 Conclusion

The viability of electrospray deposition as a solid acid fuel cell electrode fabrication tool has been demonstrated. A three-dimensional, porous, interconnected CsH_2PO_4 and Pt nanostructure has been created with an average feature size of 100 nm. The structure is morphologically stable under oxygen plasma treatment applied to remove the stabilizing polymer PVP, and upon exposure to high humidity at elevated temperatures. Such electrosprayed electrodes have an interfacial impedance of 1.5 Ωcm^{-2} for hydrogen electro-oxidation with a platinum loading of 0.3 mg cm^{-2}. In comparison to mechanically milled electrodes of Pt black and CsH_2PO_4 with similar composition, the electrochemical activity is maintained despite an approximately 30-fold reduction in Pt loading. While this result indicates that electrospray deposition can dramatically increase Pt utilization in SAFC electrodes relative to cruder fabrication methods, the specific combination of activity and Pt loading reported here is not sufficient for widespread adoption of solid acid fuel cells. However, several avenues for optimization of the resulting electrodes and their electrochemical activity are available (compositional tuning, introduction of carbon, further reducing feature size) and may ultimately enable high activity electrodes with sufficiently low precious metals content.

4.6 Acknowledgements

Funding for this project was provided by the Gordon and Betty Moore Foundation through the Caltech Center for Sustainable Energy Research, and by the Airforce Research Office, through a the subaward from Superprotonic, Inc. Additional support was provided by the National Science Foundation through the Caltech Center for the Science and Engineering of Materials, a Materials Research Science and Engineering Center (DMR-052056). The authors thank Dr. Chi Ma and Prof. George Rossman for assistance, respectively, with scanning electron microscopy and infrared spectroscopy.

Chapter 5

Platinum thin films on electrosprayed CsH_2PO_4 structures

5.1 Abstract

Solid acid fuel cells are performance limited by the electrode reaction kinetics. Platinum loadings of up to 7.7 mg cm^{-1}) are necessary to sufficiently catalyze the electrochemical reactions at the electrodes. Continuing efforts target improved catalyst utilization in order to minimize precious metal loadings without sacrificing power density. Platinum utilization of 2.2 S mg^{-1} has been reported for high performance electrodes. 19 S mg^{-1} has been reported for two-dimensional platinum thin film electrodes in humidified hydrogen, with controlled geometries but with large area specific electrode resistance due to small absolute area. Here we seek to extend the two-dimensional thin film interface into the third dimension, and therefore maximize the electrocatalytically active area, by creating a highly porous CsH_2PO_4 electrolyte nanostructure via electrospray deposition and adding a platinum thin film via magnetron sputtering or metal-organic chemical vapor deposition. The amount of electrolyte nanostructure was varied between 0.2 and 5 mg and the thickness of platinum thin film between 5 and 30 nm with sputter deposition. 10, 20 and 50 nm platinum layer was deposited with metal-organic chemical vapor deposition onto 5 mg of electrosprayed electrolyte nanostructure. The platinum mass normalized activity for the best electrode obtained with MOCVD creating a 50 nm platinum layer was 6.35 S mg^{-1}. Remarkable mass

normalized activity values of $\sim$500 S mg^{-1} were recorded for three separate samples obtained by sputter deposition of a 15 nm platinum film and electrospraying a 0.4 mg of electrolyte nanostructure.

5.2 Introduction

The largest overpotential in a solid acid fuel cells can be attributed to the oxygen reduction reaction at the cathode, i.e. the performance limiting component. [6] To increase reaction kinetics, an empirically optimized amount of platinum and platinum on carbon catalyst (7.7 mg of Pt cm^{-2}) is used, rendering the technology non-viable for commercial application. [4]

With the assumption that both hydrogen electro-oxidation and oxygen electro-reduction reactions are limited by same electrode characteristics, an improvement in one electrode entails an improvement of the same magnitude in the other electrode. In this chapter, for experimental convenience, we consider electrochemical measurements in symmetric humidified hydrogen environment and symmetric cell geometry, rather than in humidified oxygen environment.

Mass normalized activity of a catalyst is a convenient metric to compare and contrast the performance and utilization of catalyst materials. It is measured as current per unit mass of catalyst material and is dependent on the intrinsic activity of the catalyst and its utilization. To date, the highest platinum catalyst mass-normalized activity of a solid acid fuel cell electrode in humidified hydrogen, mechanically milled and cold-pressed powder electrodes is 2.2 S mg^{-1} [6] The area specific resistance, calculated as the resistivity times the projected electrode area, was 0.06 Ω cm^2. In such an electrode, the reaction rate is limited by the density of electrocatalytically active triple phase boundaries, between the electrolyte, the catalyst and the gas phase. Recent work on simple, two-dimensional electrodes consisting of platinum thin films with controlled geometries (thickness and area) has shown that up to 19 S mg^{-1} mass normalized activity can be achieved. [14] In this case, 7.5 nm thin platinum film was sputtered onto cold-pressed and carefully polished CsH_2PO_4 electrolyte pellets (19 mm diameter). Here, hydrogen diffusion through the platinum thin film is sufficiently fast, so that the entire two-phase boundary between the electrolyte and the platinum film is catalytically active in addition to the triple phase boundary at the edge of the platinum thin film. The area specific resistance was 3.1 ± 0.5 Ω cm^2. The

large value is not surprising despite the excellent catalyst mass normalized activity, based on the small absolute electrode area.

An increase of the two-phase boundary interface into the third dimension by depositing the platinum catalyst thin film onto a high surface area, porous electrolyte nanostructure is shown here to improve the electrode kinetics dramatically.

5.3 Experimental procedure

5.3.1 Materials and symmetric cell fabrication

CsH_2PO_4 powder was synthesized using the co-precipitation method [15]. In brief, stoichiometric quantities of phosphoric acid and cesium carbonate were mixed and allowed to react in an aqueous solution while heating to ∼50°C and stirring for 15 min. CsH_2PO_4 is then precipitated out in a methanol bath, filtered and dried overnight at 100°C. Phase purity was confirmed with powder X-ray diffraction.

Solid pellets of electrolyte (19 mm diameter, 0.5 mm thickness) were fabricated by uniaxially cold pressing the dry CsH_2PO_4 powder for 20 min at 34 MPa.

To fabricate the high surface electrode, an aqueous solution of CsH_2PO_4 and the surfactant polyvinylpyrrolidone (PVP M_W 8000 u, Alfa Aesar, Stk no. 41626) was electrosprayed onto both sides of the electrolyte pellets in the manner described by Varga et al. [33]. The solution consisted of a water-methanol mixture (1:1 molar ratio) with CsH_2PO_4 and PVP concentrations of 10 and 20 g/L respectively, Table 5.1.

Table 5.1: Electrospray parameters employed for the preparation of porous, nanostructured CsH_2PO_4 directly deposited onto cold pressed pellet of CsH_2PO_4

Parameter	Porous CsH_2PO_4 nanostructure
Temperature (°C)	100
Voltage (kV)	4.5
Sheath gas flow rate (sccm)	1000
Mol% methanol in solution	50
CsH_2PO_4/PVP concentration (g/L)	10/20
Solution flow rate (ml/h)	1

5.3.1.1 Platinum thin film deposition via sputtering

Subsequent to electrospray deposition of CsH_2PO_4, platinum thin films were deposited at room temperature onto the both sides of the electrolyte pellet *via* DC magnetron sputtering using a Cressington 208HR system (∼15 mTorr Ar, 80 mA plasma current). For uniform film deposition, the samples were rotated in an orbital fashion, around two separate axes. Sputter deposition is a very poor line of sight deposition method [93]. This is exploited here in order to cover those features of the electrosprayed nanostructure that are not on the top surface, with a platinum thin film. Nevertheless, a non-uniform film thickness with a high density of edges is expected due to shadowing effects of the irregular porous electrolyte nanostructure.

The electrospray deposition time was varied between 1 min and 30 min, resulting in a variation of 0.2 to 5 mg deposited material. The thickness of the sputter deposited platinum thin film was measured with a thickness monitor using the frequency shift of an oscillating crystal, and controlled between 5 and 30 nm, Table 5.2.

5.3.1.2 Platinum thin film deposition via metal-organic chemical vapor deposition

An in-house CVD reactor, consisting of a vacuum oven (National Appliance Company 5831), a vacuum pump (Buechi V-500) and nitrogen purge lines was constructed. A procedure to deposit a platinum thin films on CsH_2PO_4 particle surfaces has been described by Papandrew et. al [94]. Preferential decomposition of the organometallic platinum precursor and deposition of platinum on CsH_2PO_4 was observed in their study. Here we use a similar procedure to deposit platinum thin films onto electrosprayed CsH_2PO_4 nanostrutures. In brief, platinum(II)(2,4)-pentanedionate ($Pt(acac)_2$, Alfa Aesar, Pt 48% min, Product No. 10526) powder is added onto porous carbon paper filter (Toray, TGP-H-60) and placed onto both sides of the coldpressed electrolyte pellet, Figure 5.1. The filter was removed together with the remaining platinum powder after the deposition process. The amount of $Pt(acac)_2$ powder was

varied: 40, 80 and 160 mg were used per electrode. The substrate and platinum precursor were then covered with a Petri dish. A small vial with 2.1 ml deionized water is placed into the chamber of the vacuum oven. The oven is evacuated with a diaphragm membrane pump to 0.3 bar and purged with dry nitrogen three times. After the final evacuation, the sealed vacuum chamber was heated to 145°C and kept for 12 hours to allow decomposition of the metal-organic precursor and platinum deposition, Figure 5.2. Three different electrodes with varying amounts of $Pt(acac)_2$ precursor powder have been fabricated. The platinum loading was determined by weighing each symmetric cell before and after MOCVD. Excess platinum particles were removed together with the carbon paper porous layers and weighed to ensure that the $Pt(acac)_2$ precursor decomposed completely.

Figure 5.1: (a) $Pt(acac)_2$ powder on porous carbon paper, (b) as pressed CsH_2PO_4 pellet, (c) $Pt(acac)_2$ powder|carbon paper|electrosprayed CsH_2PO_4|CsH_2PO_4 pellet|electrosprayed CsH_2PO_4|carbon paper|$Pt(acac)_2$ powder in a Petri dish.

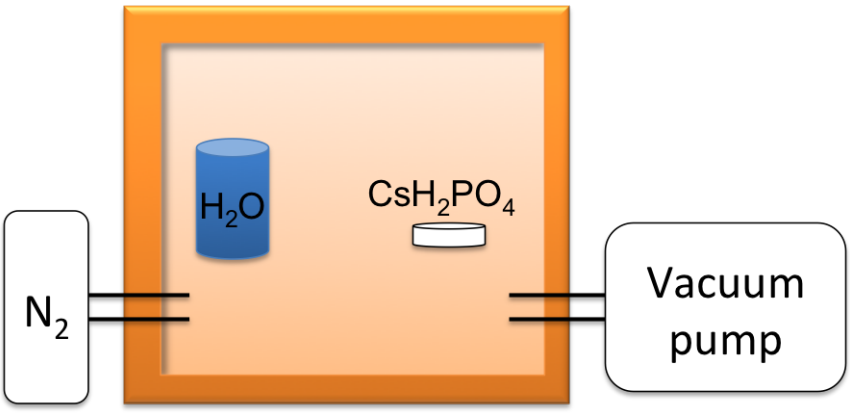

Figure 5.2: Schematic of metalorganix chemical vapor deposition setup

Table 5.2: Variation of deposition amount of porous electrolyte nanostructure and platinum thin film

	ESD time (min)	Sputtered Pt film (nm)	MOCVD Pt film (nm)
Sample 1	5	45	
Sample 2	2	45	
Sample 3	1	45	
Sample 4	30	30	10/20/50
Sample 5	5	30	
Sample 6	2	30	
Sample 7	1	30	
Sample 8	5	15	
Sample 9	2	15	
Sample 10	1	15	
Sample 11	5	5	
Sample 12	2	5	
Sample 13	0	5	

The side along the circumference of each pellet was sanded in order to remove any platinum deposited there and to prevent a short circuit between the two electrodes.

Carbon paper (Toray TGP-H-120) current collector and stainless steel porous gas diffusion layer were lightly pressed on both sides of the pellet for electrochemical measurements, Figure 5.3.

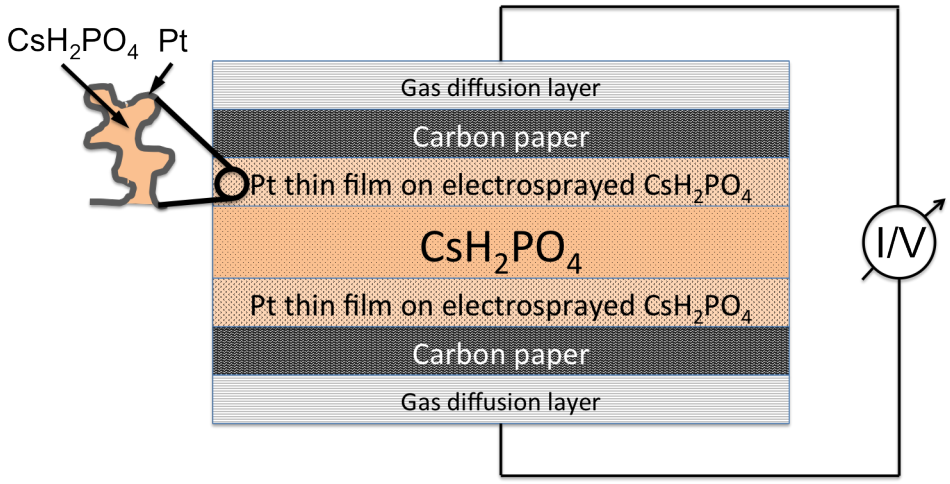

Figure 5.3: Schematic symmetric cell configuration

5.3.2 Physical and electrochemical characterization

The electrode microstructures were imaged *via* scanning electron microscopy (Zeiss 1550VP Field Emission SEM, 3 - 10 kV accelerating voltage) before and after electrochemical measurements. A Solartron Analytical 1260 frequency response analyzer was used for the electrochemical measurements, applying a sinusoidal voltage perturbation ranging from 10 mHz to 1 MHz and a voltage amplitude of 10 mV. Hydrogen was supplied at a linear flow velocity of 0.6 cm min^{-1} (30 sccm) and humidified by flowing through a water bubbler kept at 80°C. The equilibrium water partial pressure was calculated to be $pH_2O = 0.4$ atm. The cell temperature was maintained at 240°C during the measurement.

5.4 Results and discussion

5.4.1 Sputtered platinum on high surface area electrolyte nanostructures

Figure 5.4 shows a digital photograph of a representative CsH_2PO_4 pellet (a) before and (b) after electrospray deposition of the porous electrolyte nanostructure and sputter deposition of the platinum thin film. The as pressed CsH_2PO_4 pellet appears uniform white, whereas the as-deposited pellet has two shades of grey. The darker color indicates a porous surface, i.e. the presence of the porous nanostructure obtained by electrospray deposition, while the lighter grey indicates a smooth surface, the area covered by the sample holder during the electrospray deposition. The density of the pellet was measured to be 94 ± 2 %.

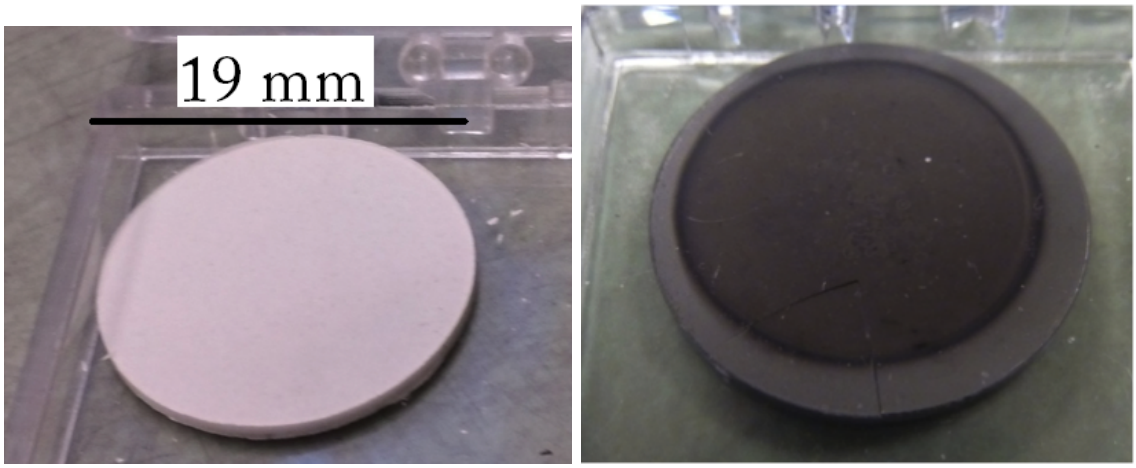

Figure 5.4: (a) As pressed CsH_2PO_4 pellet (b) CsH_2PO_4 pellet after electrospray, and sputter deposition of a porous electrode

Figure 5.5 shows SEM micrographs of the top surface of a representative cold-pressed CsH_2PO_4 pellets at three different magnifications. Pore and feature sizes ranging from 1 to 3 μm are visible.

Figure 5.6 shows SEM micrographs at (a) low and (b) high magnification of the top surface of a representative cold-pressed CsH_2PO_4 pellet after electrospray deposi-

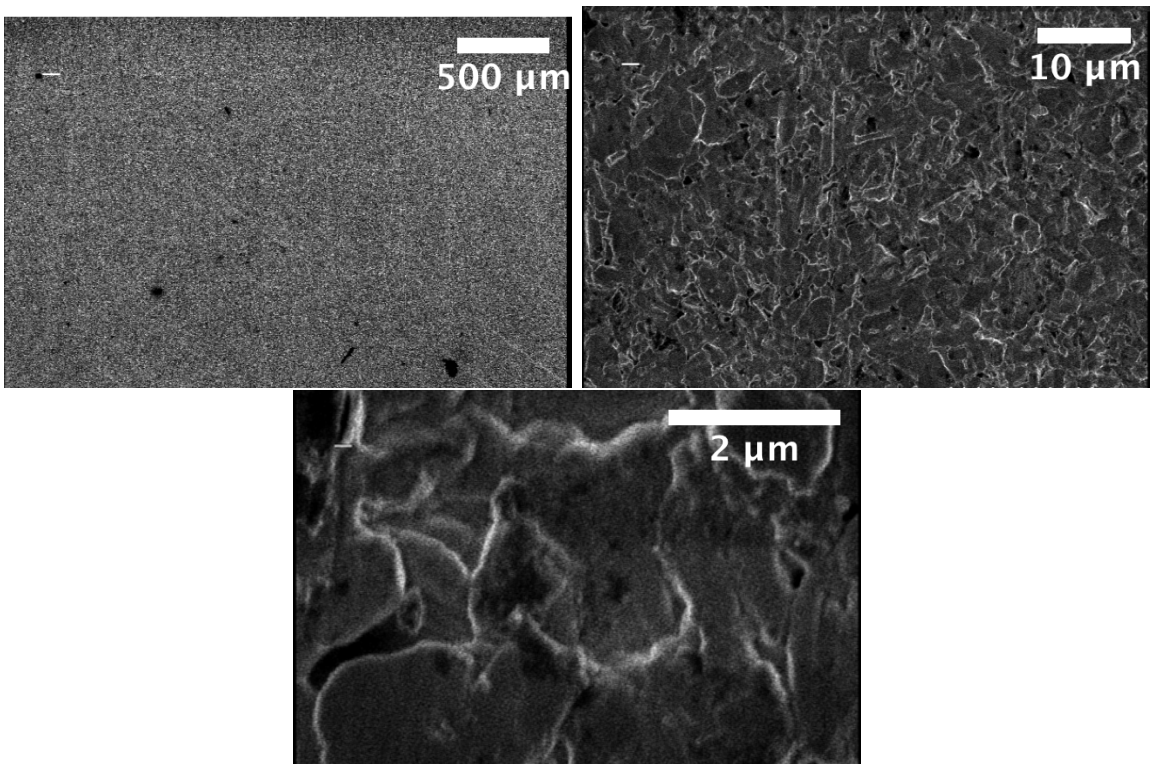

Figure 5.5: (a) Low magnification (b) intermediate magnification and (c) high magnification SEM micrograph of as pressed CsH_2PO_4 pellet surface

tion of a porous, interconnected nanostructure, consisting of CsH_2PO_4 and PVP, and subsequent sputter deposition of a 15 nm thin platinum film. 100 - 200 nm features, with 500 nm agglomerates and up to 500 nm pores are visible. As observed previously [33], the addition of the surfactant PVP serves to stabilize the nanostructure. Note that high electron beam accelerating voltage in the scanning electron microscope (>3 kV) causes severe charging and partial melting of as deposited CsH_2PO_4 nanostructures (not shown here) due to its low electronic conductivity. However, with the platinum thin film deposited, up to 10 kV electron accelerating voltage can be used due to efficient charge dissipation.

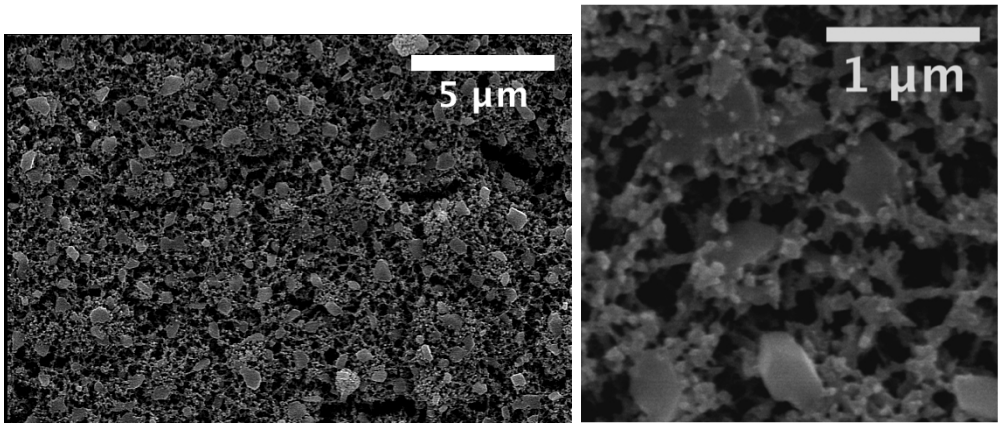

Figure 5.6: (a) Low magnification and (b) high magnification SEM micrograph of cold-pressed CsH_2PO_4 pellet surface with electrospray deposited CsH_2PO_4 + PVP and sputter deposited platinum thin film

Electrochemical measurements up to 8 hours at 240°C in a humidified hydrogen environment cause microcracks in the electrolyte pellet and some agglomeration in the electrode microstructure, especially at the contact points with the carbon fibers of the carbon paper current collector, Figure 5.7 (a) and (b) respectively. Nevertheless, a significant portion of the finer 100 - 200 nm features is still intact, providing a high surface area for the electrochemical reaction, Figure 5.8

AC impedance spectra for the symmetric cells are shown in the Nyquist form (-Im(Z) vs. Re(Z)). For convenience, the electrolyte contribution to the impedance, typically apparent as a real offset of the electrode impedance arc from the origin was

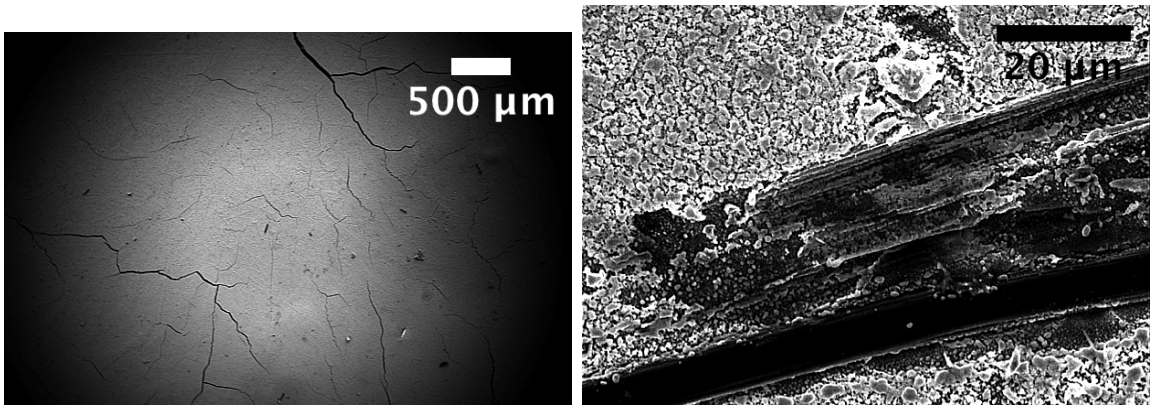

Figure 5.7: SEM micrograph of cold-pressed CsH_2PO_4 pellet surface with electrospray deposited CsH_2PO_4 + PVP and sputter deposited platinum thin film after electrochemical measurements showing (a) microcracks and (b) structure agglomeration due to mechanical pressure from the carbon paper fiber

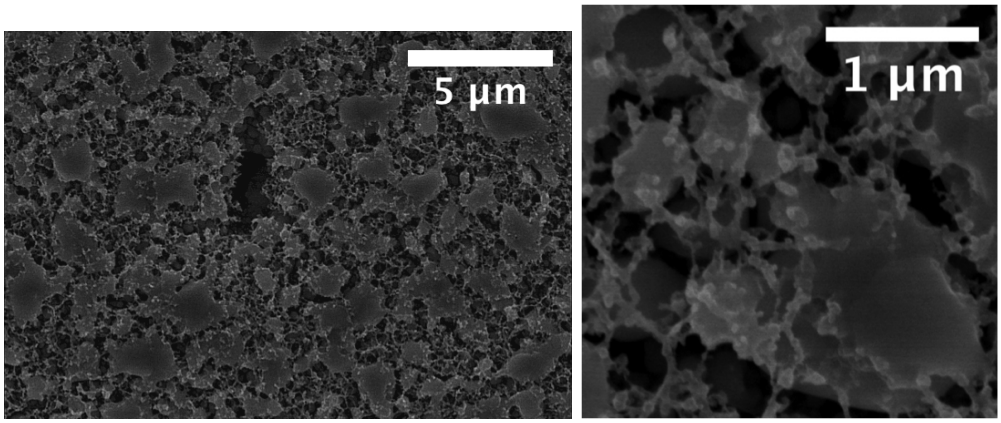

Figure 5.8: (a) Low magnification and (b) high magnification SEM micrograph of cold-pressed CsH_2PO_4 pellet surface with electrospray deposited CsH_2PO_4 + PVP and sputter deposited platinum thin film after electrochemical measurements

subtracted.

Figure 5.9 shows impedance spectra for electrodes with 45 nm platinum thin film deposited with high surface area electrolyte nanostructures obtained by 5, 2, and 1 min electrospraying. The electrodes with 5 min electrosprayed structure showed uniform degradation of the area specific resistance over a 9 hour period from an initially remarkable 0.12 Ωcm^2 to 0.75 Ωcm^2. The two electrodes with 2 and 1 min electrosprayed structures showed $<1\%$ degradation of the area specific resistance over a 5 and 3 hour period respectively.

Impedance spectra shown in Figure 5.10 show the area specific resistance of four electrodes with 30 nm thick sputtered platinums and 30, 5, 2, and 1 min electrospray deposited high surface area electrolyte nanostructures. Electrodes obtained with shorter electrospray deposition time (2 and 1 min) show good stability over a 5 and 11 h period respectively. The other two electrodes show remarkable initial area specific resistance but a significant degradation over an 8 hour period.

Very low area specific resistance values were observed with electrodes employing 15 nm thick sputter deposited platinum layers. Initial area specific resistance of 0.05 Ωcm^2 were obtained for both 5 min and 2 min electrospray deposited electrolyte nanostructures. The former electrode degraded and then stabilized over an 8 hour period to 0.5 Ωcm^2 whereas the latter electrode remained stable over a 5 hour period. The third electrode with only 1 min electrosprayed electrolye nanostructure had a 0.75 Ωcm^2 initial area specific resistance and showed good stability over a 3 hour period.

Three electrodes with only 5 nm sputtered platinum thickness showed good stability over a 12 hour period, but the area specific resistance values were relatively large, with 0.5 and 5.3 Ωcm^2 for 5 and 2 min electrosprayed nanostructures, respectively. A sample with a 5 nm platinum thin film sputtered directly onto the as pressed CsH_2PO_4 pellet showed remarkable area specific resistance values of 0.75 Ωcm^2 and good stability over a 24 hour period.

The general stability trend of less stable electrodes with longer electrospray deposition times can be explained by the possibility of deformation and densification

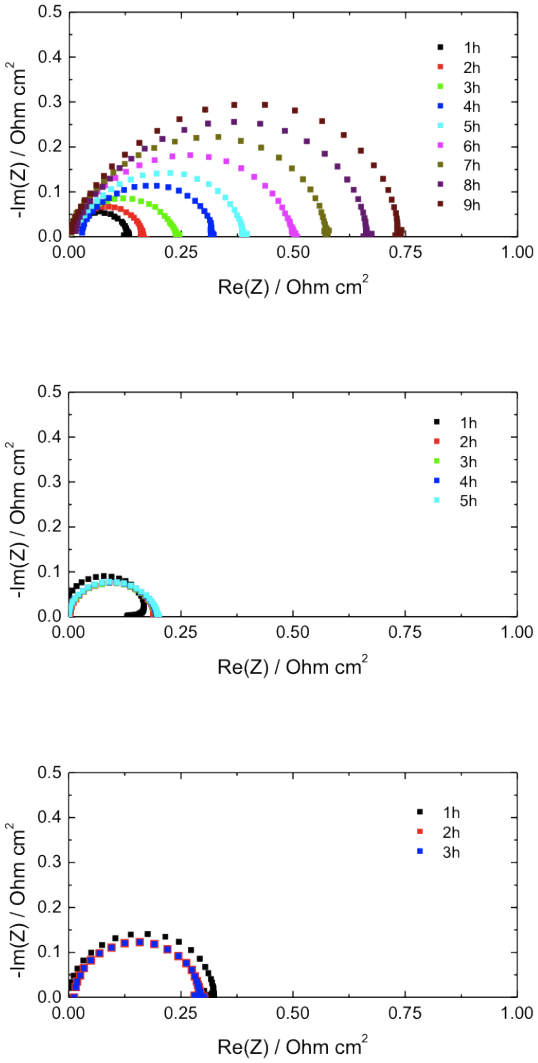

Figure 5.9: Impedance spectra of symmetric cells with electrosprayed CsH_2PO_4 + PVP + sputter deposited 45 nm Pt thin film electrodes (a) 5 min ESD, (b) 2 min ESD, (c) 1 min ESD, all measured at T=240°C, pH_2=0.6 atm, and pH_2O=0.4 atm

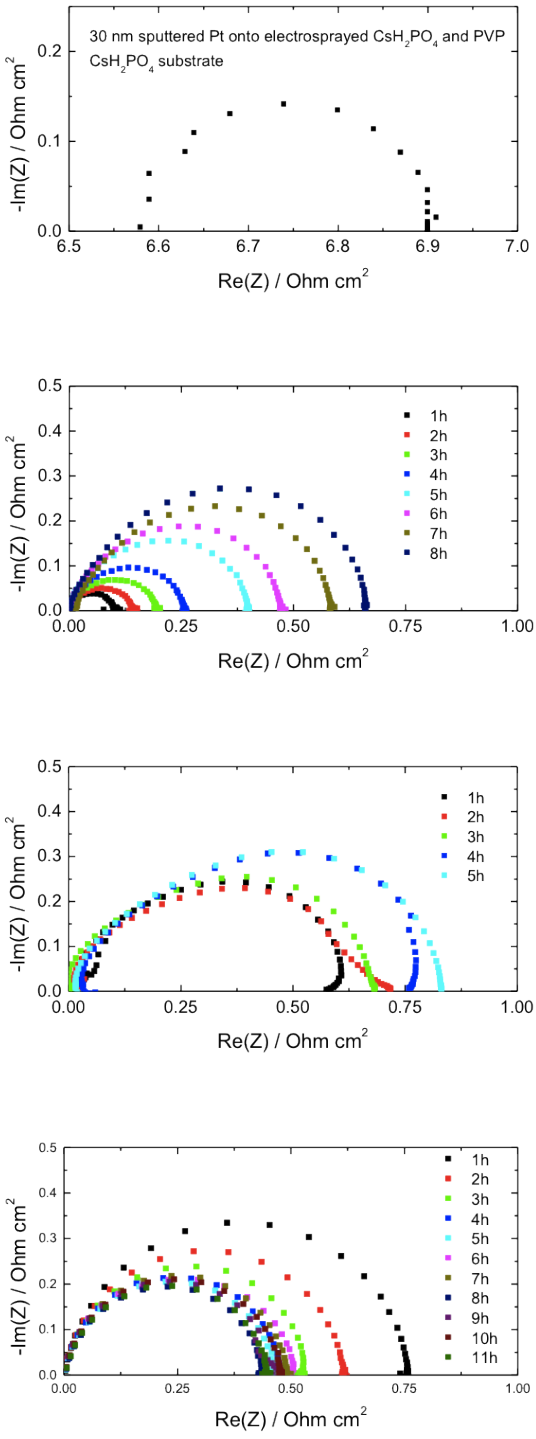

Figure 5.10: Impedance spectra of symmetric cells with electrosprayed CsH_2PO_4 + PVP + sputter deposited 30 nm Pt thin film electrodes (a) 30 min ESD, (b) 5 min ESD, (c) 2 min ESD, (d) 1 min ESD, all measured at T=240°C, pH_2=0.6 atm, and pH_2O=0.4 atm

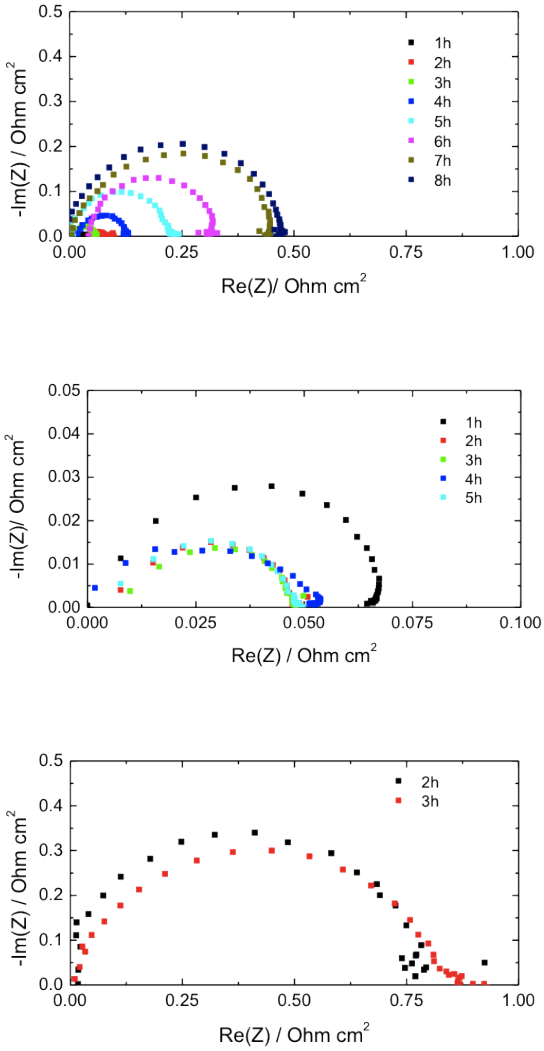

Figure 5.11: Impedance spectra of symmetric cells with electrosprayed CsH_2PO_4 + PVP + sputter deposited 15 nm Pt thin film electrodes (a) 5 min ESD, (b) 2 min ESD, (c) 1 min ESD, all measured at T=240°C, pH_2=0.6 atm, and pH_2O=0.4 atm

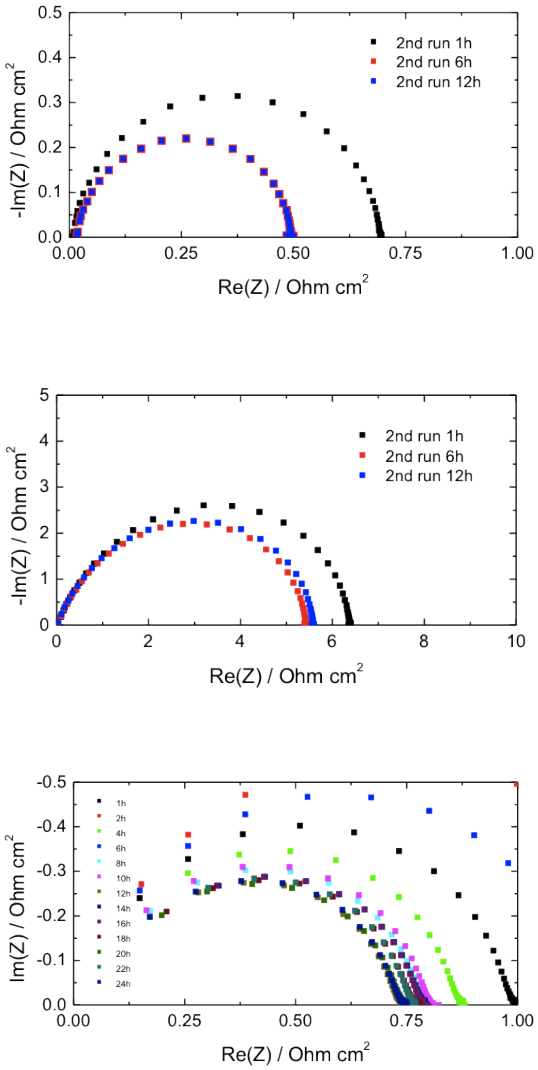

Figure 5.12: Impedance spectra of symmetric cells with electrosprayed CsH_2PO_4 + PVP + sputter deposited 5 nm Pt thin film electrodes (a) 5 min ESD, (b) 2 min ESD, (c) no ESD, all measured at T=240°C, pH_2=0.6 atm, and pH_2O=0.4 atm

of the porous electrolyte nanostructure since it becomes superplastic under fuel cell operating conditions. Electrodes with lower amounts of electrosprayed electrolyte nanostructures are less prone to deformation and hence show better initial stability.

The absolute area specific resistance values show remarkable and surprising results for the given platinum loadings, Figure 5.13. The platinum loading for each electrode was calculated using the projected area of the electrolyte pellet ($A = \pi(19\ mm/2)^2$) and the nominal thickness of the platinum layer (5, 15, 30, 45 nm) to calculate the volume and the total mass of the deposited platinum. All electrodes show a higher mass normalized activity then the best thin film electrode. Electrodes with 15 nm sputtered platinum show an 26, 29 and 32-fold enhancement in the mass normalized activity of platinum as compared to the best result obtained by controlled thin film electrodes.

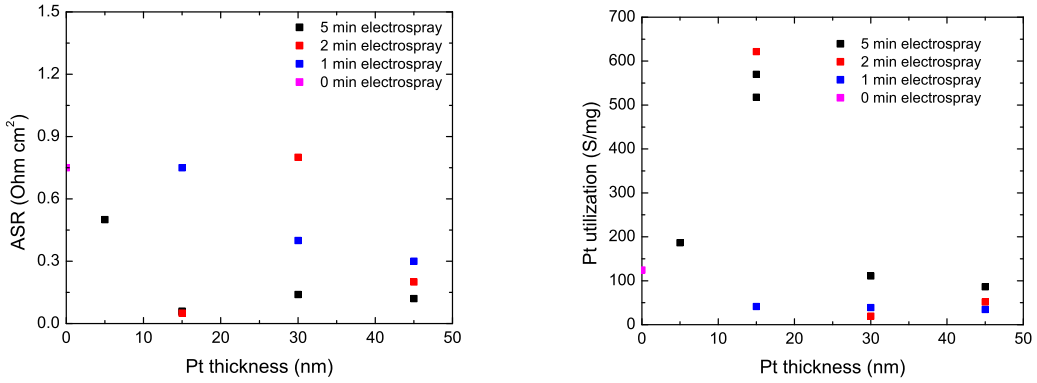

Figure 5.13: (a) Area specific resistance and (b) platinum utilization of high surface area thin film electrodes (sputtering)

Composite electrodes obtained via electrospray and sputter deposition are thought to contain a high density of edges, i.e. triple phase boundary interfaces with the electrode, electrolyte, and gas phase, in addition to the large continuous surface area, providing a two phase boundary interface. We speculate that the high mass normalized activities reported here are based on the intrinsically higher activity of the triple phase boundaries compared the two phase boundary alone. This theory is cor-

roborated by the fact that nominally thicker platinum films are expected to be more continuous and have fewer edges or triple phase boundaries and have higher area specific resistance values despite the higher platinum loading. At the other extreme, very thin films (5 nm here) may coarsen under solid acid fuel cell operating conditions and the developing platinum islands or particles loose electric interconnectivity and hence do not contribute to the overall electrode current. Therefore, the platinum utilization and mass normalized activity values are low. The optimal platinum thin film thickness of the electrodes studied here is 15 nm, providing a high density of triple phase boundaries that are still electrically connected to the current collector of the electrode.

5.4.2 MOCVD platinum on high surface area electrolyte nanostructures

Figure 5.14 shows two SEM images with low and high magnification of 0.7 mg/cm^2 platinum deposited via MOCVD onto electrosprayed nanostructure consisting of CsH_2PO_4 and PVP, deposited prior onto a cold pressed CsH_2PO_4 pellet. The platinum layer is ca. 50 nm thick, consisting of 50 nm diameter grains.

Figure 5.15 shows two SEM images with low and high magnification of 0.4 mg/cm^2 platinum deposited via MOCVD onto electrosprayed nanostructure consisting of CsH_2PO_4 and PVP, deposited prior onto a cold pressed CsH_2PO_4 pellet. The platinum layer is ca. 20 nm thick, consisting of 20 nm well interconnected platinum particles.

Figure 5.16 shows two SEM images with low and high magnification of $<$0.2 mg/cm^2 platinum deposited via MOCVD onto electrosprayed nanostructure consisting of CsH_2PO_4 and PVP, deposited prior onto a cold pressed CsH_2PO_4 pellet. $\sim$ 10 nm isolated platinum particles are visible as bright areas on the CsH_2PO_4 surface.

Figure 5.17 shows AC impedance spectra for the three different types of electrodes with (a) 10 nm Pt particles, (b) 20 nm Pt particles (three different samples), and (c) 50 nm Pt particles and the area specific electrode resistances of 37 Ωcm^2, 0.55 - 0.74

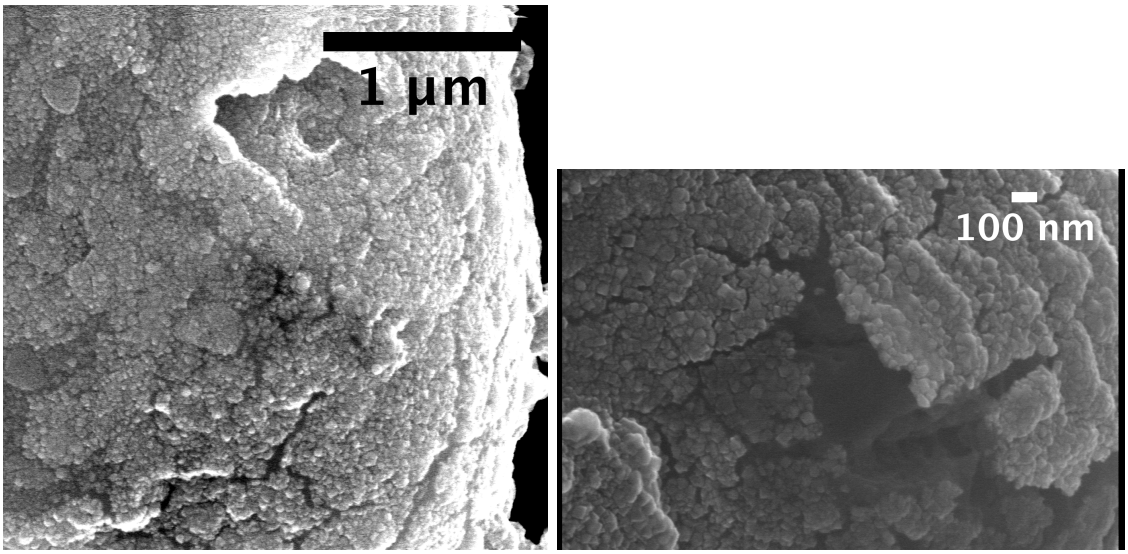

Figure 5.14: (a) low magnification and (b) high magnification SEM image of 0.7 mg/cm^2 platinum deposited via MOCVD onto electospray porous CsH_2PO_4 nanostucture

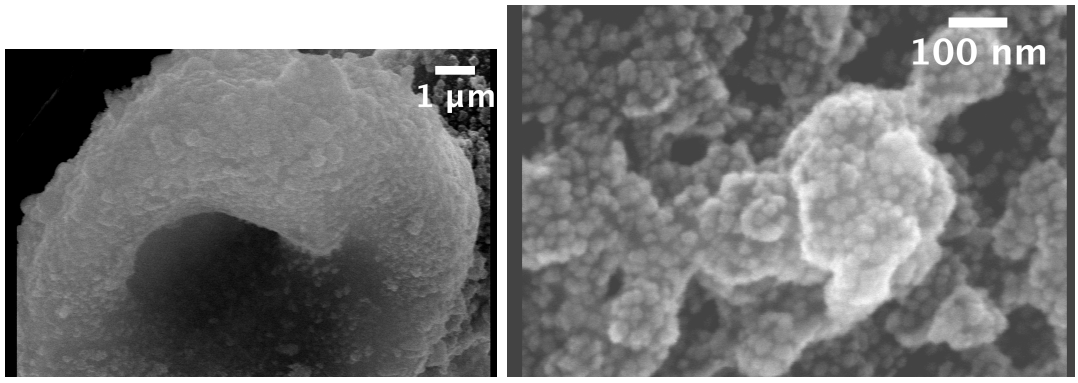

Figure 5.15: (a) low magnification and (b) high magnification SEM image of 0.4 mg/cm^2 platinum deposited via MOCVD onto electospray porous CsH_2PO_4 nanostucture

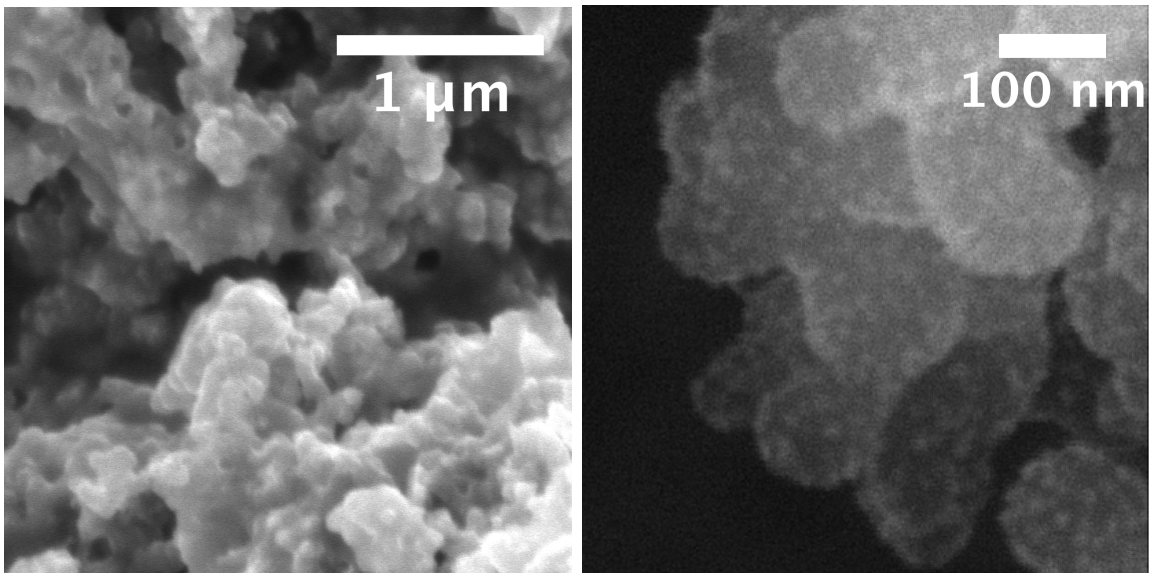

Figure 5.16: (a) low magnification and (b) high magnification SEM image of <0.2 mg/cm^2 platinum deposited via MOCVD onto electospray porous CsH_2PO_4 nanostucture

Ωcm^2, and 0.16 Ωcm^2 respectively.

From the scanning electron microscopy images, it is evident that with larger platinum particles, the degree of particle interconnectivity increases. Electrodes with 10 nm isolated platinum particles deposited, the large impedance value can be explained by low platinum utilization, resulting in 0.3 S/mg mass normalized activity. Electrodes with 20 nm platinum particles deposited have higher platinum utilization and a mass normalized activity of 3.3 - 4.5 S/mg is obtained. The electrode with the largest platinum loading and 50 nm platinum particles forming a continuous platinum layer has the highest platinum utilization and mass normalized activity of 9 S/mg.

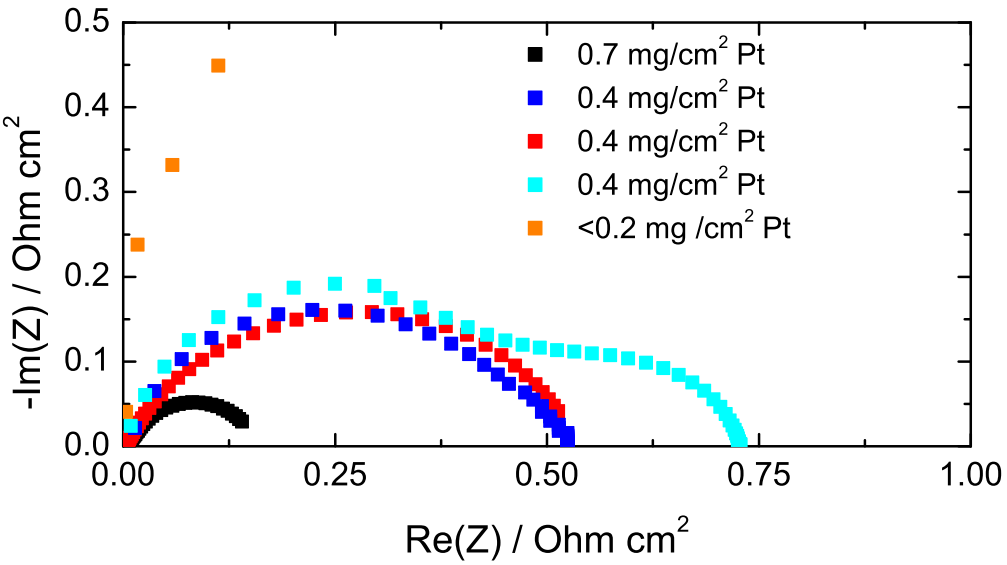

Figure 5.17: Impedance spectra of symmetric cells with electrosprayed CsH_2PO_4 + PVP + MOCVD deposited Pt, all measured at T=240°C, pH_2=0.6 atm, and pH_2O=0.4 atm

5.5 Conclusion

Two new methods to fabricate solid acid fuel cell electrodes have been explored, with the aim of maximizing the catalytically active two phase boundary area between the electrolyte CsH_2PO_4 and platinum catalyst. The objective was to improve the area specific resistance of the electrode without increasing the platinum loading.
To this end, CsH_2PO_4 nanostructures obtained via previously optimized electrospraying, deposited directly onto a cold pressed CsH_2PO_4 pellet have been used as the substrate for platinum thin film deposition. Thin films with varying thickness and interconnectivity have been obtained via magnetron sputtering and metalorganic chemical vapor deposition.

A.C. impedance spectroscopy measurements in humidified hydrogen environment showed that the best electrodes obtained via sputter deposition matched the state of the art area specific resistance (0.055 cm^2) but with a dramatic reduction of platinum loading (from 7.7 mg/cm^2 to 3.2 $\mu g/cm^2$). Remarkable mass normalized activity values have been obtained with sputter deposited platinum thin films, as high as 550 S/mg, representing a 32-fold improvement over results obtained with the best platinum thin films deposited onto polished electrolyte layers. Shadowing effects during deposition may lead in the case of electrolyte nanostructures to significantly higher density of triple phase boundaries and a varying thickness of the platinum film and the intrinsically higher catalytic activity.

Platinum thin films obtained via MOCVD are expected to have a more uniform coverage of the CsH_2PO_4 structure. The lack perfect electronic interconnectivity and therefore lower than ideal platinum utilization do not yield extremely high mass normalized activities but still represent a smaller four fold improvement over previous platinum mass normalized activity values (from 2.2 to 9 S/mg). Further optimization of the film thickness and grain size may result in similarly high mass normalized activities as in the case of sputter deposited platinum thin films.

Chapter 6

Carbon nanotubes as electronic interconnects in solid acid fuel cell electrodes

A. Varga, M. Pfohl, N.A. Brunelli, M. Schreier, K. P. Giapis, S. M.Haile, Carbon nanotubes as electronic interconnects in solid acid fuel cell electrodes, *submitted*

6.1 Abstract

Carbon nanotubes have been explored as interconnects in solid acid fuel cells to improve the link between nanoscale Pt catalyst particles and macroscale current collectors. The nanotubes were grown by chemical vapor deposition on carbon paper substrates, using nickel nanoparticles as the catalyst, and were characterized by scanning electron microscopy and Raman spectroscopy. The composite electrode material, consisting of CsH_2PO_4, platinum nanoparticles, and platinum on carbon-black nanoparticles was deposited onto the nanotube-overgrown carbon paper by electrospraying, forming a highly porous, fractal structure. AC impedance spectroscopy in a symmetric cell configuration revealed a significant reduction of the electrode impedance as compared to similarly prepared electrodes without carbon nanotubes.

6.2 Introduction

In the present work, we pursue here a strategy for attaining this goal that stems from several recent experimental observations and achievements. First, it has been established that the conventional composite electrode in SAFCs, comprised of electrolyte particles, Pt nanoparticles, and Pt on graphite, has activity that scales inversely with electrolyte particle size. [8] That is, a reduction in the electrolyte particle size from 1150 nm to 160 nm (with a fixed Pt loading), has led to a monotonic and significant reduction of the electrode overpotential. [8] This is believed to result from an increase in the number density of catalytically active sites within a given volume of electrode material. Second, it has been possible to estimate the inherent or limiting activity for Pt on a per unit mass basis in a dense, thin-film (7.5 nm) electrode geometry [14]. Deviations from the -ideal- value of the mass-normalized activity of the well-defined structure provide a measure of Pt utilization in composite structures. Third, the catalyst-mass-normalized activity in the finest composite structures we have been able to prepare to date, obtained by the method of electrospray [33], is substantially lower than the ideal value. This low relative activity suggests that the Pt in the composite structure is poorly utilized, which, in turn, may be the result of poor electronic connectivity between Pt nanocatalyst particles and the exterior current collector. That is, despite the reduction in the electrolyte particle size and the creation of a highly porous, fractal electrode with interconnected nanoscale electrolyte particles, a large fraction of the Pt particles are apparently isolated electrically and cannot deliver current. Here we explore the potential of carbon nanotubes (CNTs) grown directly on the current collector to serve as conductive interconnects that link Pt nanoparticles to the exterior circuit. While the focus is on solid acid fuel cells (SAFCs), the approach may be broadly applicable to lower temperature fuel cells. Indeed, the utility of carbon nanotubes as platinum catalyst supports for PEM fuel cells has been discussed in the recent literature. [95–98] Here we are particularly interested in incorporating CNTs in the anode of SAFCs, at which their possible reaction with oxygen is less of a concern than at the cathode.

6.2.1 Experimental

6.2.2 Carbon nanotube synthesis

Carbon nanotubes (CNTs) were grown on carbon paper substrates by chemical vapor deposition (CVD) using Ni nanoparticles as the catalyst and acetylene as the gaseous carbon source. [99] Nickel nanoparticles were synthesized following a procedure described by Metin et al. [100] In brief, 1.03 g of nickel acetylacetonate was mixed with 60 mL of oleylamine and 1.2 mL of oleic acid under a nitrogen environment. Moisture and oxygen were removed from this solution by heating it to 110°C and holding at that temperature for one hour. Separately, 1.06 g borane tributylamine complex was dissolved in 8 mL of oleylamine. The nickel-containing solution was cooled to 90°C and the second solution rapidly injected into it to induce the reduction of nickel acetylacetonate by borane tributylamine. The reaction was allowed to proceed for 60 min. After cooling to room temperature, the organic products were removed by adding 120 mL of ethanol, centrifuging (3000 rpm for 10 min), and then decanting. The resulting oleylamine-capped particles were then re-dispersed in hexane. Typical particle sizes obtained by this method are 3.2 nm [100]. Immediately prior to dispensing on the carbon paper, the suspension was subjected to ultra-sonication for one hour to encourage the break-up of agglomerates. The catalyst particles were applied to the carbon paper substrates (Toray-H-120, 5 Ã 5 mm2 in area) by spin coating. Two drops of the solution were dispensed to each substrate as it was spun at 2000 rpm for 15 sec, resulting in a catalyst loading of ~ 0.25 mg/cm^2.

The catalyst-loaded substrate was then placed in the center of an in-house CVD reactor consisting of a quartz tube (2.5 cm dia. and 61.5 cm length), a tube furnace (Lindberg/Blue M Mini-Mite, monitored with a K-type thermocouple), and mass flow controllers, Figure 6.1.

The details of the growth protocol employed (typical of procedures reported in the literature [99]) are given in Table 6.1. The initial heating to 800°C was carried out under argon and followed by a 10-min anneal under a mixture of hydrogen and argon to ensure the reduction of any NiO to Ni. The oleylamine, with a boiling point

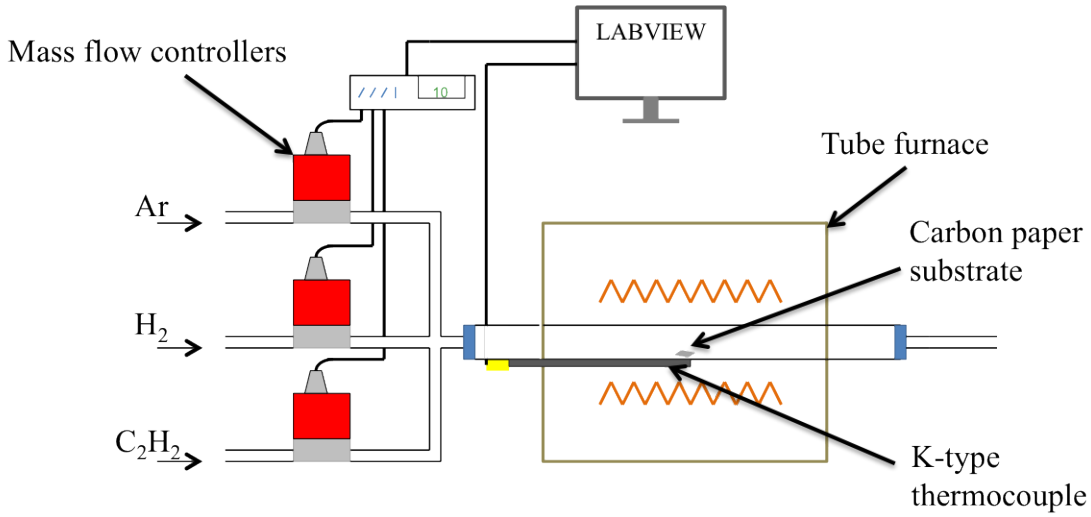

Figure 6.1: CVD apparatus for MWCNT growth

much lower than 800°C [101,102], is presumably volatized before or during the anneal step, although some carbon may be incorporated into the catalyst particles during these stages. The 10-min growth step was carried out under a mixture of acetylene, hydrogen, and argon. The sample was subsequently cooled under argon flow.

Table 6.1: Conditions for CVD growth of CNTs used in electrodes for solid acid fuel cells

	Ramp	Anneal	Grow	Cool
Temperature (°C)	20 → 800	800	800	800 → 20
Ramp rate (°C/min)	15	0	0	Passive
Time (min)	52	10	10	30
Argon (sccm)	750	750	750	750
Hydrogen (sccm)	0	250	250	0
Acetylene (sccm)	0	0	16	0

6.2.3 Electrode fabrication

Composite electrodes comprising CsH_2PO_4 and Pt were deposited on carbon paper substrates by electrospray using methods described by Varga et al. [33] Both neat (as-

Table 6.2: Electrospray solution composition

	Solution 1	Solution 2*	Control
CsH_2PO_4 (g/L) (in house)	10	10	10
Platinum black (g/L) Alfa Aesar, Stk no. 43838, $\sim$30 m^2g^{-1}	3	5	0
Platinum (40 wt%) on Carbon (g/L) Alfa Aesar, Stk no. 42208	3	5	0
Polyvinylpyrrolidone (g/L) Alfa Aesar, Stk no. 41626 M_W 8000u	12	20	20
Deionized water-methanol (wt %) Macron Chemicals, 3016-16	50	50	50

purchased) and CNT-overgrown carbon paper substrates were employed. In addition, two different electrospray solutions were utilized, the detailed compositions of which are summarized in Table 6.2.

Both contained dissolved CsH_2PO_4 as well as dispersed Pt. The CsH_2PO_4 was synthesized in-house using Cs_2CO_3 (Alfa Aesar, 99% metal basis, Stk no. 12887) and H_3PO_4 (Mallinckrodt Chemicals, 85%, Stk no. 2788-14) as precursors. The two solutions differed in the Pt content (with the ratio of Pt black to Pt on carbon held constant), varied as a means of probing the effectiveness of the CNTs for providing current collection pathways at different Pt loadings. Polyvinylpyrrolidone (PVP) was added in both cases to aid in the suspension of the Pt and carbon solid components, and the PVP-to-solids weight ratio was also held constant between the two solutions. As a control, a solution of CsH_2PO_4 and PVP (but no Pt) was electrosprayed on CNT-overgrown carbon paper to assess the possible contribution of CNTs and/or Ni nanoparticles to any observed catalytic activity.

As in our previous work, [33] the electrospray chamber was operated under ambient pressures, the temperature was fixed at 140 °C (to facilitate solvent evaporation), the voltage between the capillary tip and substrate was 4.5 kV, the tip to substrate distance was 2.5 cm, the nitrogen sheath gas velocity was 50 cm/min, the liquid flow rate was 1 mL/h, and deposition was carried out for 1 hour. The quantity of mate-

rial deposited onto the substrate was determined from a comparison of the pre- and post-deposition weights, as measured using a microbalance, from which the Pt loading was computed. In continued analogy to our earlier study, for control electrodes not containing CNTs, an oxygen plasma treatment step (150 W power, 13.56 MHz frequency, 13.6 mTorr Ar + O_2 mixture, 4 min exposure) was employed in order to remove PVP5, which could otherwise coat the Pt catalyst particles and prevent electrochemical access. In the case of the CNT-containing electrodes, the oxygen plasma treatment step was omitted in case of damage to the carbon structures.

To facilitate electrochemical characterization, symmetric cells were prepared with general configuration:

carbon paper : composite electrode | CsH_2PO_4 | composite electrode : carbon paper

A disk of the electrolyte material (1.9 cm diameter and 1-2 mm thick) of $\sim$ 95% density was first obtained by uniaxially pressing (34 MPa). Two electrodes, each $\sim$ 2 mm^2 in area, were cut out from a given substrate and positioned in the middle of either side of the flat electrolyte pellet. The sandwich structure was then lightly pressed between inactive carbon paper current collectors.

6.2.4 Characterization

The morphological features of the samples were characterized with a scanning electron microscope (Zeiss 1550VP and Hitachi S-4100 field emission SEM) equipped with a secondary electron detector. The as-grown CNTs were further characterized by Raman spectroscopy (Renishaw M1000 Micro Raman Spectrometer System).

A.C. impedance spectra were collected at 240 °C under humidified hydrogen as a means of probing the hydrogen electro-oxidation reaction. Hydrogen gas ($>$ 99.95% purity) was bubbled through water held at 80°C to achieve a water partial pressure of 0.4 atm and supplied at a gas phase velocity 3.1 cm/min. Electrical data were acquired using an impedance analyzer (Autolab PGSTAT 32) over the frequency range 5 mHz to 1 MHz, a perturbation voltage amplitude of 10 mV, and zero D.C. bias.

Two different and four different cells created from solutions 1 and 2, respectively, with CNT-modified electrodes were characterized. Stability was evaluated for a representative sample (solution 2) by collecting data over a 8 - 12 h periods. Impedance data are reported as normalized with respect to the area of the carbon paper electrode over which CNTs were grown (active area).

6.3 Results and discussion

6.3.0.1 Summary of ideas

Images of the carbon paper substrate after CNT growth are presented in Figure 6.2.

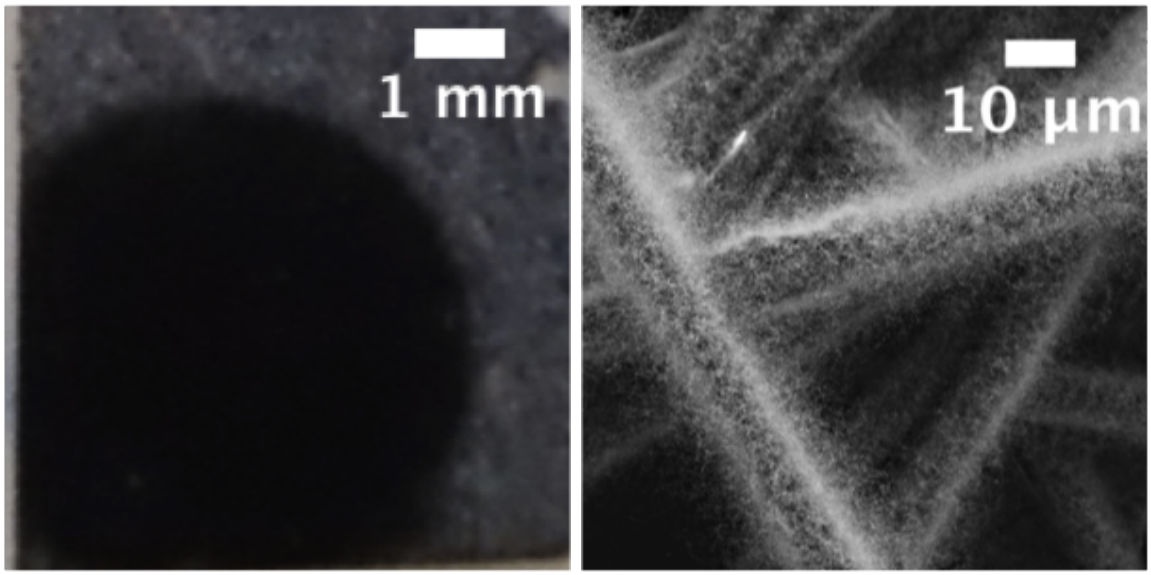

Figure 6.2: a) optical and b) SEM image of MWCNTs on carbon paper

The regions of the carbon paper where nickel nanoparticles had been deposited acquired a uniform black appearance demonstrating the effectiveness of these particles in catalyzing CNT growth, Figure 6.2. Other areas retained the grey appearance of the as-purchased substrate. Within the regions of CNT growth, the coverage over the carbon paper figures is visually uniform, Figure 6.2 b and 6.3 c. The diameter of the CNTs range from 15 to 25 nm and they extend out $\sim 8\ \mu m$ from the surface of the carbon paper fiber. A bright spot is evident at the tip of the CNT visible in

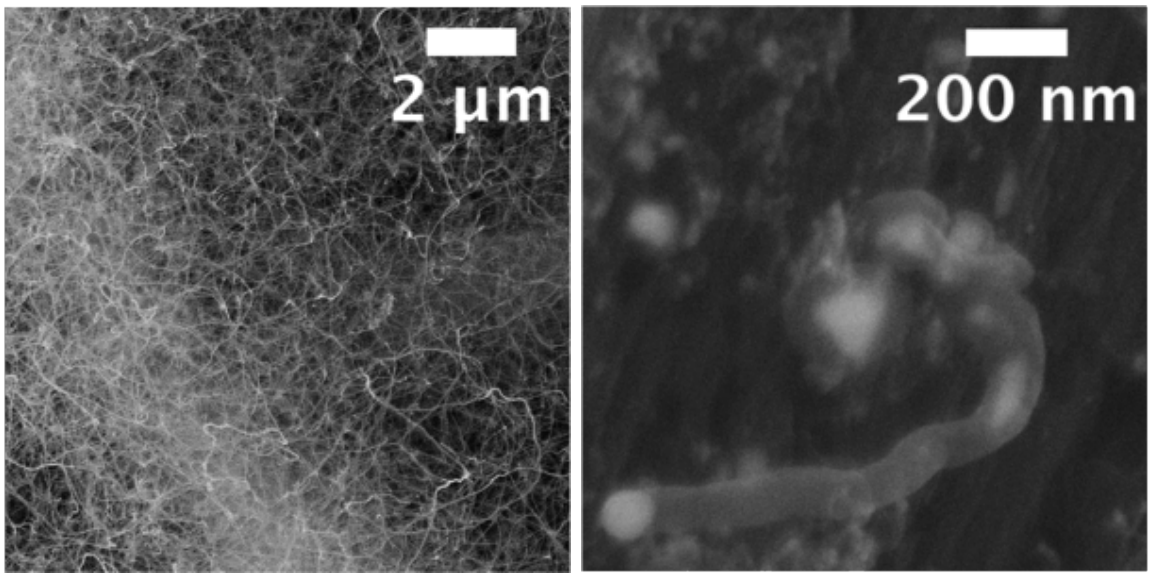

Figure 6.3: SEM images MWCNTs on carbon paper

Figure 6.3 d, an image collected in electron backscatter mode. This feature is believed to be the Ni catalyst particle, energy dispersive spectroscopy confirmed the general presence of Ni in the sample, and its location suggests that the tip-growth mechanism is operative [103]. The imaged nanoparticle is larger than the 3.2 nm expected from the Ni synthesis, likely due to coarsening during the high temperature anneal prior to CNT growth. Images of similarly prepared Ni particles annealed at 550 °C for 10 min under Ar revealed agglomerates 10 - 40 nm in diameter formed of 3.9 nm primary particles. [104] growth periods longer than 10 min did not result in longer CNTs. The large diameter of the CNTs suggests they are multi-walled [105].
Raman spectra for the CNTs are presented in Figure 6.4.

The spectra in Figure 6.4a correspond to measurements from four separate areas on a single substrate and are normalized with respect to the peak intensity of the G-band. The four spectra are nearly identical and corroborate the electron microscopy observation of generally uniform CNT growth across the substrate. A CNT sample, removed from the carbon paper substrate by ultra-sonication in ethanol and deposited on a Si wafer, had a Raman spectrum almost identical to that obtained from the CNT on carbon paper, Figure 6.4b. These two spectra (detached CNTs on Si and attached

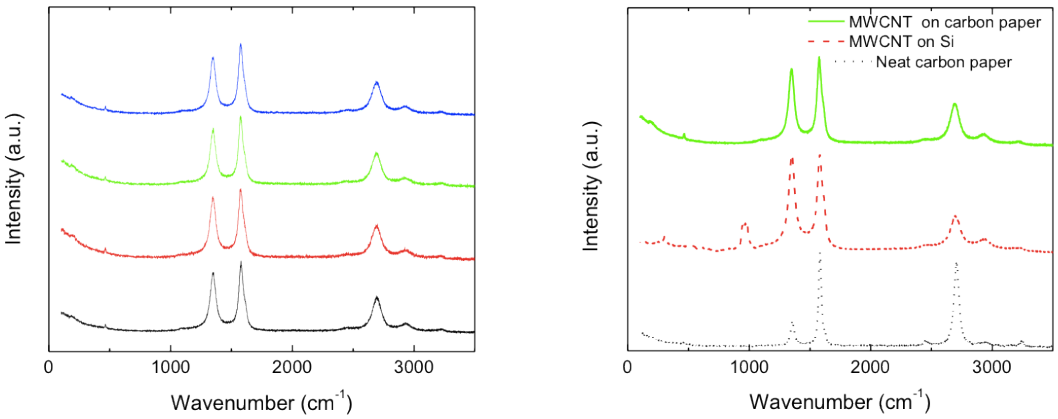

Figure 6.4: Raman spectra. (a) Spectra from four different positions of a single carbon paper substrate, and (b) comparison of spectra as indicated

CNTs on carbon paper) are, however, clearly distinct from that of the carbon paper alone, indicating that the attached CNTs on carbon paper largely, if not fully, mask the underlying substrate. The spectra for the CNTs are, in particular, distinguished from that of the substrate by the high intensity of the D band, consistent with the presence of highly graphitic carbon in the former [106]. The absence of a peak in the 100 to 300 cm^{-1} range, at which the radial breathing mode would be observed, is typical of multi-walled CNTs. [107] The composite electrodes obtained by electrospraying on the carbon paper substrates acquired differing morphologies depending on the presence or absence of the CNTs. As evident from the SEM images, Figure 6.5, the porosity was somewhat lower for deposition on substrates with CNTs. While the images presented in 6.5 are for solution 1, similar results were obtained for solution 2. At this stage the reason for the distinct morphologies is unknown.

Figure 6.6 shows the impedance spectra in the Nyquist representation: $-Z_{imag}$ vs. Z_{real} as parametric functions of frequency, for four different symmetric cells fabricated with solution 1 - lower platinum loading - after a 3 to 8 hour initial equilibration time. The data presented are those obtained once the change in electrode impedance fell below a rate of 4 % per hour. For clarity, the electrolyte contribution, a constant displacement along the real axis, is subtracted from the data. Cells with both CNTs

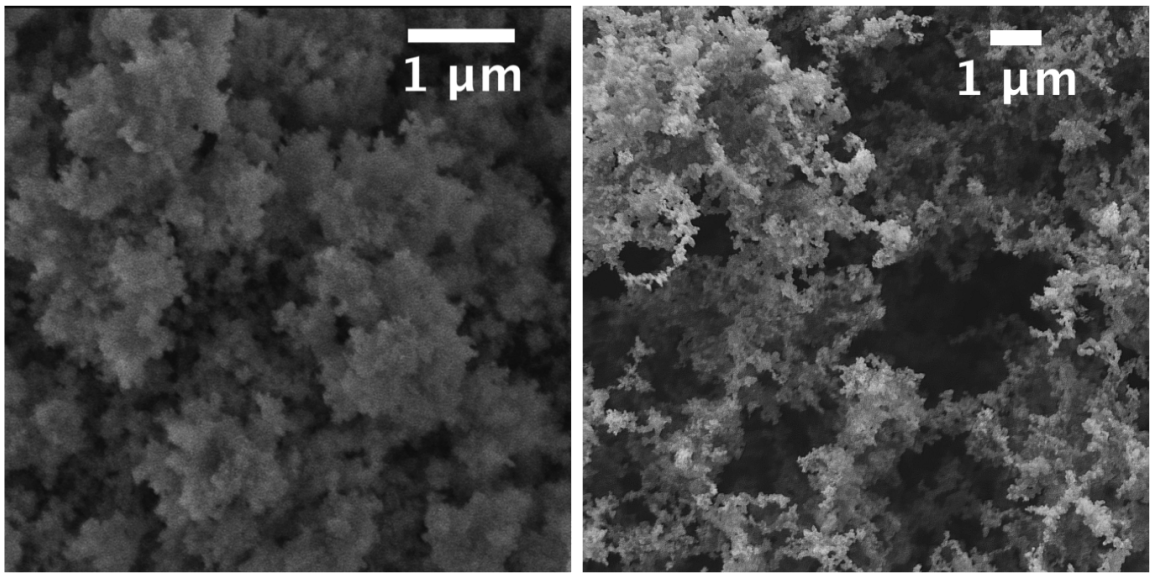

Figure 6.5: SEM images of the electrosprayed composite electrodes, consisting of CsH_2PO_4, platinum black, platinum on carbon black and PVP deposited onto carbon paper (a) with and (b) without MWCNTs

and Pt in the electrodes showed a five-fold reduction of the electrode impedance as compared to those with only Pt (6 Ω cm^2 vs. 30 Ω cm^2). Furthermore, excellent reproducibility is evident for the two electrodes containing both CNTs and Pt.

A similar result, also after a 3-8 hour initial equilibration time, was obtained in the case of cells fabricated using solution 2 (higher Pt loading), Figure 7.18. In this case, however, the presence or absence of CNTs leads to a three-fold difference in impedance (0.5 Ω cm^2 vs. 1.5 Ω cm^2). Again, reproducibility is high, and the results for the cell with Pt but no CNTs match previously reported results. [33] Moreover, the enhancement obtained using the CNT-modified carbon paper occurs despite the potential presence of residual PVP, which has been shown to have a slight negative impact on activity. [33] Overall, the low impedance values obtained in the presence of the CNTs directly translate into five- and three-fold improvements in the catalyst utilization, respectively. Specifically, the mass normalized activity [inverse of (area normalized electrode impedance x Pt loading)] was increased from 0.2 to 1.0 S mg^{-1} for the lower Pt loading and from 2.2 to 6.6 S mg^{-1} for the higher Pt loading.

In the absence of Pt, the CNT-modified electrode displayed negligible activity, as

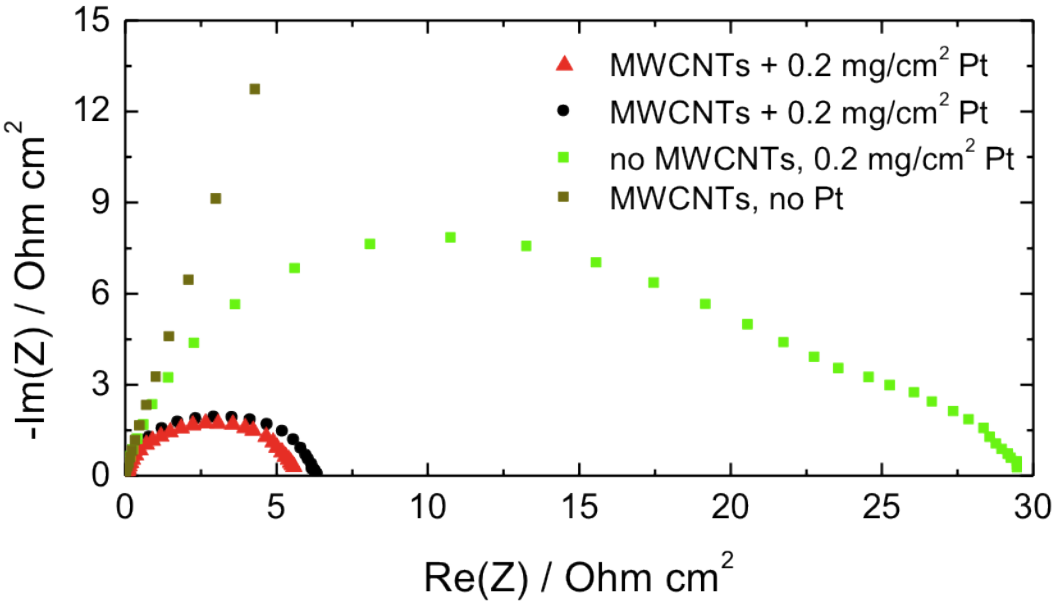

Figure 6.6: Impedance spectra for two composite electrodes with MWCNTs and one without but otherwise identical; Solution 1 with lower platinum loading. The reduced electrode impedance is attributed to better catalyst interconnectivity

shown in both Figures 6.6 and 7.18.

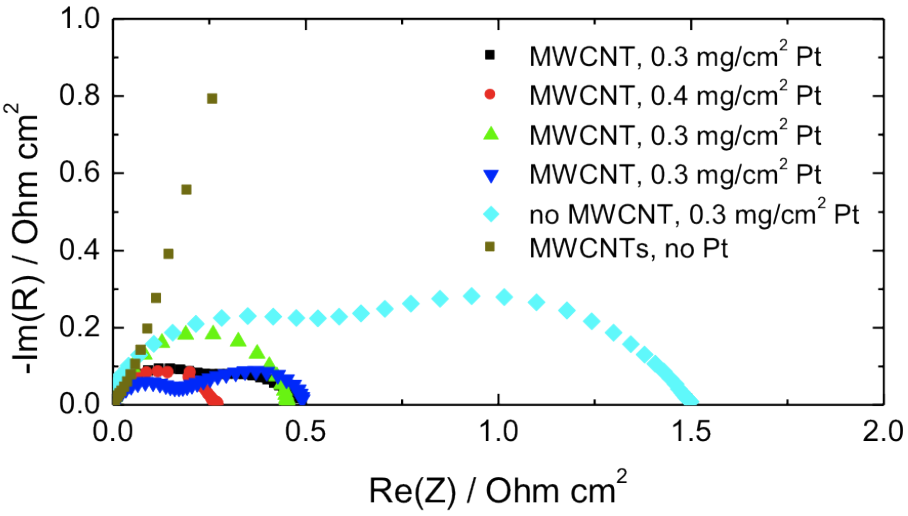

Figure 6.7: Impedance spectra for four composite electrodes with MWCNTs and one without but otherwise identical; Solution 2 with higher platinum loading. The reduced electrode impedance is attributed to better catalyst interconnectivity

Thus, neither the CNTs nor the residual (carbon-saturated) Ni can be responsible for the observed enhancement over Pt-only electrodes when both CNTs and Pt are present. Furthermore, although the possibility of a synergistic interaction between Ni and Pt cannot be ruled out, the relatively low electrospray deposition and measurement temperatures suggest that these two types of particles remain as discrete units, with little likelihood of interdiffusion even where they do come into contact.

The observations of substantially enhanced activity in CNT + Pt electrodes over those with Pt only and of negligible activity for electrodes with only CNTs suggest strongly that the CNTs are providing the desired electrical contacts to the Pt catalyst particles. The greater impact of the CNTs at the low Pt loading (a five-fold improvement vs. a three-fold improvement at high Pt loading) is consistent with the occurrence of a greater fraction of electrically isolated catalyst particles when the amount of Pt is low. The CNT overgrowth to carbon paper thus provides a larger benefit for lower platinum catalyst loading.

Beyond improved activity, the CNT modified electrodes displayed good stability. The electrode impedance either decreased over time to a stable value or remained unchanged during the course of evaluation. An example of the former behavior is shown in Figure 6.8, which summarizes measurements for an electrode prepared using solution 2 (higher Pt loading). Two electrode impedance responses are evident for this cell, as reflected by the presence of two arcs in the Nyquist plot, Figure 6.8 a, a feature generally present in all of the electrodes examined (Figures 6.6 and 7.18). Both arc widths decrease substantially with time to reach stable values after about 8 hr. While the physical origin of the two distinct responses is unknown, we attribute the overall decrease in the global impedance, Figure 6.8b, to either an improvement of the contact between the electrosprayed CsH_2PO_4 particles of the composite electrode and the pre-pressed CsH_2PO_4 pellet serving as the electrolyte, or due to the volatization of residual PVP during high temperature exposure. The eventual stabilization of the electrochemical response suggests that after a moderate period of exposure to the light pressure of the electrochemical measurement apparatus the morphology of the electrode/electrolyte interface adopts a fixed configuration, and/or that the process of PVP removal is completed.

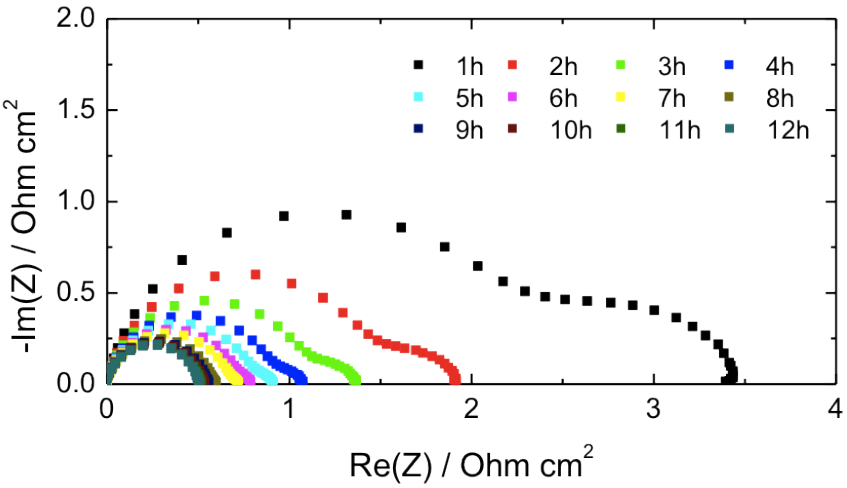

Figure 6.8: Impedance spectra for a composite electrode with MWCNTs - solution 2, with higher platinum loading - taken over a 12 hour period, showing good stability after remarkable improvement over an initial 8 hour period

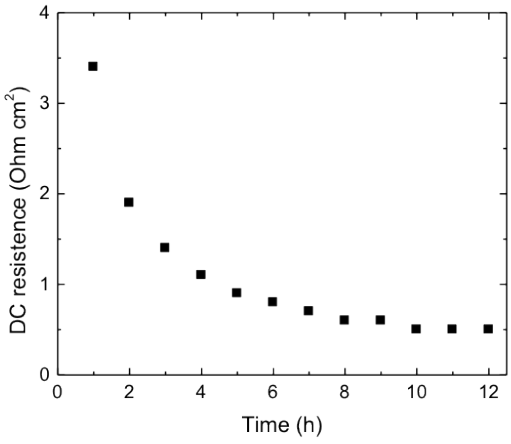

Figure 6.9: Low frequency intercept of impedance arcs vs. time replotted - solution 2

6.4 Conclusion

Direct growth of carbon nanotubes onto the current collector (carbon paper) applied to composite electrodes in solid acid fuel cells has resulted in a multi-fold decrease in the electrochemical reaction impedance and a commensurate increase in the Pt utilization relative to similar electrodes without carbon nanotubes. The increased electrode performance is attributed to better catalyst utilization as a result of improved interconnectivity. The CNTs, with diameters of a few nanometers and lengths in the micron range, provide a means of matching the length scales of the Pt catalyst nanoparticles and the micrometric fibers of the carbon paper current collector. While the highest mass normalized activity achieved here, 6.6 S mg^{-1}, is lower than the measured value of 19 S mg^{-1} for Pt thin films, [14] the enhancement is still substantial. Additional gains may be realized by further optimizing the electrode structure, e.g., by growing longer CNTs and/or ensuring the absence of defects that may have a negative impact on CNT electronic conductivity.

6.5 Acknowledgements

This material is based upon work supported by the National Science Foundation under Grant No. DMR-0520565. Funding was also provided by the Gordon and Betty Moore Foundation through the Caltech Center for Sustainable Energy Research. M.P. and M.S. were partially supported on ETH Zurich fellowships. The authors thank Prof. George Rossman for invaluable assistance with Raman spectroscopy measurements. We are also indebted to Prof. Harry Gray, without whose generosity this work would not have been possible.

Chapter 7

Carbon nanotubes as solid acid fuel cell electrocatalysts

7.1 Abstract

Commercial application of low and intermediate temperature fuel cells has been hindered by the need for precious metals as electrocatalysts. State of the art solid acid fuel cell electrodes consist of composites of CsH_2PO_4, platinum black, and platinum on carbon nanoparticles. Here we show unprecedented catalytic performance of nitrogen doped and more importantly, undoped carbon nanotubes as oxygen electroreduction- as well as water splitting catalysts. The carbon nanotubes were grown by chemical vapor deposition on carbon paper using nickel nanoparticles as the gowth catalyst. The as grown carbon nanotubes were characterized via scanning electron microscopy and Raman spectroscopy. Symmetric cells for AC impedance spectroscopic measurements in humidified oxygen were fabricated by cold-pressing the carbon nanotube covered carbon paper into fine CsH_2PO_4 powder. The five best electrodes showed stable performance over at least 24 hours with area specific resistance values ranging from 0.2 to 0.4 Ωcm^2 at 240°C. Measurements with a DC bias of 100 to 700 mV for one representative sample yielded remarkable current densities of up to 3 A/cm^2 demonstrating highly efficient water splitting and oxygen reduction catalysis.

In the presented work, the CNTs were partly grown by others.

7.2 Introduction

All solid acid fuel cell electrodes to date employ platinum as the electrode-catalyst either in the form of nanoparticles, thin films, or nanoparticle alloys with other precious metals, such as palladium. [4,6,8,108] As in other low and intermediate temperature fuel cell, the oxygen electroreduction at the cathode has been identified as the performance limiting process. [6,109,110] Large platinum loadings of up to 7.7 mg cm^{-2} are required to achieve competitive power densities, rendering these types of fuel cells economically non-viable. However, recently, nitrogen doped carbon nanotubes and graphene sheets have been reported to be catalytically active in polymer electrolyte fuel cells, facilitating the oxygen reduction reaction at the cathode. [111–116] In the present work we aim to create high performance, precious metal-free solid acid fuel cell cathodes, using nitrogen doped and undoped carbon nanotubes as the only electrocatalyst. They are grown directly on carbon paper current collector using nickel nanoparticles as the growth catalyst.

7.2.1 Experimental

7.2.2 Catalytically active carbon nanotube synthesis

Chemical vapor deposition was used as the growth method to overgrow carbon paper with undoped, defective carbon nanotubes, a standard method reported previously. [105, 117] Nickel nanoparticles served as the growth catalyst and acetylene gas as the carbon source. The nickel nanoparticles were synthesized as described by Metin et. al. [100] As described in chapter 6 of that thesis, Ni nanoparticles were synthesized by Nicholas A. Brunelli. The resulting oleylamine-capped particles were dispersed in hexane. Typical particle sizes obtained by this method are 3.2 nm [100], but larger agglomerates are likely to be present. Immediately prior to application of the catalyst to the substrate for CNT growth, the suspension was sonicated for one hour to encourage the break-up of agglomerates. Two drops of the solution were applied to each carbon paper substrate (Toray-H-120, 5 x 5 mm2 in area) by spin coating (2000 rpm, 15 sec), to obtain a catalyst loading of ~ 0.25 mg/cm^2.

The catalyst-containing substrate was then placed in the center of an in-house chemical vapor deposition (CVD) reactor consisting of a quartz tube (2.5 cm dia. and 1 m length), a tube furnace (Lindberg/Blue M Mini-Mite, monitored with a K-type thermocouple), and mass flow controllers, Figure 7.1 and 7.2.

Table 7.1: Conditions for CVD growth of nitrogen doped CNTs used in electrodes for solid acid fuel cells

	Ramp	Anneal	Grow	Cool
Temperature (°C)	20 → 800	800	800	800 → 20
Ramp rate (°C/min)	15	0	0	Passive
Time (min)	52	10	10	30
Argon (sccm)	750	750	0	750
Hydrogen (sccm)	0	250	73	0
Acetylene (sccm)	0	0	16	0
Ammonia (sccm)	0	0	6/12/24	0

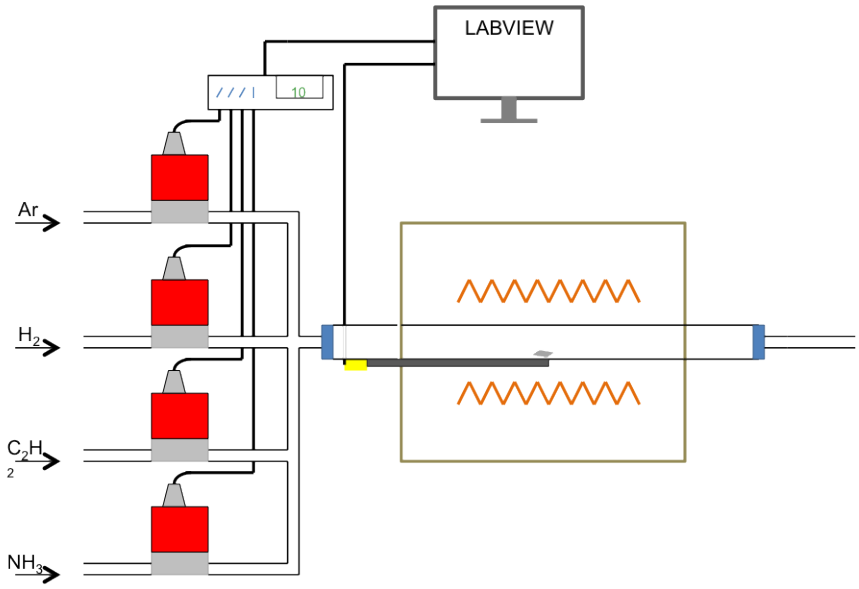

Figure 7.1: CVD apparatus for nitrogen doped CNT growth

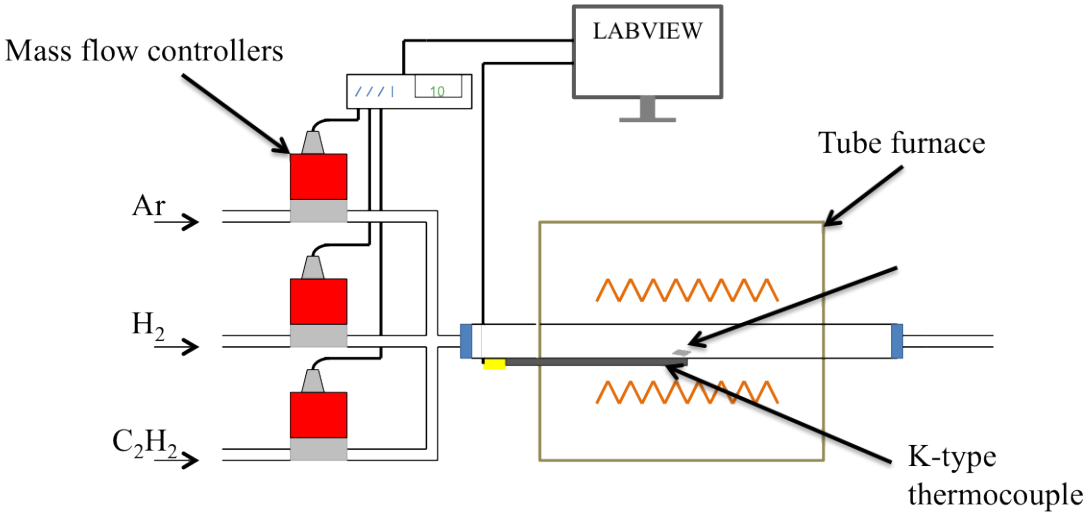

Figure 7.2: CVD apparatus for undoped, defective CNT growth

Table 7.2: Conditions for CVD growth of undoped, defective CNTs used in electrodes for solid acid fuel cells

	Ramp	Anneal	Grow	Cool
Temperature (°C)	$20 \rightarrow 800$	800	800	$800 \rightarrow 20$
Ramp rate (°C/min)	15	0	0	Passive
Time (min)	52	10	10	30
Argon (sccm)	750	750	$*0*$	750
Hydrogen (sccm)	0	250	250	0
Acetylene (sccm)	0	0	16	0

Two different growth protocols and two separate CVD systems were used in order to exclude any chance of nitrogen cross-contamination.

The details of the growth protocols employed for nitrogen-doped CNTs and undoped CNTs are given in Table 7.1 and Table 7.2 respectively. The initial heating to 800 °C was carried out under argon and followed by a 10-min anneal under a mixture of hydrogen and argon to ensure the reduction of any NiO to Ni. The oleylamine (boiling point $\sim$ 350 °C) was also presumably removed before or during the anneal step. [101, 102] This was followed by a 10-min growth period in a gas mixture of hydrogen, acetylene and ammonia to grow nitrogen doped carbon nanotubes. Undoped carbon nanotubes on the other hand, were grown with acetylene and hydrogen only present and with *no* Ar present. Subsequently, the CVD reactor was allowed to cool passively in both case, in an argon environment.

After each growth period, the quartz reactor tube was burned out at 800° for 60 min using a ca. 50 sccm air flow.

7.2.3 Symmetric cell fabrication

7.2.3.1 Nitrogen doped CNT electrodes

With the aim of maximizing the density of triple-phase boundary interfaces between the electrolyte, the catalyst and the gas phase, CsH_2PO_4 nanoparticles were electro-

Table 7.3: Electrospray parameters employed for the deposition of CsH_2PO_4 nanoparticles onto carbon paper, overgrown with NCNTs)

Parameter	CsH_2PO_4 nanoparticles
Temperature (°C)	100
Voltage (kV)	5.5
Sheath gas flow rate (sccm)	1000
Mol% methanol in solution	50
CsH_2PO_4 concentration (g/L)	10
Solution flow rate (ml/h)	1

sprayed as described previously by [33], directly onto the carbon paper, overgrown with nitrogen doped carbon nanotubes (NCNTs). The electrospray deposition parameters are shown in Table 7.3.

For electrochemical measurements, symmetric cells were fabricated by cutting out a 2 mm diameter section of the composite eletrode (NTNCTs + CsH_2PO_4 nanoparticles) and lightly pressing onto both sides of a uniaxially cold pressed CsH_2PO_4 pellet, thus obtaining the general configuration, Figure 7.3.
Carbon paper | NCNT | electrosprayed CsH_2PO_4 | CsH_2PO_4 | electrosprayed CsH_2PO_4 | NCNT | Carbon paper

7.2.3.2 Undoped CNT electrodes

Fine grained CsH_2PO_4 powder (fine-CsH_2PO_4) was synthesized following the procedure described by K. Sasaki [18]. In brief, it consists of dissolving 10 mg of CsH_2PO_4 in 8.5 ml DI-water and injecting the solution into an ultrasonicated anhydrous methanol bath via a syringe (26G1/2). The precipitate is allowed to settle and the natant precipitate is decanted. The dried particles have a ~ 1 μm diameter.

For the electrodes, a 4 mm diameter hole was cut through the center of a 13

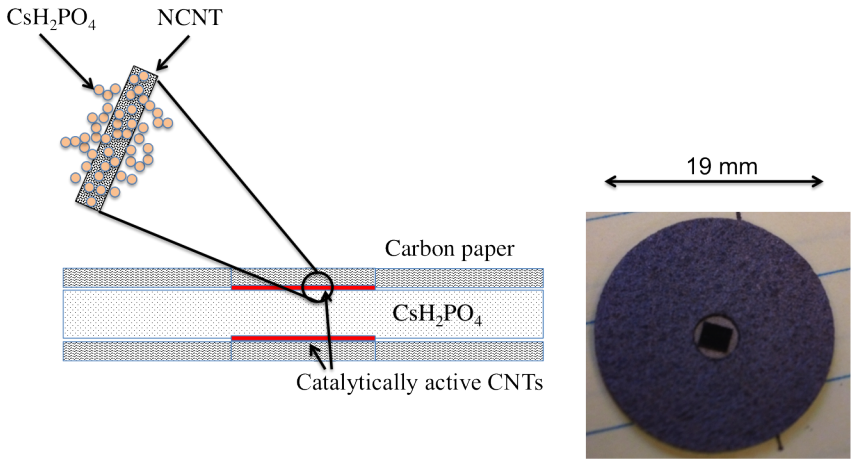

Figure 7.3: Schematic of symmetric cell assembly of NCNT + electrosprayed CsH_2PO_4 electrodes.

mm diameter blank carbon paper disk. A 4 mm diameter undoped CNT containing carbon paper disk was fitted into the hole. 200 mg of fine-CsH_2PO_4 powder was added and an identical electrode placed on the top, Figure 7.4. This assembly was uniaxially cold-pressed for 20 min under a pressure of 69 MPa to obtain the general configuration: Carbon paper | CNT | CsH_2PO_4 | CNT | Carbon paper

The solid symmetric cell was sandwiched between two stainless steel gas diffusion layers on either side for electrochemical characterization.

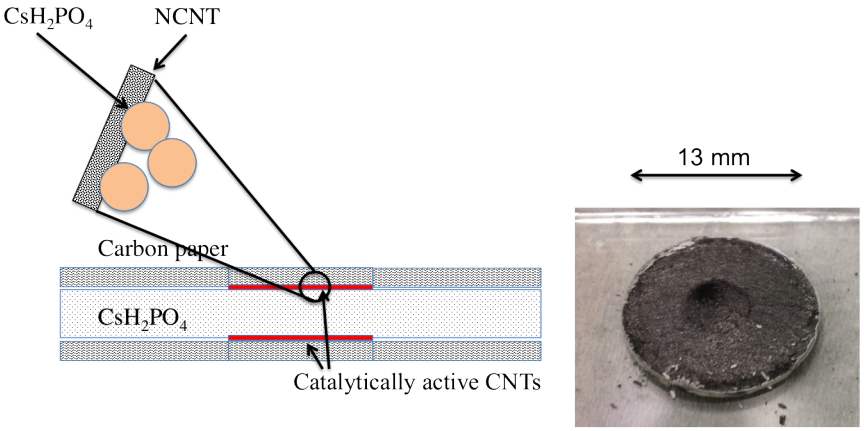

Figure 7.4: Schematic of symmetric cell assembly with electrodes containing undoped CNT

7.2.4 Characterization

The morphological features of the samples were characterized with a scanning electron microscope (Zeiss 1550VP and Hitachi S-4100 field emission SEM) equipped with a secondary electron detector. The as-grown CNTs were further characterized by Raman spectroscopy (Renishaw M1000 Micro Raman Spectrometer System), X-ray Photoelectronspectroscopy (M-Probe) and contact angle measurements with a contact angle goniometer (EM-500 Digital Camera).

A.C. impedance spectra were collected at 240 °C under humidified hydrogen and oxygen as a means of probing the hydrogen electro-oxidation and oxygen electroreduction reaction respectively. Hydrogen or oxygen gas ($> 99.95\%$ purity) was bubbled through water held 80°C to achieve a water partial pressure of 0.4 atm and supplied at a gas phase velocity 3.1 cm/min. Electrical data were acquired using an impedance analyzer (Autolab PGSTAT 32 or Solartron Analytical 1260) over the frequency range 5 mHz to 1 MHz, a perturbation voltage amplitude of 10 mV, and zero D.C. bias. Biased measurements were also conducted for symmetric cells containing undoped CNTs. The chemical stability of undoped CNTs was evaluated in a humidified oxygen environment using a mass spectromenter (Pfeiffer Vacum Omni Star) both using simple standalone electrodes and a symmetric cell under biased AC impedance measurements. The thermal stability of a representative standalone electrode was evaluated by increasing the temperature by 50°C steps and holding for 30 min in a 30 sccm humidified oxygen flow ($pH_2O = 0.4$ atm) and continuously monitoring the carbon dioxide and carbon monoxide concentrations.

7.3 Results and discussion

7.3.0.1 Nitrogen doped CNT electrodes

Images of representative samples of carbon paper after CVD growth of nitrogen doped CNTs are presented in Figure 7.5.

Bright spots at the end of the nanotubes indicate the presence of nickel growth

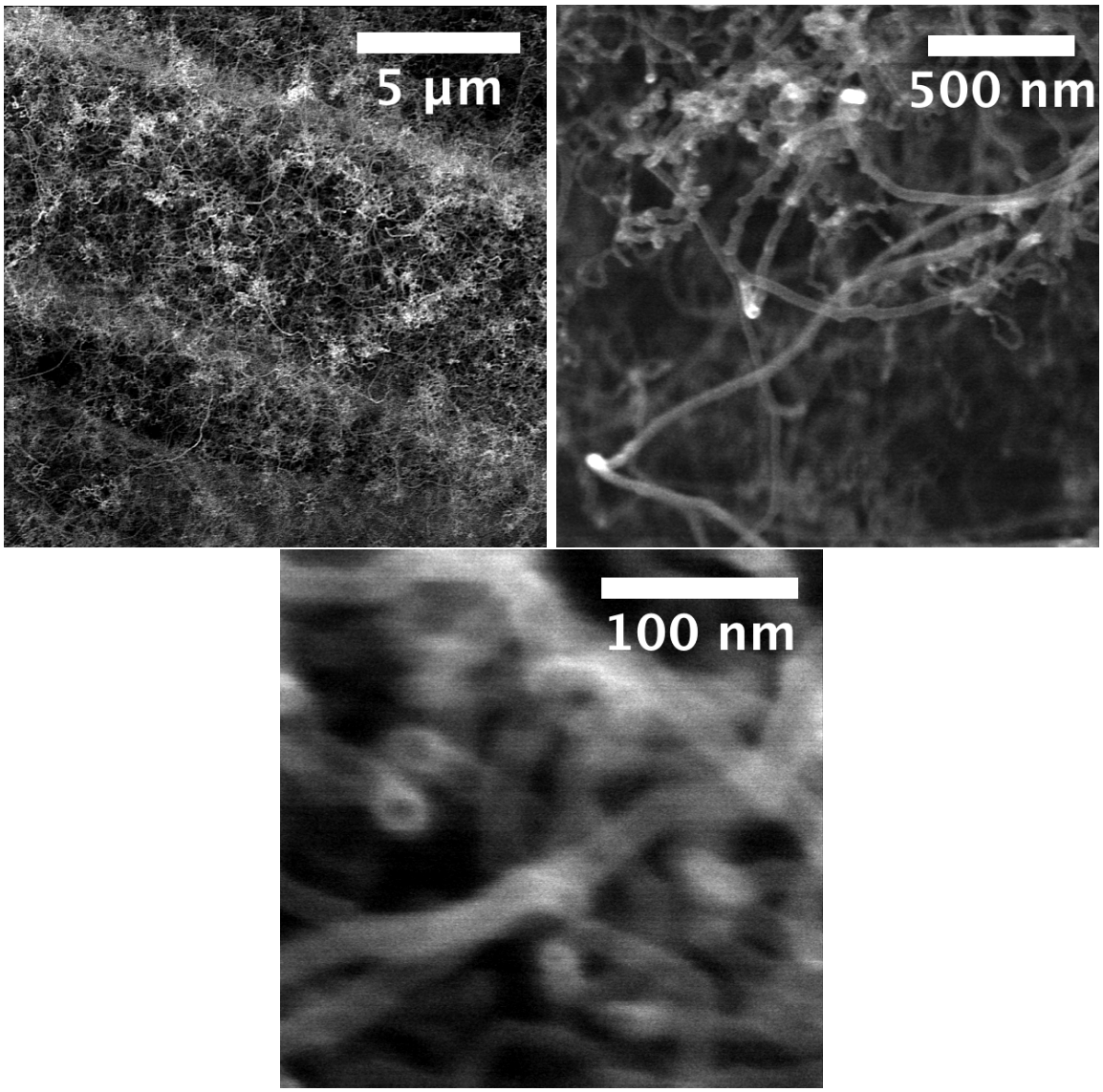

Figure 7.5: SEM images of as-grown nitrogen doped carbon nanotubes on carbon paper with (a) low (b) intermediate and (c) high magnification

catalyst and suggest that the tip-growth mechanism is active. The carbon nanotubes extend ca. 10 μm from the surface of the carbon paper fiber and their diameter ranges between 10 - 20 nm.

SEM images after electrospray deposition of CsH_2PO_4 nanoparticles are shown in Figure 7.6 at low magnification and 7.7 high magnification for varying deposition times (a) - (d). 100 - 200 nm interconnected CsH_2PO_4 particles form a porous layer on the carbon nanotubes, with increasing density with longer deposition times.

Figure 7.8 shows AC impedance spectra after an initial equilibration period for four different symmetric cells containing NCNTs as the catalyst, fabricated with different ammonia flow rates. A symmetric cell with standard, undoped CNTs was also measured as a reference. Electrodes fabricated with 12 sccm ammonia flow rate show good activity while the electrodes fabricated with 24 sccm ammonia flow show excellent activity.

The stability of the high performance symmetric cell was evaluated over a 24 hour period, Figure

7.3.0.2 Undoped carbon nanotubes

Figure 7.10 shows two representative SEM images of as grown undoped and defective carbon nanotubes on carbon paper at (a) low and (b) high magnification. As a comparison, Figure 7.11 shows standard non-active carbon nanotubes at the same (a) low and (b) high magnification obtained *via* the same recipe as described in Chapter 6 and used as electronic interconnects.

Significant differences between the defective and undoped (conventional) carbon nanotube morphologies is apparent from the SEM images. A wider distribution of lengths ($\sim$5 - 20 μm), and diameters ($\sim$10 - 50 nm) of undoped, defective carbon nanotubes than in non-active carbon nanotubes ($\sim$10 - 15 μm in length and (ca. 20 nm in diameter) is visible in addition to more irregular, curved, and kinked features. The overall growth density across the sample is similarly uniform.

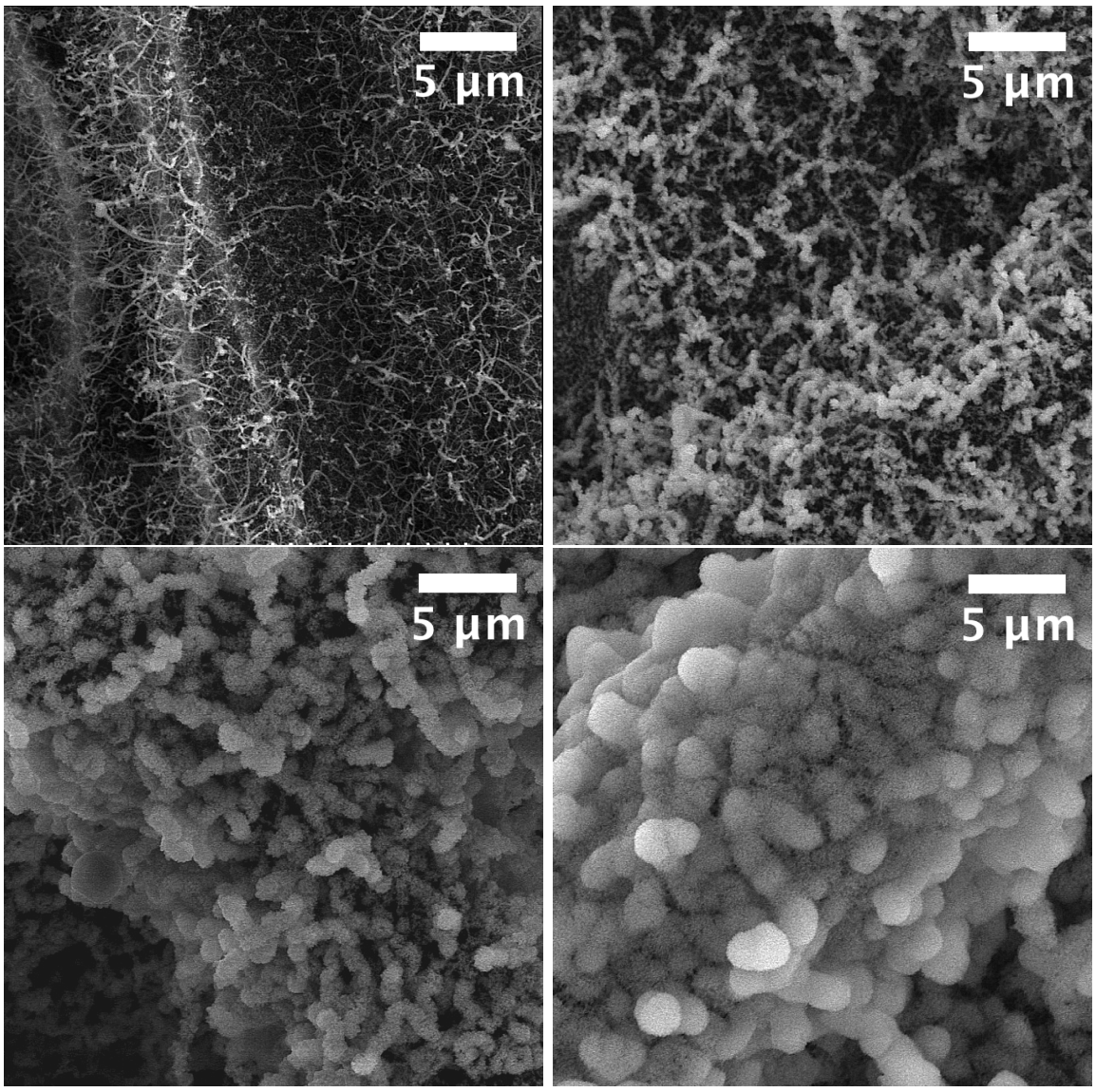

Figure 7.6: Representative low magnification SEM images of electrospray-deposited CsH_2PO_4 onto nitrogen doped CNTs at 15, 30, 45, and 60 min deposition time

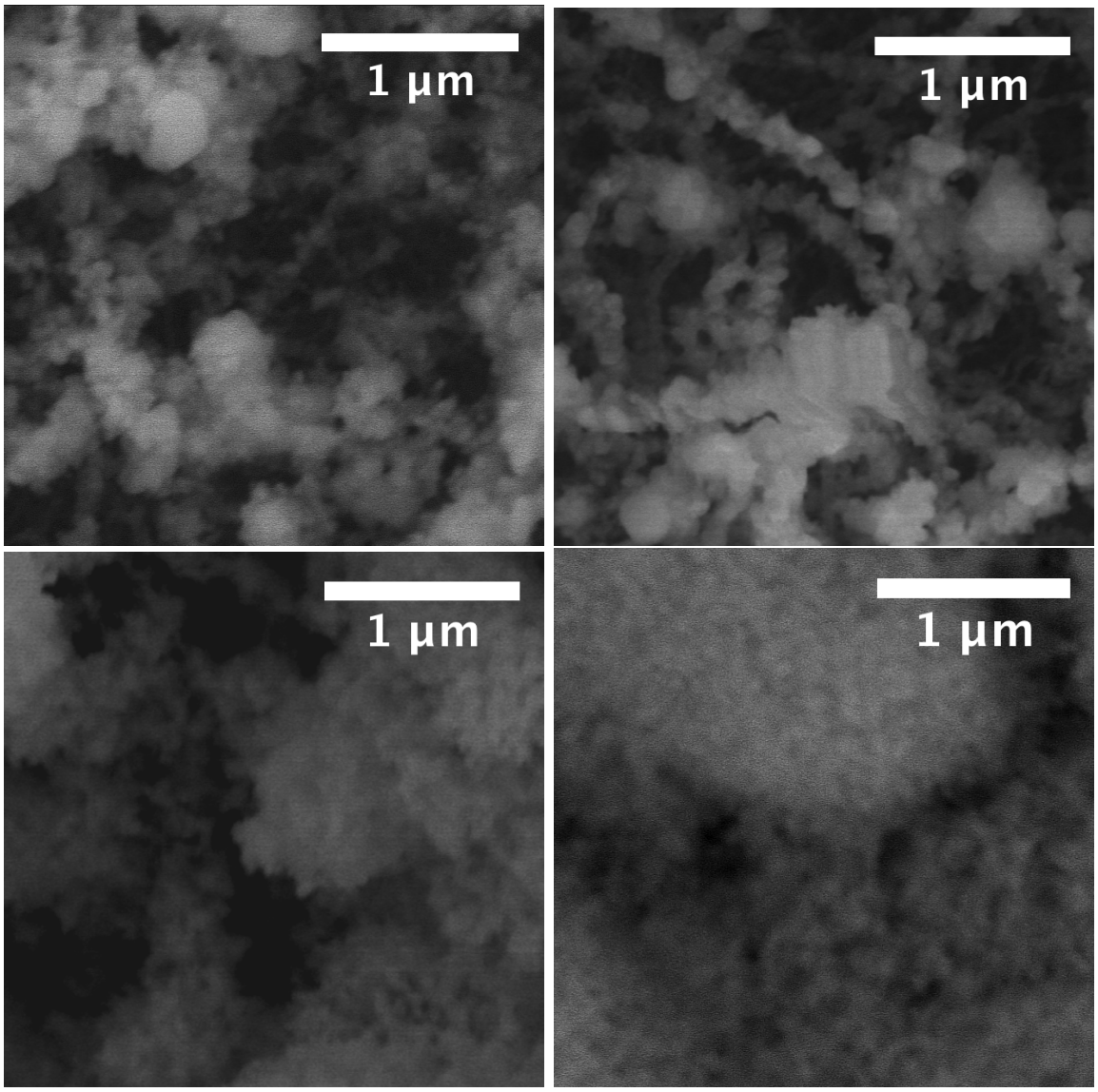

Figure 7.7: Representative high magnification SEM images of electrospray-deposited CsH_2PO_4 onto nitrogen doped CNTs at 15, 30, 45, and 60 min deposition time
.

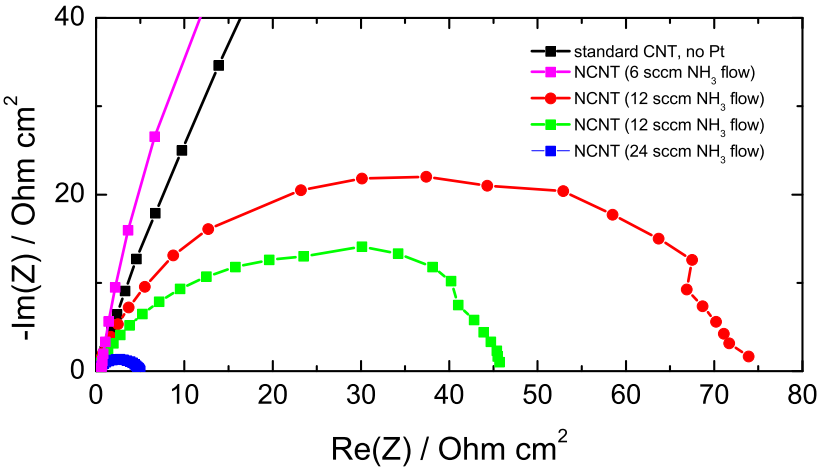

Figure 7.8: Impedance spectra of symmetric cells with NCNT containing electrodes measured at T = 240 °C, pH_2O = 0.4 atm, pO_2 = 0.6 atm - cells were fabricated with varying ammonia flow rates

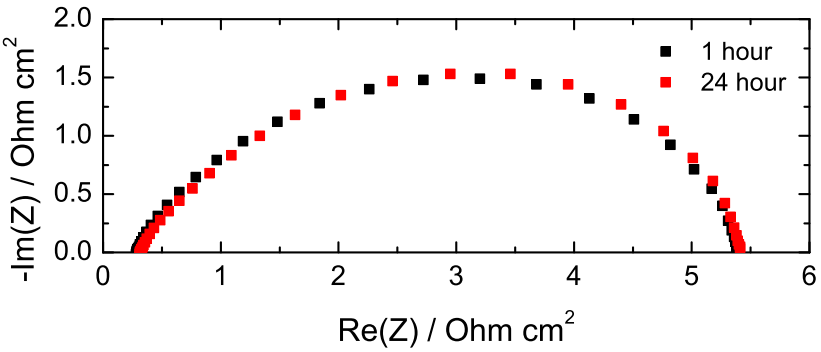

Figure 7.9: Impedance spectra of NCNT-containing electrodes showing 24 hour stability, measured at T = 240 °C, pH_2O = 0.4 atm, pO_2 = 0.6 atm

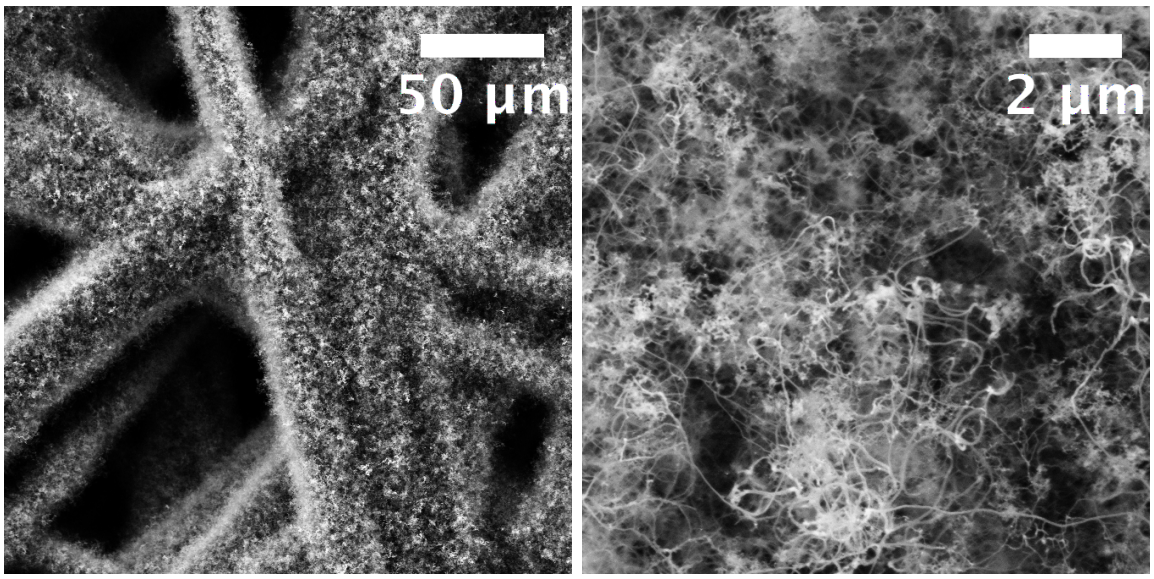

Figure 7.10: SEM images of undoped, defective carbon nanotubes on carbon paper at (a) low and (b) high magnification

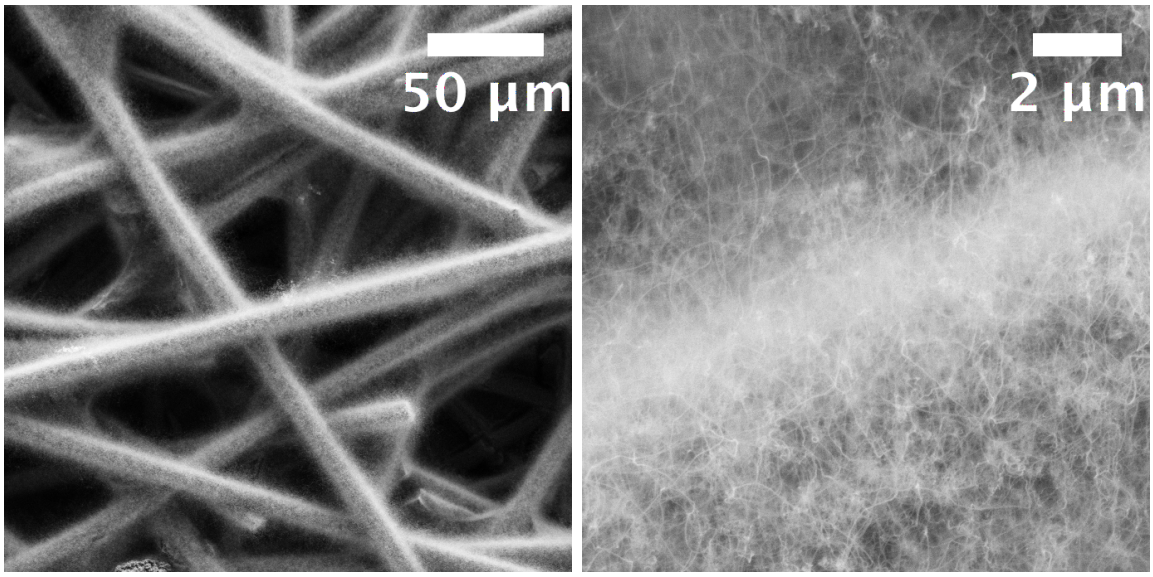

Figure 7.11: SEM images of standard, non-active carbon nanotubes on carbon paper (Chapter 6) at (a) low and (b) high magnification

Figure 7.12 shows two representative Raman spectra of standard, standard CNTs and undoped, defective CNTs. The D to G-band intensity ratios differ strongly between the two samples: We observed I(D)/I(G)<1 for the standard, inactive CNTs and I(D)/I(G)>1 for the undoped, defective CNTs. The results strongly suggest that the defect concentration of the catalytically active CNTs is significantly higher than in the standard CNTs.

7.3.0.3 A.C. impedance measurements with no D.C. bias

Figures 7.13 (a) and (b), 7.14 (a) and (b) show impedance spectra in the Nyquist representation (-Im(Z) vs. Re(Z)) of identically fabricated symmetric cells after a short 1 - 2 hour stabilization period. The electrolyte resistance, apparent as a shift of the electrode arc along the real axis is subtracted for convenience. Electrode area specific resistance values were ranging from 400 Ω cm^2 to 0.2 Ω cm^2. Although this is a wide variation, in no instance was the resistance as high as for conventional, undoped CNTs by itself. The impedance of non-active electrodes (not shown here, ref. Chapter 6) was >1 MΩ cm^2 with a high capacitive contribution at the low frequency

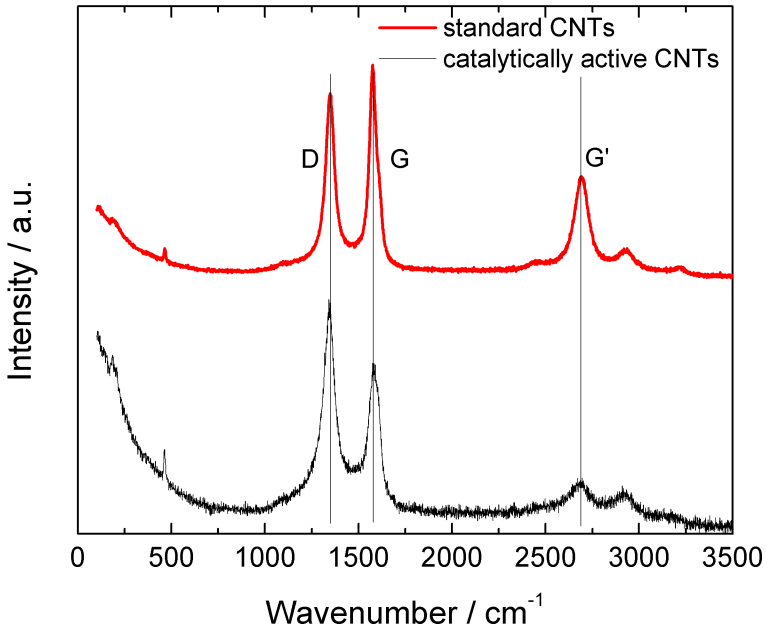

Figure 7.12: Raman spectra of undoped, defective CNTs and standard CNTs with the D, G, and G' bands indicated.

measurement range, indicating the existence of layers with charge accumulation (e.g. a blocking electrode). However the consistency of the results is poor, and can be attributed to two different sources:

1. Small variations in growth conditions during chemical vapor deposition, such as humidity, barometric pressure, and sample positioning, reactor wall conditions, as well as substrate properties, such as catalyst particle size distribution and spacing on the substrate, can lead to large differences in the physical properties of carbon nanotubes. [118] These properties include length and diameter of the nanotubes, the defect concentration, which may influence the catalytic properties. 2. The number density of the triple phase boundary interfaces between the carbon nanotubes and the CsH_2PO_4 electrolyte particles has a more direct impact on the area specific resistance. For high performance, low impedance electrodes, we seek to maximize the number density of such triple phase boundaries. A more monodisperse grainsize distribution of the fine-CsH_2PO_4 powder, and precise control during uniaxial cold-pressing is

expected to improve the level of consistency significantly.

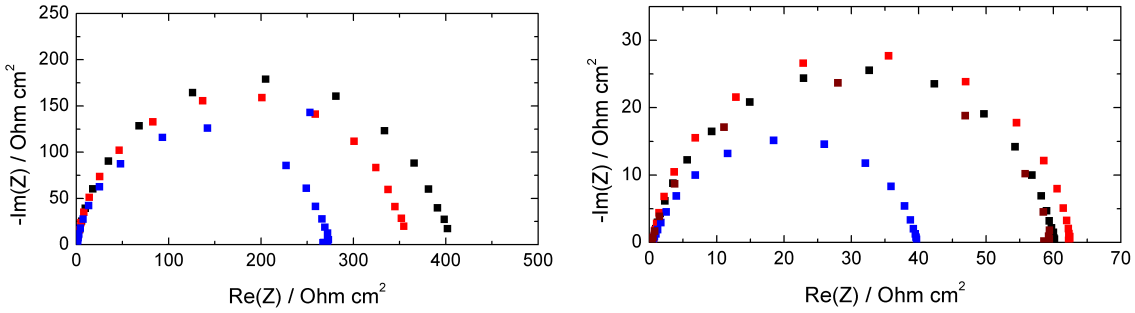

Figure 7.13: Nyquist plot of impedance spectra of symmetric cells containing undoped, defective CNTs only - high impedance, measured at T = 240 °C, pH_2O = 0.4 atm, pO_2 = 0.6 atm

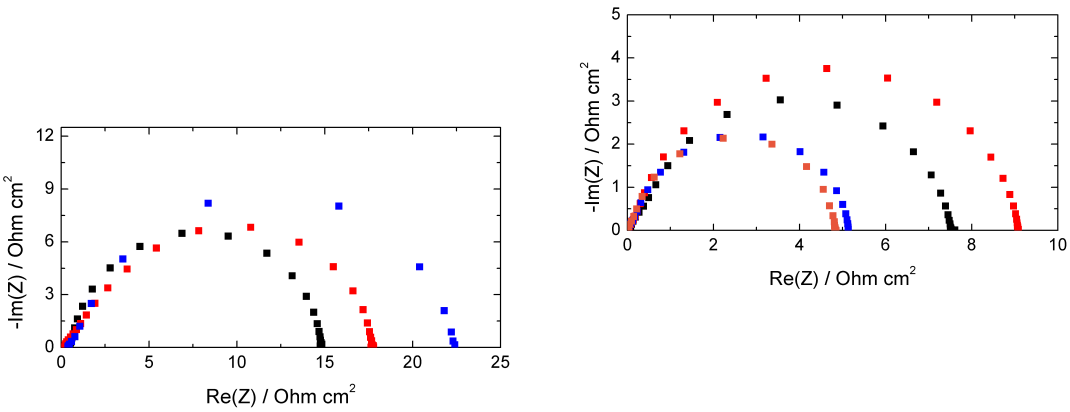

Figure 7.14: Nyquist plot of impedance spectra of symmetric cells containing undoped, defective CNTs only - intermediate impedance, measured at T = 240 °C, pH_2O = 0.4 atm, pO_2 = 0.6 atm

Remarkably small electrode impedance values (0.2 - 0.4 Ωcm^2) were measured for four separate symmetric cells in humidified oxygen suggesting highly efficient catalysis of both water splitting and oxygen reduction reaction, Figure 7.15.

After a 2 hour initial stabilization, the degradation rate over an 18 hour period of the electrode impedance of one representative sample was <1/hour, Figure 7.16. A slight increase of the electrode impedance at the second heating and measurement

cycle, after storing the sample for 3 days at ambient conditions was measured and can be attributed to morphological changes of the CsH_2PO_4 structure, leading to a possible decrease of the catalytically active triple phase boundaries. The electrode impedance values (width of the arc) was determined by fitting a parallel RC circuit and is plotted as a function of time, Figure 7.16 (b).

Carbon dioxide and carbon monoxide concentration vs. time, Figure 7.17 (a), shows excellent stability of free-standing carbon paper substrates overgrown with defective carbon nanotubes at solid acid fuel cell operating conditions. The gas concentrations measured at temperatures up to 250°C are the background gas concentrations with a slight instrument drift. The sharp step-wise increase in the CO and CO_2 gas concentrations at 300°C in the CNT containing sample and 450°C in the blank carbon paper sample indicate the onset of degradation through an oxidation process and the boundary of the stability window.

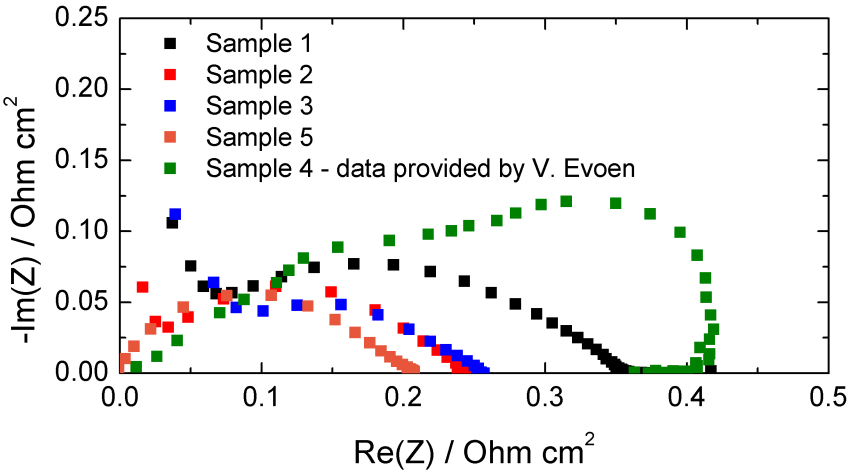

Figure 7.15: Nyquist plot of impedance spectra of symmetric cells containing undoped, defective CNTs only - low impedance, at T = 240 °C, pH_2O = 0.4 atm, pO_2 = 0.6 atm

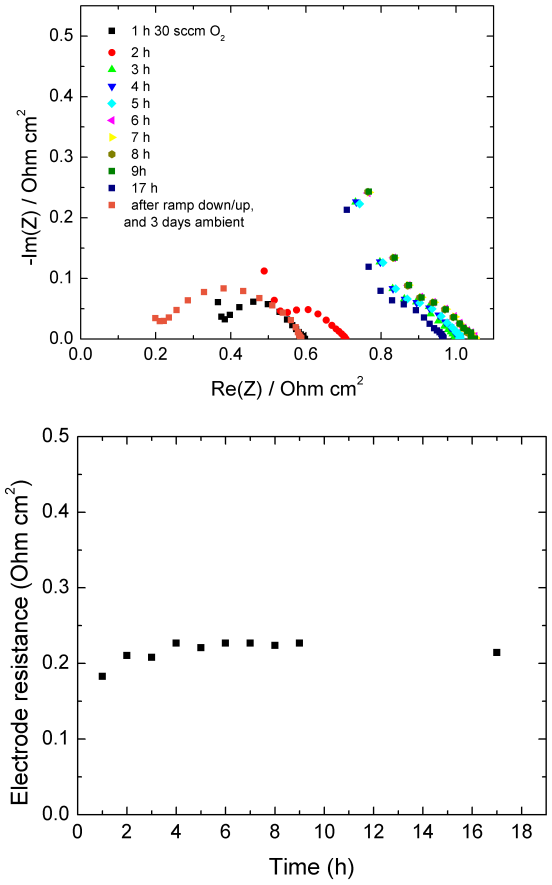

Figure 7.16: (a) Nyquist plot and (b) stability plot (electrode impedance vs. time) for a representative symmetric cell with undoped, defective CNTs measured at T = 240 °C, pH_2O = 0.4 atm, pO_2 = 0.6 atm

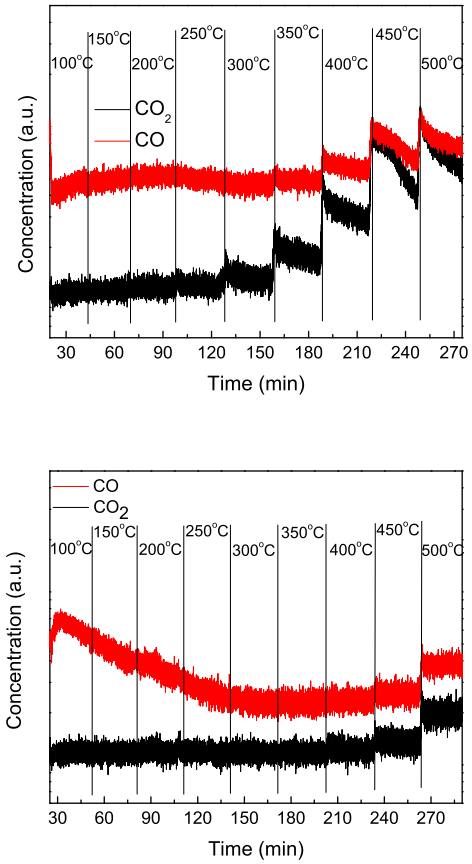

Figure 7.17: CO and CO_2 concentration vs. time obtained with a mass spectrometer at different temperatures of (a) undoped, defective CNTs and carbon paper and (b) carbon paper only, measured at pH_2O = 0.4 atm, pO_2 = 0.6 atm

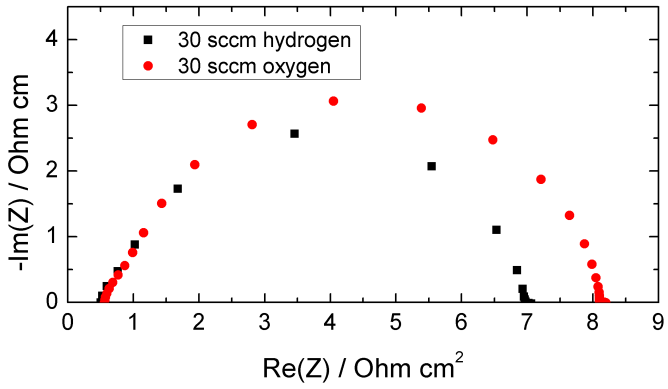

Figure 7.18: Impedance spectra for undoped, defective CNTs in symmetric humidified hydrogen and oxygen environment, measured at T = 240 °C, pH_2O = 0.4 atm, pO_2 = 0.6 atm

7.3.0.4 A.C. impedance measurements with D.C. bias

Figure 7.19 (a) shows the impedance spectra in the Nqyquist form (-Im(Z) vs. Re(Z)) for representative symmetric cell electrodes. The electrolyte contribution to the impedance was subtracted for convenience. The electrode D.C. resistance (low frequency intercept of the electrode arc) was replotted vs. D.C. bias. Typical Butler-Volmer eletrode behavior is observed, with the electrode resistance decreasing from 0.4 to 0.02 Ω cm^2, Figure 7.19 (b).

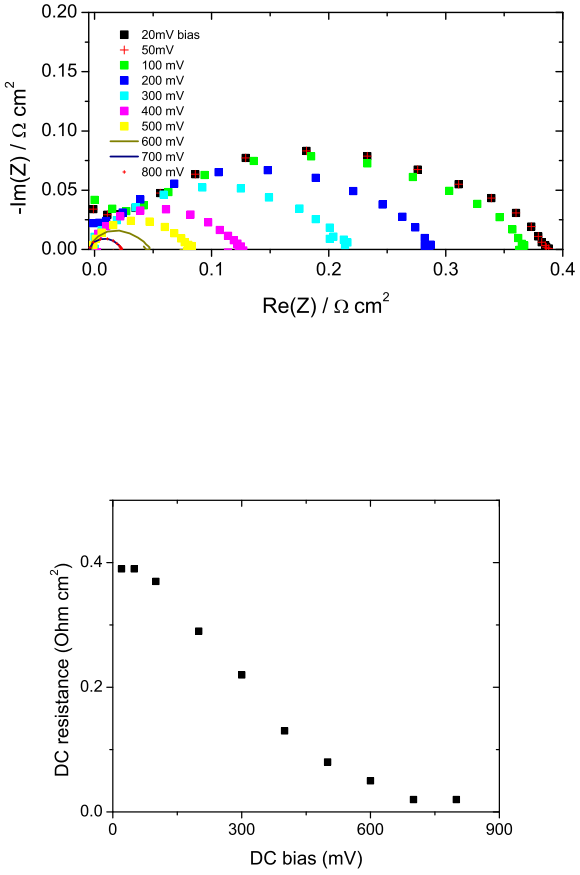

Figure 7.19: DC biased measurements of symmetric cell: (a) Nyquist plot of impedance spectra and (b) DC resistance vs. bias voltage at T = 240 °C, pH_2O = 0.4 atm, pO_2 = 0.6 atm

The corresponding current density values for each applied D.C. voltage values are shown in Figure 7.20. For such electrochemical devices extremely high current density

values of up to 3.5 A cm^{-2} were observed at 700 mV D.C. voltage bias.

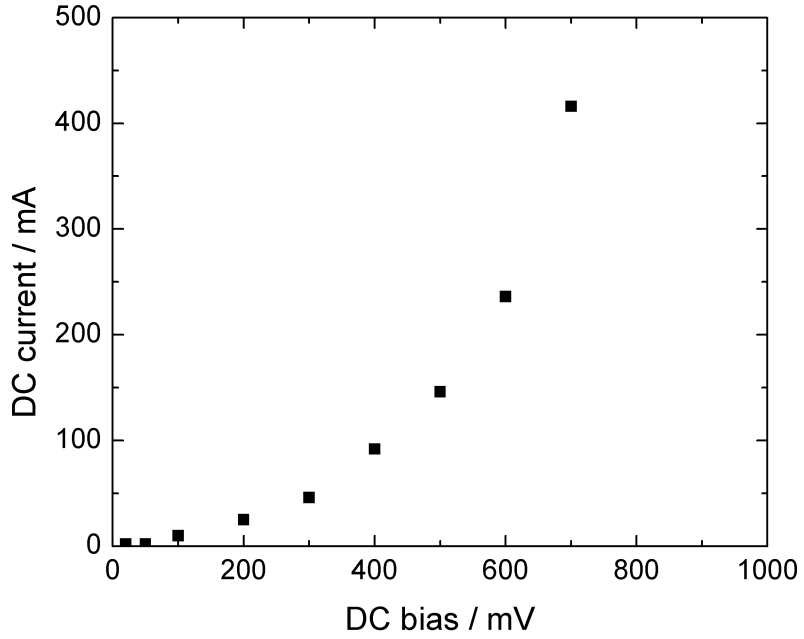

Figure 7.20: Current density vs. applied voltage for a symmetric cell with undoped, defective CNTs, measured at T = 240 °C, pH_2O = 0.4 atm, pO_2 = 0.6 atm

Figure 7.21 shows the cyclic voltammetry scan of a representative symmetric cell, containing cundoped, defective CNTs. The scan rate of 0.001 V/sec, resulting in a 17 hour total scan time. Slight degradation of the current density over a ∼4 hour period is apparent. The curve was fitted with a third degree polynomial ($f(x) = 0.075x + 0.001x^2 + 0.024x^3$) and the area integrated in order to calculate the total charge through the symmetric cell 464 C.

In order to determine whether carbon corrosion could be the explanation for the high current density through the symmetric cell under DC bias, the total amount of carbon necessary to provide 464 C through carbon corrosion is calculated, Equation 7.1

Cathode:

$$C + 2\ H_2O \rightarrow CO_2 + 4\ H^+ + 4\ e^- \tag{7.1}$$

is 14 mg. The total amount of carbon, including carbon paper and undoped, defec-

tive carbon nanotubes is 21 mg per electrode. Thus, most of the current through the cell has to be sourced from the electrocatalytic water splitting and oxygen reduction reactions.

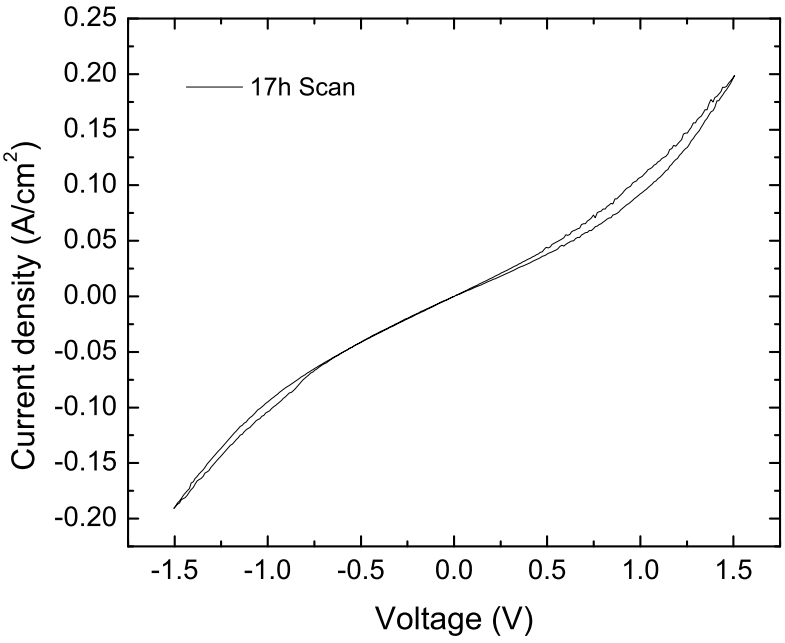

Figure 7.21: 17 h cyclic voltammetry scan of a representative symmetric cell with undoped, defective CNTs, measured at T = 240 °C, pH_2O = 0.4 atm, pO_2 = 0.6 atm. Includes ohmic contributions to voltage due to the electrolyte

7.4 Conclusion

We demonstrated remarkable catalytic activity of both nitrogen doped and undoped carbon nanotubes as electrocatalysts in solid acid fuel cell electrodes. AC impedance spetroscopy of symmetric cells in humidified oxygen showed a 5 Ωcm^2 area specific resistance for NCNT containing electrodes and as low as 0.2 Ωcm^2 for undoped CNT containing electrodes. Excellent stability over 18 h or longer periods has been shown in both types of nanotubes at solid acid fuel cell operating conditions. The possibility of replacing platinum by undoped, defective carbon nanotubes will advance the field of solid acid fuel cells significantly and bring it closer to commercial reality.

Small electrode impedance values measured in a humidified oxygen environment also indicate excellent water splitting catalysis. Such a catalyst opens up the possibility to operate a solid acid fuel cell in reverse, as an electrochemical water splitting device.

Bibliography

[1] Nathan S Lewis and Daniel G Nocera. Powering the planet: Chemical challenges in solar energy utilization. *PNAS*, 103(43):15729–15735, 2006.

[2] WIlliam Grove. On a gaseous voltaic battery. *Philosophical Magazine*, 21(140):417–420, 1842.

[3] James Larminie and Andrew Dicks. *Fuel Cell Systems Explained*. Wiley, New York, 2 edition, 2003.

[4] Tetsuya Uda and Sossina M. Haile. Thin-membrane solid-acid fuel cell. *Electrochemical and Solid-State Letters*, 8(5):A245, 2005.

[5] Tetsuya Uda, Dane A. Boysen, Calum R. I. Chisholm, and Sossina M. Haile. Alcohol fuel cells at optimal temperatures. *Electrochemical and Solid-State Letters*, 9(6):A261, 2006.

[6] Sossina M. Haile, Calum R. I. Chisholm, Kenji Sasaki, Dane A. Boysen, and Tetsuya Uda. Solid acid proton conductors: from laboratory curiosities to fuel cell electrolytes. *Faraday Discussions*, 134:17, 2007.

[7] Dane A Boysen, Tetsuya Uda, Carum RI Chisholm, and Sossina M. Haile. High performance solid acid fuel cells through humidity stabilization. *Science*, 303:68–70, 2004.

[8] C R I Chisholm, Dane A Boysen, Alexander B. Papandrew, Strahinja K. Zecevic, SukYal Cha, K. A. Sasaki, Ãron Varga, Konstantinos P. Giapis, and S. M. Haile. From laboratory curiosities to technological realization: The development path for solid acid fuel cells. *Interface Magazine*, 18:53–59, 2009.

[9] Yu-ki Taninouchi, Tetsuya Uda, Yasuhiro Awakura, Ayako Ikeda, and Sossina M. Haile. Dehydration behavior of the superprotonic conductor csh2po4 at moderate temperatures: 230 to 260 Â°c. *Journal of Materials Chemistry*, 17(30):3182, 2007.

[10] Ayako Ikeda and Sossina M. Haile. The thermodynamics and kinetics of the dehydration of csh2po4 studied in the presence of sio2. *Solid State Ionics*, 213:63–71, 2012.

[11] Ayako Ikeda and Sossina M. Haile. Examination of the superprotonic transition and dehydration behavior of cs0.75rb0.25h2po4 by thermogravimetric and differential thermal analyses. *Solid State Ionics*, 181(3-4):193–196, 2010.

[12] Chatr Panithipongwut and Sossina M. Haile. High-temperature phase behavior in the rb3h(so4)2ârbhso4 pseudo-binary system and the new compound rb5h3(so4)4. *Solid State Ionics*, 213:53–57, 2012.

[13] Mary W. Louie, Mikhail Kislitsyn, Kaushik Bhattacharya, and Sossina M. Haile. Phase transformation and hysteresis behavior in cs1âxrbxh2po4. *Solid State Ionics*, 181(3-4):173–179, 2010.

[14] Mary W. Louie and Sossina M. Haile. Platinum thin film anodes for solid acid fuel cells. *Energy Environmental Science*, 4(10):4230, 2011.

[15] Mary W. Louie, Kenji Sasaki, and Sossina M. Haile. Towards understanding electrocatalysis in cdp based fuel cells pt and pd thin film electrodes. *Electrochemical Society Transactions*, 13(28):57–62, 2008.

[16] Mary W. Louie, A Hightower, and S. M. Haile. Nanoscale electrodes by conducting atomic force microscopy: Oxygen reduction kinetics at the pt|cshso4 interface. *ACS Nano*, 4(5):2811–2821, 2010.

[17] K. A. Sasaki, Y. Hao, and S. M. Haile. Geometrically asymmetric electrodes for probing electrochemical reaction kinetics: a case study of hydrogen at the pt-csh2po4 interface. *Phys Chem Chem Phys*, 11(37):8349–57, 2009. Sasaki, Kenji A Hao, Yong Haile, Sossina M England Phys Chem Chem Phys. 2009 Oct 1;11(37):8349-57. Epub 2009 Jul 15.

[18] K. A. Sasaki. *Electrochemical Characterization of Solid Acid Fuel Cell Electrodes*. PhD thesis, 2010.

[19] John Zeleny. The electrical discharge from liquid points, and a hydrostatic method of measuring the electric intensity at their surfaces. *Physical Review*, 3(2):69–91, 1914.

[20] Geoffrey Taylor. Disintegration of water drops in an electric field. *Proceedings of the Royal Society of London, Seies A, Mathematical and Physical Sciences*, 280(1382):383–397, 1964.

[21] L Rayleigh. On the equilibrium of liquid conducting masses charged with electricity. *Philosophical Magazine*, 14:184–186, 1882.

[22] Malcolm Dole, LL Marck, RL Hines, RC Mobley, LD Ferguson, and MB Alice. Molecular beams of macroions. *The Journal of Chemical Physics*, 49(5):2240, 1968.

[23] B. A. Thomson and J. V. Iribarne. Field induced ion evaporation from liquid surfaces at atmospheric pressure. *The Journal of Chemical Physics*, 71(11):4451, 1979.

[24] Masamichi Yamashita and John B Fenn. Electrospray ion source - another variation on the free-jet theme. *Journal of Physical Chemistry*, 88:4451–4459, 1984.

[25] I. Taniguchi. Electrostatic spray deposition of gd0.1ce0.9o1.95 and la0.9sr0.1ga0.8mg0.2o2.87 thin films. *Solid State Ionics*, 160(3-4):271–279, 2003.

[26] T Nguyen and E. Djurado. Deposition and characterization of nanocrystalline tetragonal zirconia films using electrostatic spray deposition. *Solid State Ionics*, 138:191–197, 2001.

[27] A. Princivalle, D. Perednis, R. Neagu, and E. Djurado. Porosity control of lsm/ysz cathode coating deposited by electrospraying. *Chemistry of Materials*, 17(5):1220–1227, 2005.

[28] Chunhua Chen, Erik M Kelder, Paul JJM van der Put, and J. Schoonman. Morphology control of licoo2 films fabricated using the electrostatic spray technique. *Journal of Materials Chemistry*, 6(5):765–771, 1996.

[29] IW Lenggoro, K Okuyama, J Fernandez de la Mora, and Noboru Tohge. Preparation of zns nanoparticles via electrospray pyrolysis. *Journal of Aerosol Science*, 31(1):121–136, 2000.

[30] David Mesguich, Jean-Marc Bassat, Cyril Aymonier, and Elisabeth Djurado. Nanopowder synthesis of the sofc cathode material nd2nio4 by ultrasonic spray pyrolysis. *Solid State Ionics*, 181(21-22):1015–1023, 2010.

[31] Olga A. Baturina and Gary E. Wnek. Characterization of proton exchange membrane fuel cells with catalyst layers obtained by electrospraying. *Electrochemical and Solid-State Letters*, 8(6):A267, 2005.

[32] R. Benitez, J. Soler, and L. Daza. Novel method for preparation of pemfc electrodes by the electrospray technique. *Journal of Power Sources*, 151:108–113, 2005.

[33] Ãron Varga, Nicholas A. Brunelli, Mary W. Louie, Konstantinos P. Giapis, and Sossina M. Haile. Composite nanostructured solid-acid fuel-cell electrodes via electrospray deposition. *Journal of Materials Chemistry*, 20(30):6309, 2010.

[34] A Jaworek and A Krupota. Classification of the modes of ehd spraying. *Journal of Aerosol Science*, 30(7):873–893, 1999.

[35] A. Jaworek and A. T. Sobczyk. Electrospraying route to nanotechnology: An overview. *Journal of Electrostatics*, 66(3â4):197–219, 2008.

[36] Liang Kuang Lim, Jinsong Hua, Chi-Hwa Wang, and Kenneth A. Smith. Numerical simulation of cone-jet formation in electrohydrodynamic atomization. *AIChE Journal*, 57(1):57–78, 2011.

[37] RPA Hartman, DJ Brunner, DMA Camelot, JCM Marijnissen, and B Scarlett. Electrohydrodynamic atomization in the cone.

[38] Alfonso M. Ganan-Calvo. Cone-jet analytical extension of taylorâs electrostatic solution and the asymptotic universal scaling laws in electrospraying. *Physical Review Letters*, 79(2):217–220, 1997.

[39] I Hayati, Adrian G Bailey, and Th F Tadros. Mechanism of stable jet formation in electrohydrodynamic atomization. *Nature*, 319:41–43, 1986.

[40] R P A Hartman, D J Brunner, D M A Camelot, J C M Marijnissen, and B Scarlett. Jet break-up in electrohydrodynamic atomization in the cone-jet mode. *Journal of Aerosol Science*, 31(1):65–95, 2000.

[41] Da-Ren Chen and David Y. H. Pui. Experimental investigation of scaling laws for electrospraying: Dielectric constant effect. *Aerosol Science and Technology*, 27(3):367–380, 1997.

[42] AM Ganan-Calvo, J Davila, and A Barrero. Current and doplet size in the electrospraying of liquids scaling laws. *Journal of Aerosol Science*, 28(2):249–275, 1997.

[43] Hong Kyoon Choi, Jang-Ung Park, O. Ok Park, Placid M. Ferreira, John G. Georgiadis, and John A. Rogers. Scaling laws for jet pulsations associated with high-resolution electrohydrodynamic printing. *Applied Physics Letters*, 92(12):123109, 2008.

[44] C. H. Chen, D. A. Saville, and I. A. Aksay. Scaling laws for pulsed electrohydrodynamic drop formation. *Applied Physics Letters*, 89(12):124103, 2006.

[45] Alfonso M. Ganan-Calvo. On the general scaling theory for electrospraying. *Journal of Fluid Mechanics*, 507:203–212, 2004.

[46] Wenhua Gu, Philip Edward Heil, Hyungsoo Choi, and Kyekyoon Kim. Comprehensive model for fine coulomb fission of liquid droplets charged to rayleigh limit. *Applied Physics Letters*, 91(6):064104, 2007.

[47] Alessandro Gomez and Keqi Tang. Charge and fission of droplets in electrostatic sprays. *Physics of Fluids*, 6(1):404, 1994.

[48] Christopher J Hogan, Pratim Biswas, and D. R. Chen. Charged droplet dynamics in the submicrometer size range. *Journal of Physical Chemistry B*, 113:970–976, 2009.

[49] Ronald L Grimm and JI Beauchamp. Evaporation and discharge dynamics of highly charged droplets of heptane, octane, and p-xylene generated by electrospray ionization. *Analytical Chemistry*, 74:6291–6297, 2002.

[50] Ronald L Grimm and JI Beauchamp. Evaporation and discharge dynamics of highly charged multicomponent droplets generated by electrospray ionization. *Journal of Physical Chemistry A*, 114:1411–1419, 2010.

[51] O. Wilhelm, L. MÃdler, and S. E. Pratsinis. Electrospray evaporation and deposition. *Journal of Aerosol Science*, 34(7):815–836, 2003.

[52] J N Smith, RC Flagan, and JI Beauchamp. Droplet evaporation and discharge dynamics in electrospray ionization. *Journal of Physical Chemistry A*, 106:9957–9967, 2002.

[53] L. Konermann. A simple model for the disintegration of highly charged solvent droplets during electrospray ionization. *J Am Soc Mass Spectrom*, 20(3):496–506, 2009. Konermann, Lars J Am Soc Mass Spectrom. 2009 Mar;20(3):496-506. Epub 2008 Nov 21.

[54] P Kebarle. A brief overview of the present status of the mechanisms involved in electrosrapy mass spectrometry. *Journal of Mass Spectrometry*, 35:804–817, 2000.

[55] D. H. Charlesworth and W. R. Marshall Jr. Evaporation from drops containing dissoved solids. *AIChE Journal*, 6(1):9–23, 1957.

[56] O. Wilhelm, S. E. Pratsinis, D. Perednis, and L. J. Gauckler. Electrospray and pressurized spray deposition of yttria-stabilized zirconia films. *Thin Solid Films*, 479(1-2):121–129, 2005.

[57] IW Lenggoro, B Xia, and K Okuyama. Sizing of colloidal nanoparticles by electrospray and differential mobility analyzer methods. *Langmuir*, 18:4584–4591, 2002.

[58] B Han, I W Lenggoro, M Choi, and K Okuyama. ï¿Œï¿Œï¿Œmeasurement of cluster ions and residue nanoparticles from water samples with an electrospray differential mobility analyzer. *Analytical Sciences*, 19:843–851, 2003.

[59] Atsumu Hirabayashi. Evaporation of charged fine droplets. *International Journal of Mass Spectrometry and Ion Processes*, 175:241–245, 1998.

[60] M Lohmann, H Beyer, and A Schmidt-Ott. Size and charge distribution of liquid metal electrospray generated nanoparticles. *Journal of Aerosol Science*, 28(1):s349–S350, 1997.

[61] M Gamero-Castano and J Fernandez de la Mora. Mechanisms of electrospray ionization of singly and multiply charged salt clusters. *Analytica Chimica Acta*, 406:67–91, 2000.

[62] IW Lenggoro, B Xia, and K Okuyama. Sizing of colloidal nanoparticles by electrospray and differential mobility analyzer methods. *Langmuir*, 18:4584–4591, 2002.

[63] Basics of electrochemical impedance spectroscopy.

[64] RM Sankaran, D Holunga, RC Flagan, and Konstantinos P. Giapis. Synthesis of blue luminescent si nanoparticles using atmospheric-pressure microdischarges. *Nanoletters*, 5(3):537–541, 2005.

[65] M. L. Ostraat, J. W. De Blauwe, M. L. Green, L. D. Bell, M. L. Brongersma, J. Casperson, R. C. Flagan, and H. A. Atwater. Synthesis and characterization of aerosol silicon nanocrystal nonvolatile floating-gate memory devices. *Applied Physics Letters*, 79(3):433, 2001.

[66] Da-Ren Chen, DYH Pui, and SL Kaufman. ï¿Œelectrospraying of conducting liquids for monodisperse aerosol generation in the 4 nm to 1.8 pm diameter range. *Journal of Aerosol Science*, 26(6):963–977, 1995.

[67] Michel Cloupeau and Bernard Prunet-Foch. Electrohydrodynamic spraying functioning modes: A critical review. *Journal of Aerosol Science*, 25(6):1021–1036, 1994.

[68] J Fernandez de la Mora and I G Loscertales. The current emitted by higly conducting taylor cones. *Journal of Fluid Mechanics*, 260:155–184, 1994.

[69] G. V. Jayanthi, S. C. Zhang, and Gary L. Messing. Modeling of solid particle formation during solution aerosol thermolysis: The evaporation stage. *Aerosol Science and Technology*, 19(4):478–490, 1993.

[70] Keqi Tang and Richard D Smith. Theoretical prediction of charged droplet evaporation and fission in electrospray ionization. *International Journal of Mass Spectrometry*, 185:97–105, 1999.

[71] Aaron J. Rulison and Richard C. Flagan. Scale-up of electrospray atomization using linear arrays of taylor cones. *Review of Scientific Instruments*, 64(3):683, 1993.

[72] John H Seinfeld and Spyros N Pandis. *Atmospheric Chemistry and Physics*. John Wiley and Sons, New York, 1998.

[73] Rebecca J Hopkins and Jonathan P Reid. A comparative study of the mass and heat transfer dynamics of evaporating ethanol/ water, methanol/water, and 1-propanol/water aerosol droplets. *Journal of Physical Chemistry*, 110:3239–3249, 2006.

[74] R. J. Hopkins, C. R. Howle, and J. P. Reid. Measuring temperature gradients in evaporating multicomponent alcohol/water droplets. *Phys Chem Chem Phys*, 8(24):2879–88, 2006. Hopkins, Rebecca J Howle, Chris R Reid, Jonathan P England Phys Chem Chem Phys. 2006 Jun 28;8(24):2879-88. Epub 2006 May 24.

[75] Chul Ho Park and Jonghwi Lee. Electrosprayed polymer particles: Effect of the solvent properties. *Journal of Applied Polymer Science*, 114(1):430–437, 2009.

[76] C Pantano, AM Ganan-Calvo, and A Barrero. Zeroth-order electrohydrostatic solution for electrospraying in cone-jet mode. *Journal of Aerosol Science*, 25(6):1065–1077, 1994.

[77] Richard C. Flagan. On differential mobility analyzer resolution. *Aerosol Science and Technology*, 30(6):556–570, 1999.

[78] William A. Hoppel and Glendon M. Frick. Ion - aerosol attachment coefficients and the steady-state charge distribution on aerosols in a bipolar ion environment. *Aerosol Science and Technology*, 5(1):1–21, 1986.

[79] Mark R. Stolzenburg and Peter H. McMurry. Equations governing single and tandem dma configurations and a new lognormal approximation to the transfer function. *Aerosol Science and Technology*, 42(6):421–432, 2008.

[80] Hyun-Ha Kim, Jong-Ho Kim, and Atsushi Ogata. Time-resolved high-speed camera observation of electrospray. *Journal of Aerosol Science*, 42(4):249–263, 2011.

[81] BY Liu and KW Lee. *American Industrial Hygene Association*, 36:861–865, 1975.

[82] Zohra Olumee, John H Callahan, and Akos Vertes. Droplet dynamics changes in electrostatic sprays of methanol-water mixtures. *Journal of Physical Chemistry*, 102:9154–9160, 1998.

[83] Khellil Sefiane, Samuel David, and Martin ER Shanahan. Wetting and evaporation of binary mixture drops. *Journal of Physical Chemistry*, 112:11317–11323, 2008.

[84] M S Wilm and M Mann. Electrospray and taylor-cone theory, dole's beam of macromolecules at last? *International Journal of Mass Spectrometry and Ion Processes*, 136:167–180, 1994.

[85] Svein Sunde. Simulations of composite electrodes in fuel cells. *Journal of Electroceramics*, 5(2):153–182, 2000.

[86] Adrian G Bailey. *Electrostatic Spraying of Liquids*. Research Studies Press, Taunton, 1 edition, 1988.

[87] D. Perednis and L. J. Gauckler. Thin film deposition using spray pyrolisis. *Journal of Electroceramics*, 14:103–111, 2005.

[88] I. Taniguchi, RC Landschoot, and J. Schoonman. Fabrication of lscfo thin films by electrostatic spray deposition. *Solid State Ionics*, 156:1–13, 2003.

[89] C. W. Chen, D. Tano, and M. Akashi. Colloidal platinum nanoparticles stabilized by vinyl polymers with amide side chains: Dispersion stability and catalytic activity in aqueous electrolyte solutions. *J Colloid Interface Sci*, 225(2):349–358, 2000. Chen, Chun-Wei Tano, Daisuke Akashi, Mitsuru J Colloid Interface Sci. 2000 May 15;225(2):349-358.

[90] Yoshie Narui, Donato M Ceres, Jinyu Chen, Konstantinos P. Giapis, and CP Collier. High aspect ratio silicon dioxide-coated single-walled carbon nanotube scanning probe nanoelectrodes. *Journal of Physical Chemistry C*, 113:6815–6820, 2009.

[91] Daniel Marinha, CÃ©cile Rossignol, and Elisabeth Djurado. Influence of electrospraying parameters on the microstructure of la0.6sr0.4co0.2f0.8o3-d films for sofcs. *Journal of Solid State Chemistry*, 182(7):1742–1748, 2009.

[92] Y Borodko, SE Habas, M Koebel, Peidong Yang, H Frei, and Gabor A Somojai. Probing the interaction of poly(vinylpyrrolidone) with platinum nanocrystals by uv-raman and ftir. *Journal of Physical Chemistry B*, 110:23052–23059, 2006.

[93] Rointan F Bunshah. Deposition technologies for films and coatings– an overview.

[94] Alexander B. Papandrew, Calum R. I. Chisholm, Ramez A. Elgammal, Mustafa M. OÌzer, and Strahinja K. Zecevic. Advanced electrodes for solid acid fuel cells by platinum deposition on csh2po4. *Chemistry of Materials*, 23(7):1659–1667, 2011.

[95] N. Rajalakshmi, H. Ryu, M. Shaijumon, and S. Ramaprabhu. Performance of polymer electrolyte membrane fuel cells with carbon nanotubes as oxygen reduction catalyst support material. *Journal of Power Sources*, 140(2):250–257, 2005.

[96] H. Tang, J. H. Chen, Z. P. Huang, D. Z. Wang, Z. F. Ren, L. H. Nie, Y. F. Kuang, and S. Z. Yao. High dispersion and electrocatalytic properties of platinum on well-aligned carbon nanotube arrays. *Carbon*, 42(1):191–197, 2004.

[97] Yongyan Mu, Hanpu Luiung, Jinsong Hu, Li Jiang, and Lijun Wun. Controllable pt nanoparticle deposition on carbon nanotubes as anode catalyst for direct methanol fuel cells. *Journal of Physical Chemistry B*, 109:22212–22216, 2005.

[98] Xin Wang, Mahesh Waje, and Yushan Yan. Cnt-based electrodes with high efficiency for pemfcs. *Electrochemical and Solid-State Letters*, 8(1):A42, 2005.

[99] Minjae Jung, Kwang Yong Eun, Jae-Kap Lee, Young-Joon Baik, Kwang-Ryeol Lee, and Jong WAn Park. Growth of carbon nanotubes by chemical vapor deposition. *Diamond and Related Materials*, 10:1235–1240, 2001.

[100] Onder Metin, Vismadeb Mazumderm, Saim Ozkar, and Shouheng Sun. Monodisperse nickel nanoparticles and their catalysis in hydrolytic dehydrogenation of ammonia borane. *Journal of the American Chemical Society*, 132:1468–1469, 2010.

[101] WM Haynes. *CRC Handbook of Chemistry and Physics*, volume 94 of *CRC Press*. CRC Press, 2013.

[102] www.sigmaaldrich.com.

[103] Mukul Kumar and Yoshinori Ando. Chemical vapor deposition of carbon nanotubes: A review on growth mechanism and mass production. *Journal of Nanoscience and Nanotechnology*, 10(6):3739–3758, 2010.

[104] Marcel Schreier. *Performance Enhancement of Nanostructured Solid Acid Electrodes Through Carbon Nanotubes Based Current Collectors*. PhD thesis, 2012.

[105] G. D. Nessim. Properties, synthesis, and growth mechanisms of carbon nanotubes with special focus on thermal chemical vapor deposition. *Nanoscale*, 2(8):1306–23, 2010. Nessim, Gilbert D England Nanoscale. 2010 Aug;2(8):1306-23. doi: 10.1039/b9nr00427k. Epub 2010 May 28.

[106] M. S. Dresselhaus, G. Dresselhaus, R. Saito, and A. Jorio. Raman spectroscopy of carbon nanotubes. *Physics Reports*, 409(2):47–99, 2005.

[107] A. Jorio, Esko Kaupinnen, and Abdou Hassanien. *Carbon-Nanotube Metrology*. Springer Verlag, Berlin, 2008.

[108] S. M. Haile, Dane A Boysen, Calum Chisholm, and Ryan Merle. solid acids as fuel cell electrolytes. *Nature*, 410:910–913, 2001.

[109] Nenad M. Markovic, T. J. Schmidt, Vojislav R. Stamenkovic, and P N Ross. Oxygen reduction reaction on pt and pt bimetallic surfaces: A selective review. *Fuel Cells*, 1(2):105–116, 2001.

[110] M. K. Debe. Electrocatalyst approaches and challenges for automotive fuel cells. *Nature*, 486(7401):43–51, 2012. Debe, Mark K England Nature. 2012 Jun 6;486(7401):43-51. doi: 10.1038/nature11115.

[111] Stephen Maldonado and Keith J Stevenson. Influence of nitrogen doping on oxygen reduction electrocatalysis at carbon nanofiber electrodes. *Journal of Physical Chemistry B*, 109:4707–4716, 2004.

[112] R Czerw, M Terrones, J C Charlier, I X Blase, B Foley, K Kamalakaran, N Grobert, D Terrones, H Tekleab, P M Ajayan, W Blau, M Ruhle, and D L Carroll. Identification of electron donor states in n-doped carbon nanotub. *Nanoletters*, 1(9):457–460, 2001.

[113] R Droppa, P Hammer, ACM Carvalho, MC dos Santos, and F Alvarez. Incorporation of nitrogen in carbon nanotubes. *Journal of Non-Crystalline Solids*, 299(302):874–879, 2002.

[114] Kuanping Gong, Feng Du, Zhenhai Xia, Michael Durstock, and Liming Dai. Nitrogen-doped carbon nanotube arrays with high electrocatalytic activity for oxygen reduction. *Science*, 323:760–764, 2009.

[115] P. Ayala, R. Arenal, M. Rummeli, A. Rubio, and T. Pichler. The doping of carbon nanotubes with nitrogen and their potential applications. *Carbon*, 48(3):575–586, 2010.

[116] Liangti Qu, Yong Liu, Jon-Beom Baek, and Liming Dai. Nitrogen-doped graphene as efficient metal-free electrocatalyst for oxygen reduction in fuel cells. *ACS Nano*, 4(3):1321–1326, 2010.

[117] Qiang Zhang, Jia-Qi Huang, Meng-Qiang Zhao, Wei-Zhong Quian, and Fei Wei. Carbon nanotube mass production: Principles and processes. *ChemSUSChem*, 4:864–89, 2011.

[118] C. Ryan Oliver, Erik S. Polsen, Eric R. Meshot, Sameh Tawfick, Sei Jin Park, Mostafa Bedewy, and A. John Hart. Statistical analysis of variation in laboratory growth of carbon nanotube forests and recommendations for improved consistency. *ACS Nano*, 2013.